University of Ljubljana
Faculty of Computer and Information Science

Jernej Zupanc

Automated Assessment of Nanoparticle Influence on Giant Lipid Vesicles from Video Microscopy for Bio-Nano Interaction Studies

Doctoral Dissertation

Ljubljana, 2011

University of Ljubljana
Faculty of Computer and Information Science

Jernej Zupanc

Automated Assessment of Nanoparticle Influence on Giant Lipid Vesicles from Video Microscopy for Bio-Nano Interaction Studies

Doctoral Dissertation

Prof. Dr. Branko Šter
advisor

Prof. Dr. Damjana Drobne
coadvisor

Ljubljana, 2011

Univerza v Ljubljani
Fakulteta za računalništvo in informatiko

Jernej Zupanc

Avtomatizirano ugotavljanje vpliva nanodelcev na orjaške lipidne vezikle iz mikroskopskih posnetkov za študij bio-nano interakcij

DOKTORSKA DISERTACIJA

Prof. Dr. Branko Šter
MENTOR

Prof. Dr. Damjana Drobne
SOMENTORICA

Ljubljana, 2011

I Z J A V A O A V T O R S T V U

doktorske disertacije

Spodaj podpisani/-a _____,

z vpisno številko _____,

sem avtor/-ica doktorske disertacije z naslovom

_____

_____

S svojim podpisom zagotavljam, da:

- sem doktorsko disertacijo izdelal/-a samostojno pod vodstvom mentorja (naziv, ime in priimek)

  _____

  in somentorstvom (naziv, ime in priimek)

  _____

- so elektronska oblika doktorske disertacije, naslov (slov., angl.), povzetek (slov., angl.) ter ključne besede (slov., angl.) identični s tiskano obliko doktorske disertacije

- in soglašam z javno objavo elektronske oblike doktorske disertacije v zbirki »Dela FRI«.

V Ljubljani, dne _____ Podpis avtorja/-ice: _____

ABSTRACT

Nanoparticles have different chemical, physical, and biological characteristics than bulk materials of the same chemical composition. This offers infinite possibilities in their application, but at the same time provokes questions about their hazardous potential when in contact with biological systems. Much evidence suggests that nanoparticles affect cell membrane stability and subsequently exert toxic effects. To determine these interactions research is often conducted on lipid vesicles. Their resemblance to biological cell membranes allows studying nanoparticle interactions by exposing the vesicles instead of live organisms. In this dissertation, we present a methodology which enables observing thousands of lipid vesicles and analyzing their shape transformations. The idea is to capture microscopy video sequences containing lipid vesicle populations before and after exposure to nanoparticles. With the use of algorithms and approaches presented here, these video sequences can be stitched into mosaics, and thousands of vesicles in them automatedly segmented. This way we enable evaluation of the differences between exposed and unexposed vesicle populations.

The first step in the mosaic stitching process is filtering frames for static noise, which is inherent to the imaging system. Next, the frames of the video sequence are aligned using translation acquired with direct registration between subsequent frames. A mosaic is blended by applying temporal median filter to the aligned frames. The resulting mosaic, where each pixel is a median of all pixels representing it in the recorded frames, is then further improved. Using edge estimator and selected morphological operators, a foreground detection is performed. Every segmented vesicle is then locally registered in all frames containing it, since individual vesicles in the population express local movements. The frame with the sharpest vesicle representation is selected by area sharpness estimator and the selected area around the sharpest vesicle is then aligned and blended onto the median mosaic using gradient fusion. This way, the final mosaic consists of the sharpest

representation of every vesicle that was available in the video sequence. The vesicles in the improved mosaic can be manually or automatedly segmented. Since the manual segmentation is very time demanding, automated Markov random field model image segmentation is proposed. The final step is counting segmented vesicles, determining their diameters, and comparing the resulting data gathered from multiple populations to determine the effect of added investigated nanoparticles. The proposed methodology is tested on two experiments, where vesicles are exposed to two different nanoparticles. First, both nano-C_{60} and the detergent $ZnCl_2$ are found to provoke bursting of vesicles, which decreases the population size up to 80%. In the second experiment, $CoFe_2O_4$ nanoparticles cause an increase in mean vesicle diameter in comparison to the unexposed vesicle population, where the mean diameter decreases. Even though the results cannot directly point to the physics underlying the interaction, they provide suggestions on the direction for subsequent research.

Experimental results confirm our hypothesis, that insight on interactions between nanoparticles and lipid membranes can be gained by exposing populations of lipid vesicles to nanoparticles and gathering statistical data on vesicle shape transformations. Also, the computerized steps for stitching a video sequence into a mosaic and segmenting vesicle populations are to our best knowledge the first known solution to vesicle population analysis. Automated segmentation decreased the time required for manual vesicle segmentation eightfold, allowing conducting many more experiments with less manual labor. To conclude, the presented methodology is an important step not only in bio-nano studies, but also in general studies on lipid vesicles.

Keywords: image segmentation, lipid vesicles, video microscopy, mosaic, nanoparticles, nanotoxicity, large scale microscopy, virtual microscopy

POVZETEK

V zadnjem času vse več študij prihaja do ugotovitev, da interakcije z nanodelci vplivajo na stabilnost celičnih membran. Namesto izpostavljanja živih organizmov se za preučevanje interakcij z nanodelci pogosto uporabljajo lipidni vezikli kot model celičnih membran. Računalniško podprta metodologija, ki jo predstavljamo v disertaciji, omogoča zaznavanje in kvantificiranje morfoloških sprememb tisočev veziklov skozi čas izpostavljenosti nanodelcem. Metodologija zajema vse korake od eksperimentalnega protokola, računalniške obdelave mikrografij in analize pridobljenih podatkov. Namen našega dela je bil ugotoviti morebiten vpliv dveh tipov nanodelcev (C_{60} in $CoFe_2O_4$) na POPC lipidne vezikle s študijo populacije veziklov namesto izoliranih posameznikov. V predstavljenih eksperimentih ugotavljamo da oba preizkušena tipa nanodelcev vplivata na morfološke spremembe ali pokanje lipidnih veziklov.

Ključne besede: segmentacija slik, lipidni vezikli, video mikroskopija, mozaik, nanodelci, nanotoksikologija, mikroskopija večjih površin, virtualna mikroskopija

ACKNOWLEDGEMENTS

At the time of finishing this dissertation, the official world record to complete a full marathon is 2:03:59. Along the 42.2 km of streets of Berlin, Haile Gebrselassie on average required less than 17 seconds for every 100 m which, for most of us, qualifies as sprinting. Interestingly, "sprinting" is also a verb that perfectly illustrates what and how I felt during the last 20 months of my research. By far exceeding limits of what I believe is rational, balanced, and healthy behavior, I more or less consider that time devoured by and dedicated to the research somewhat summarized in this dissertation. I hereby dedicate this work to the people who patiently stood by the side of the road and cheered for my marathon. Some helped in paying for the trip, others ran a part of the run with me or even carried me for some distance. Some handed me water, gave precious feedback, others even paved the way, and some provided me with freedom, so I was able to run faster. I am dearly grateful to you all, not only for the role you played in this research, but also my life.

My parents Majda and Franc, Prof. Damjana Drobne, Asoc. Prof. Branko Šter, Prof. Andrej Dobnikar, Assist. Prof. Deniz Erdogmus, Silvana Kavčič, Mira Škrlj, Prof. Aleš Leonardis, Assist. Prof. Iztok Lebar Bajec, Prof. Miran Mihelčič, Asoc. Prof. Janez Demšar, and the coworkers at the Faculty of Computer and Information Science, Bionanoteam, Northeastern University, Max Planck Institute, and institutions like ARRS, U.S. Department of State, Fulbright Program, Ad-Futura, and Slovenian taxpayers.

Thank you.

— Jernej Zupanc, Ljubljana, May 2011.

CONTENTS

LIST OF FIGURES

LIST OF TABLES

1 Introduction

1.1 Dissertation outline

This dissertation presents a methodology for *in vitro* bio–nano interaction studies. It consists of an experiment with nanoparticles and giant unilamellar lipid vesicles (vesicles) to gather the data and computerized steps for the data analysis. Although the motivation and background of associated research in nanotoxicology and vesicle studies are presented, the core of the dissertation are the lipid vesicle population experiment protocol, image processing approaches to enable mosaic stitching, vesicle segmentation, and analysis of data describing the observed vesicle populations.

The proposed methodology consists of roughly five steps presented in Fig. 1.1. First, the lipid vesicle experiment which is adapted from previous research with some modifications to the micrograph recording protocol, where series of micrographs or video sequences are recorded of a population instead of isolated vesicles. Next, we propose image processing steps for stitching the microscopy video sequences of lipid vesicles into mosaics, each representing the whole recorded area. To replace the cumbersome manual vesicle segmentation an adaptation of the Markov random field image segmentation

model is proposed for automatic labeling of vesicles in the mosaics. The vesicle labels are then extracted and a statistical analysis of the vesicles' shapes in the observed lipid vesicle populations is performed. The data on the properties of segmented vesicles is then analyzed to extract underlying knowledge about the vesicle population. Three experiments are presented in the results section. First, the automatic segmentation is tested on synthesized images of vesicles and individual micrographs. Moreover, the video mosaicing methodology and automatic segmentation are tested on an actual experiment with cobalt-ferrite nanoparticles. Lastly, an experiment with vesicles and fullerene nanoparticles is analyzed to reveal some influences nanoparticles can induce.

The presented development and verification of this methodology is the first step in a new branch of the vesicle–nanoparticles interaction research. Results of its future applications in various settings will reveal its narrow or wider applicability to the vesicle research and potentially shed light on what their interactions with nanoparticles are.

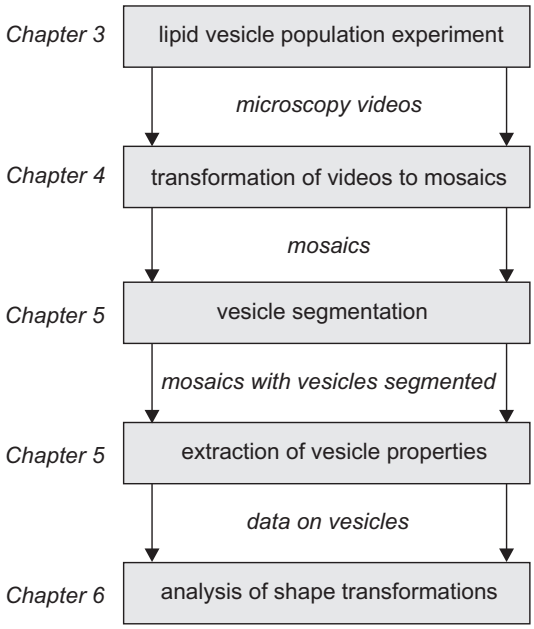

Figure 1.1 An outline of the proposed methodology. Shaded boxes present the steps in the methodology and the text in italics gives the outputs of these steps. The text in italic on the left of the shaded boxes points to the chapters of this thesis where the associated step is described in detail.

1.2 Contributions to Science

The following contributions to science are presented in this dissertation:

1. We propose a new methodology for investigating the influence of agents on giant unilamellar lipid vesicles. The main contribution is the recording protocol, especially the use of vesicle populations instead of single vesicles, which is the currently broadly used approach.

2. We show that this methodology can be successfully applied to an experiment where interactions between nanoparticles and lipid vesicles are observed. The resulting analysis is meaningful and informative.

3. As the core of this methodology, several steps for creating mosaics with best representations of the vesicles from the microscopy video sequence are proposed. Most importantly, the hierarchical approach to registering frames and moving vesicles in them via two-step rigid registration in video sequences of lipid vesicles.

4. We introduce an adaptation to the Markov random field model for segmenting multiple lipid vesicles from micrographs or mosaics and test it on data acquired from a lipid vesicle population experiment where thousands of lipid vesicles are observed and analyzed.

Parts of work presented here have been published at two international biomedical IEEE conferences [1, 2], in a new and emerging international nano-science journal [3], a top optics journal [4], a journal on liposome research [5], in a Slovenian medical journal [6], and presented at Northeastern University (April 2010, May 2011), Max Planck Institute for Biological Cybernetics (February 2011), and Harvard University (April 2011).

2 Bio-nano interaction studies

2.1 Nanotechnology and nanoparticles

"What I want to talk about is the problem of manipulating and controlling things on a small scale."

— Richard Feynman, *There's plenty room at the bottom*[1], 1959

[1] Richard Feynman was an American physicist, a Nobel laureate, who during his lifetime became one of the best-known scientists in the world. Besides many other things, he has been credited with introducing the concept of nanotechnology [7]. "There's plenty room at the bottom" was a talk he gave on December 29th, 1959, at the annual meeting of the American Physical Society at the California Institute of Technology (Caltech) and has since become a classic. Feynman considered the possibility of direct manipulation of individual atoms as a more powerful form of synthetic chemistry than those used at the time. The full transcript is available at http://www.its.caltech.edu/~feynman/plenty.html

Today, more than fifty years after the famous Richard Feynman's talk, nanotechnology is becoming a full blown industry. One of its most prominent fields, where the novel consumer products are constantly emerging, are the nanomaterials, defined as substances that have at least one critical dimension less than 100 nanometers. At this scale, the materials' physical properties change which makes nanoparticles very useful for a vast range of applications in medicine, cosmetics, electronics, energy production etc. [8]. Some interesting current and potential future applications of nanotechnology are presented in Fig. 2.1.

However, there is a catch. Due to the properties (optical, magnetic, electrical etc.) that distinguish them from similar materials made up of larger particles, nanoparticles also carry certain undertones due to lack of their health risk assessment. Even though nanotoxicology is already an emerging field it is beginning to face certain difficulties

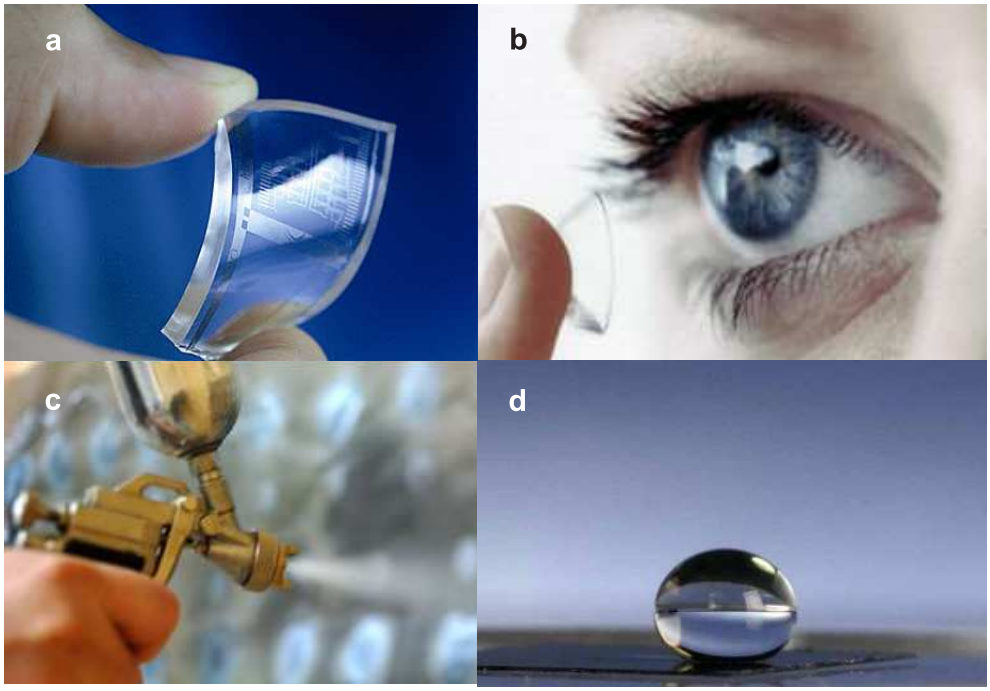

Figure 2.1 Examples of current or potential nanotechnology applications. (a) Graphene from gases for bendable electronics, (Photo by Ji Hye Hong), (b) contact lenses with nanoparticles show diabetics blood sugar, (c) a blue semiconductor mixture is sprayed onto paper coated with silver cathode dots to demonstrate the ease with which solar cells can be fabricated in the field. Connect the cells with a few wire electrodes, and a solar cell array is born (Photo courtesy of John Anthony). (d) A drop of water balances perfectly on a plastic surface covered with nano fibers (Photo by Jo McCulty, courtesy of Ohio State University).

which are not present in assessing toxicity of bulk material but arise with nanoparticles. The diversity of chemical compounds used to make nanomaterials, coupled with the huge variety of their properties, means that no one even knows how to classify them in a way that allows general conclusions to be drawn from studies on particular ones. Nanoparticles of the same matter come in a variety of different sizes, making the studies on their risk assessment difficult to compare. Even a small change in experimental conditions can lead to huge differences in the study outcome [9]. The development of a global database on biological reactivity/inertness and toxic potential of nanoscale particles is needed in order to support development, application and life cycle of these new products in terms of safety. In this respect, there is still a huge gap to fill especially when it comes to nano risk assessment methodologies [10–12].

The nanoparticle-related effects depend on particle surface area, numbers of particles and in a large part also to their surface chemical characteristics. When in contact with biological systems, much evidence suggests that nanoparticles first interact with cell membranes and subsequently provoke a cascade of cellular events. They can effectively disrupt cell membranes by nanoscale holes, membrane thinning, and/or lipid peroxidation. Recent reports provide evidence on in vivo and in vitro effects of nanoparticles on membrane stability [13, 14]. It is expected that existing in vitro tests designed for testing toxicity of soluble chemicals are appropriate also to assess toxic potential of nanomaterials [15]. However, a simple biological system is needed to allow studies of solely nanoparticle-lipid membrane interactions. For such purposes, studies with giant lipid vesicles are a promising direction [16].

2.2 Giant unilamellar lipid vesicles

Lipid vesicles are bubbles made out of the same material as cell membranes. They are highly adaptive structures with a rich diversity of shapes which can be formed at various sizes as uni- or multi-lamellar constructions. In the last decades, they have become objects of research in diverse areas that focus on cell behavior. This is mostly due to their ability to provide insights into a variety of vital cell processes, especially those linked to biological membranes (for a review see [17, 18]). By their size, they can be roughly classified into three distinct groups:

- small unilamellar vesicles (SUV) with diameters smaller than 200 nm,

- large unilamellar vesicles (LUV) with diameters between 200 nm and 5 μm,
- giant unilamellar vesicles (GUV) with diameters between 5 μm and 200 μm.

Most experimental evidence on membrane behavior is provided by giant unilamellar lipid vesicles (vesicles) (for a review see [19]). Due to their size, which is on the same order of magnitude as that of cells, they are surrogates for cell membranes and can be observed with a light microscope [20]. Research on vesicles is extensively focused on their conformational behavior and considers preferred shapes, shape transformations, and fluctuations [21–26]. Even minute asymmetries in the lipid bilayers can cause high spontaneous curvatures and vesicle deformations, causing its shape to range from spherical to pears, cup-shaped, budded and pearls [21]. Numerous lipid vesicle based research activities focus on investigating their morphological transitions induced by different agents (electric or magnetic field, chemicals) [27]. Different authors report that in the presence of agents or if external conditions such as temperature or osmotic pressure are varied, vesicles undergo distinct shape changes from one class of shapes to another [24, 28]. Changes and fluctuations in the shape of vesicles have been widely investigated by various techniques, most commonly optical microscopy [24, 29]. Some of the commonly used microscopy techniques are presented in Fig. 2.2.

The preponderance of published research focuses on observing single vesicles [24, 29–31] and the detailed inspection and theoretical description of vesicle membrane deformations [32, 33]. In such studies one vesicle is chosen and isolated, and its morphological behavior is recorded. Even though isolated single giant lipid vesicles provide good specimens for such observations, there are limitations. For example, *in vivo* and *in vitro* interactions with nanoparticles are a special topic in biology and differ from interactions with non-nanoscale chemicals [11, 15]. The response in these interactions can differ from one vesicle to another, and this is why beside tracking a single vesicle's behavior, we are also interested in the general response of a vesicle population. Due to high sensitivity, vesicles may be dynamically transformed in shape and size in response to small changes in experimental conditions [27]. Therefore we need methods which would enable investigation of a large number of vesicles and thus the analysis on the scale of a vesicle population.

2.3 Bio-nano interactions and motivation

Recently, research related to biological membranes has been gaining importance due to the products emerging from new technologies. These include drugs and diagnostic tools, as well as ingredients in food and cosmetics, whose primary reaction, at the nanoscale level, is with cell membranes. These products have many beneficial effects but may also provoke a toxic response [34]. It was shown that nanoparticles interact strongly with cell membranes [13, 35, 36] and that artificial lipid vesicles, including giant unilamellar lipid vesicles offer a simple biological system with which to study interactions between nanoparticles and biological vesicles [3, 34, 37]. Interactions of nanoparticles with lipid vesicles that have been studied so far reveal that nanoparticles induce lipid surface reconstruction [38], physical disruption of lipid membranes [39–41], and shape transformations of lipid vesicles [16].

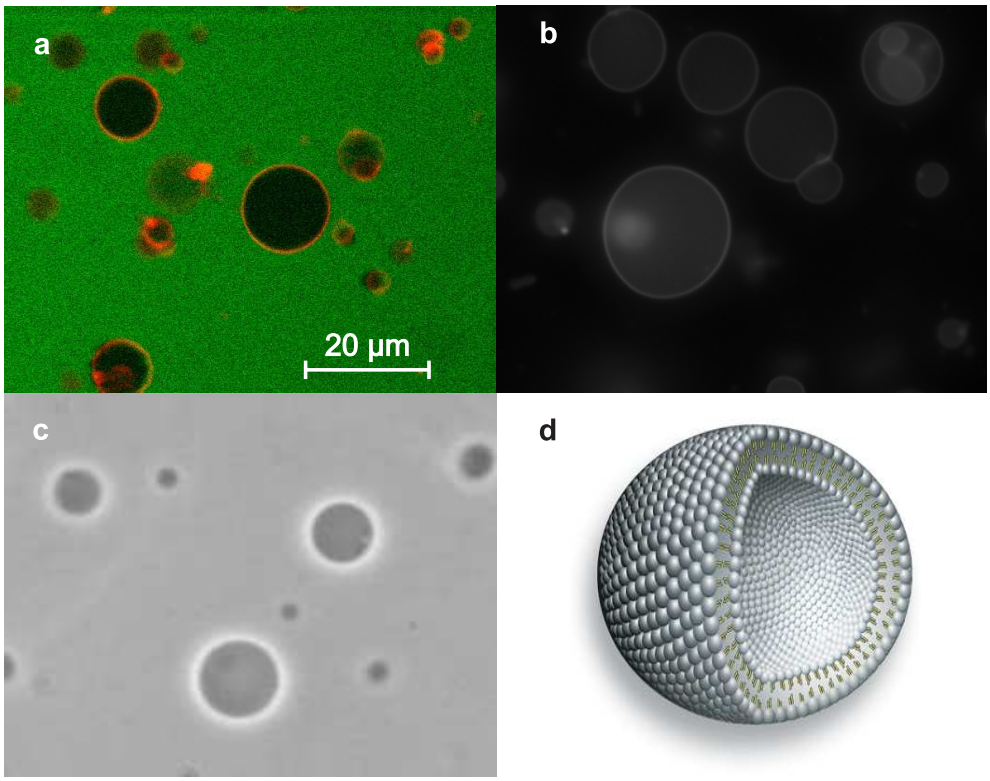

Figure 2.2 (a) Fluorescence microscopy with Apotom apparatus, with added colors, (b) fluorescence microscopy with Apotom apparatus, (c) phase contrast optical microscopy, and (d) a schematic model of a giant unilamellar lipid vesicle.

Analysis of vesicle populations has also been considered. For example, routine vesicle size analysis is carried out by photon correlation spectroscopy (PCS) using commercial instruments. This technique gives a measure for the mean size of the vesicles. Although PCS allows in principle the determination of particle size distributions, the reproducibility and reliability of the method for calculation is insufficient. Quantitative determination of the liposome size distribution, thus, is still difficult. Although a number of powerful approaches like electron microscopy, ultracentrifugation, analytical size exclusion chromatography, and field-flow fractionation have been suggested, none of these approaches has found widespread use due to various limitations. Instead, we propose a study of the changes of populations of lipid vesicles by taking advantage of a possibility of direct observation of the vesicles (phase-contrast optical microscopy) combined with computer aided image analysis approach. The first step is to prepare an experiment protocol for gathering the data on vesicle populations.

3 Experiment

3.1 Experiment overview

We conducted multiple experiments with lipid vesicle populations investigating various additives during our research on this topic. However, in this dissertation we focus on two of them, the C_{60} (fullerene nanoparticles) and the $CoFe_2O_4$ (cobalt–ferrite nanoparticles) experiments. In the context of our automated methods, the only difference in protocol between these two experiments is that in the case of C_{60} we record individual micrographs of the vesicle population, whereas with $CoFe_2O_4$, each track is recorded in a video sequence instead. In the context of bio-nano interactions, some other protocol elements and settings varied which are presented in Tab. 3.1. If not specifically mentioned, the settings and approaches described in this chapter, are the same for both experiments.

Experiment	Recording type	Time at recording [min]	Reference agent
C_{60}	810 micrographs	1, 10, 100	$ZnCl_2$
$CoFe_2O_4$	6 video sequences	1, 90	no agent

Table 3.1 Differences between the two experiments analyzed in this dissertation.

3.2 Vesicle preparation

Giant unilamellar phospholipid vesicles were prepared from 1-palmitoyl-2-oleoyl-sn-glycero-3-phosphatidylcholine (POPC) and cholesterol, combined in the proportion of 4:1 (v/v) at room temperature by the modified electroformation method [42] as described in detail elsewhere [43]. Dissolved lipid mixture (40 μl) was spread over a pair of platinum electrodes. The solvent was allowed to evaporate in low vacuum for 2 hours. The coated electrodes were then placed 4 mm apart in an electroformation chamber (Eppendorf cup) that was filled with 2 ml of 0.3 mol/l sucrose solution. An alternating electric field of magnitude 1 V/mm and a frequency of 10 Hz was applied to the electrodes for 2 hours (Fig. 3.1).

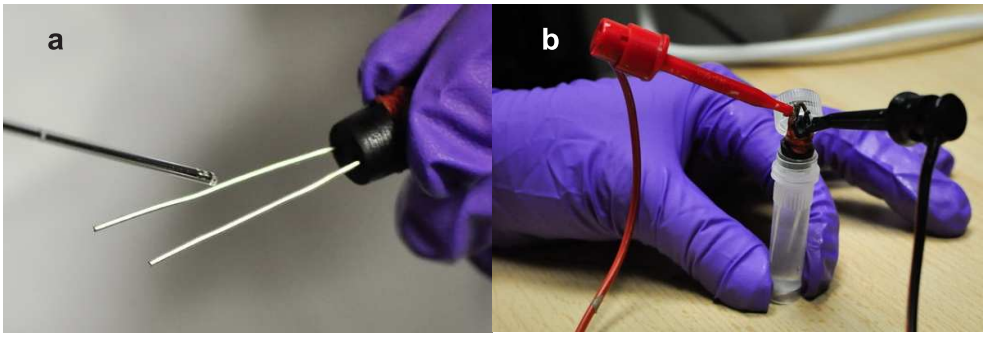

Figure 3.1 (a) Dissolved lipid mixture was spread over a pair of platinum electrodes. (b) The coated electrodes were placed 4 mm apart in an electroformation chamber (Eppendorf cup) that was filled with a sucrose solution. An alternating electric field was applied to the electrodes for 2 hours.

Then the magnitude and frequency of the alternating electric field was gradually reduced, first to 0.75 V/mm and 5 Hz, then to 0.5 V/mm and 2 Hz, and finally to 0.25 V/mm and 1 Hz (all applied for 15 minutes). After the electroformation, 600 μl of 0.3 mol/l sucrose solution containing electroformed vesicles was added to 1 ml of 0.3 mol/l glucose solution in an Eppendorf cup. Before the experiments, the vesicles were left to sediment under gravity in a low vacuum at room temperature for approximately 24 hours.

3.3 Experimental protocol

The following steps were performed on the day of the recording, 24 hours after the start of vesicle sedimentation. By turning the Eppendorf cup upside down three times, the vesicle solution inside was gently mixed. A 45 μl drop of this solution was then administered into an observation chamber made from a pair of object glasses. The larger object glass (26 x 60 mm) was covered with a smaller cover glass (18 x18 mm), and a strip of silicone paste was applied to the two sides to act as a spacer between the glasses (Fig. 3.2a). Preliminary experiments showed that the small negative buoyancy of the vesicles causes the collection of vesicles at the bottom of the suspension during the first 5 minutes. A scheme of a cross section of the glasses and the vesicle population is given in Fig. 3.3b. This was previously also observed in [3, 33]. This allowed the operator to observe a majority of vesicles in the field of view when the microscope focal plane was set to the plane with the vesicles. Some steps of the experiment are depicted in Fig. 3.2.

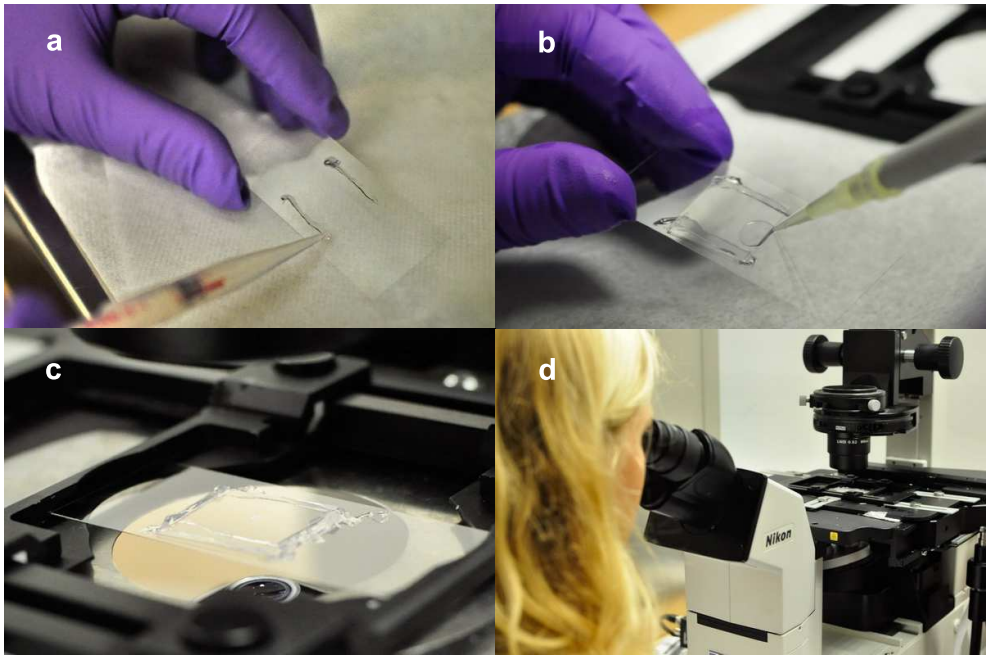

Figure 3.2 (a) A strip of silicone paste is applied to the object glass. (b) A drop of the vesicle solution is administered into an observation chamber made from a pair of object glasses and separated by silicone paste. (c) The object glass with the vesicle solution is attached onto the microscope slide. (d) The vesicle population is observed and recorded by the operator.

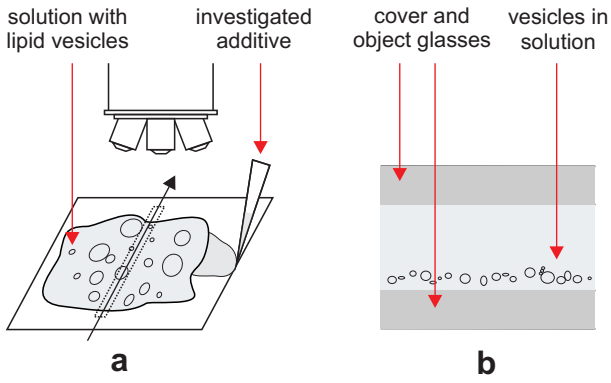

Figure 3.3 (a) The solution with lipid vesicles on the object glass is covered with a glass plate, and the suspension with the investigated additive is added. The place where the videos are recorded is shown and the arrow shows direction of recording. (b) Transverse section of the object and cover glasses and the suspension with lipid vesicles. A majority of the vesicles are in the same focal plane, at the bottom of the observation chamber. The scheme is not to scale.

The observation chamber with the vesicle solution was attached onto the microscope slide and places for acquiring the micrographs were chosen. Each place is a vertical track where the vesicle population is recorded. The position of the track is relevant to the place of adding the glucose solution (with or without nanoparticles), which is at the edge of the vesicle solution (Fig. 3.3a). By acquiring the micrographs at the same distance from the addition of the solution, we enable the observation of changes in the vesicle population. In the C_{60} experiment, two places were chosen for recording of each population at every time of incubation (1, 10, and 100 minutes). The first place (P1) was near the place of the addition and the second place (P2) was further away. Capturing two samples of the same population is interesting for comparison of the population changes at two different concentrations of the additive. At the place of addition (P1) the concentration is higher than further away (P2) because of the concentration gradient. In the experiment with $CoFe_2O_4$, only track P1 was recorded.

In the case of recording micrographs (the C_{60} experiment), series of 15 were taken at every track (Fig. 3.3a). The reason for recording only a small number of micrographs is because of the time constraint when recording a dynamic system. The 15 micrographs covered only approximately 15% of vesicles in our region of interest with this approach in the time available (up to 5 minutes). This was the primary reason why we decided to record video sequences instead in all future experiments (also $CoFe_2O_4$). This allowed

a six-fold increase in the captured area of the track (a video sequence captures 100% of the track at a single place). Both, 1-dimensional video tracks ($CoFe_2O_4$) and individual micrographs (C_{60}) of specimen, were recorded at 400x magnification. The width of view at this magnification is 200 μm and height 150 μm. The length of a single recorded track was approximately 1 cm. With these tracks we captured a subsample of the population where all vesicles of a single track were at approximately the same distance from the place where the nanoparticles or a reference chemical had been added.

3.4 Chemicals

Synthetic lipids, 1-palmitoyl-2-oleoyl-sn-glycero-3-phosphocholine (POPC) and cholesterol were obtained by Avanti Polar Lipids, Inc. (Alabaster, Al, USA) and dissolved in a mixture of chloroform and methanol solvent, combined in the proportion of 2:1 (v/v). Sucrose solution (0.3 M) was prepared with distilled water. By adding 10 ml of sucrose with 90 ml of water would result in 0.1 M. Glucose solution (5%, for intravenous applications) was purchased at Krka, d.d. (Novo Mesto, Slovenia). Fullerenes (C_{60}) and sucrose were purchased at Sigma-Aldrich (Steinheim, Germany). $ZnCl_2$ was purchased from Merck & Co., Inc. (New Jersey, USA). All vesicle preparations and experiments were conducted at the Laboratory of Biophysics, Faculty of Electrical Engineering, University of Ljubljana.

The $CoFe_2O_4$ nanoparticles were prepared by Asst. Prof. Darko Makovec. They were synthesized by co-precipitation using NaOH from aqueous solutions of Co(II) and Fe(III) ions at elevated temperatures. The samples of $CoFe_2O_4$ were thoroughly washed with water and suspended in an aqueous solution of glucose. The nanoparticles in suspension agglomerate strongly and such agglomeration must be prevented in order to prepare stable suspensions of the nanoparticles. To achieve this, citric acid was adsorbed to the surface of the nanoparticles. The nanoparticles have relatively broad size distribution ranging from 5 to 15 nm. The smaller nanoparticles are globular, while the larger are octahedral in shape. Energy dispersive x-ray spectroscopy (conducted by Bionanoteam, supervised by Prof. Damjana Drobne) showed their stoichiometric composition to be $CoFe_2O_4$. The effects of both non-coated cobalt-ferrite nanoparticles (CF) and the negative citrate-coated cobalt-ferrite nanoparticles (CF-CA) were investigated.

3.5 Hardware and software components

All processing was performed on a PC with a Quad CPU at 2.33 GHz, 8 GB RAM, on Windows Server HPC 64-bit edition, 2007. The image processing algorithms were developed in Matlab 2009b (MathWorks, Massachusetts, USA), the ImageJ [44] plug-in "Shape Segmenter" was developed in Java with the use of the environment Eclipse (Eclipse Foundation, Ontario, Canada). Microsoft Excel 2007 (Microsoft Corporation, Washington, USA) and Matlab were used for statistical analysis. The invert microscope used was a Nikon Eclipse TE2000-S with an attached Sony CCD video camera module, model: XC–77 CE.

4 Video microscopy to mosaic

4.1 Introduction to microscopy mosaicing

"Seldom does a photograph record what we perceive with our eyes. Often, the scene captured in a photo is quite unexpected – and disappointing – compared to what we believe we have seen. A common example is catching someone with their eyes closed: we almost never consciously perceive an eye blink, and yet, there it is in the photo – *the camera never lies.* Our higher cognitive functions constantly mediate our perceptions so that in photography, very often, what you get is decidedly *not* what you perceive. *What you get,* generally speaking, is a frozen moment in time, whereas *what you perceive* is some time- and spatially-filtered version of the evolving scene." (Agarwala et al., 2004 [45]).

4.1.1 Image stitching in general

As a photograph could, in general, be a frozen moment in time, a mosaic almost never is. It is rather a filtered version of the evolving scene. In most cases, a mosaic consist of two or more subsequently recorded images, stitched together to present a scene, larger

than it can be captured with a single field of view of the imaging system and thus preserve or maximize its achievable resolution. The history of mosaicing is nearly as old as the history of photography itself. It has been practiced at least since the mid-nineteenth century, when artists like Oscar Rejlander [1875] and Henry Peach Robinson [1869] began combining multiple photographs to express greater detail [45]. However, the digitalization of images and computerization of procedures vastly contributed to usability of mosaics in applications.

Currently, the number of publications concerning the mosaic stitching is enormous. At the time of writing the dissertation, the Annotated Computer Vision Bibliography[1] lists hundreds of papers related to mosaics and panoramas, tens of different mosaic or panorama generation software programs and even cell phone applications [46]. Uses in science and everyday life are too numerous to list here, however a few examples are presented in Fig. 4.1 (figure sources: a[2], b[3], c[4], d[5], e[6]). There is no doubt that now photographers are able to easily create the illusion of a wide lens picture by seamlessly stitching together a set of wisely pointed pictures taken with low cost camera gear. Just to mention a few commercial software solutions for image stitching: AutoStitch[7], AutoPano[8], PTgui[9], Panotools[10].

In some literature, the term *image mosaic* is used to describe a collection of small images arranged in such a way that, when they are seen together from a distance, suggest a larger image of a completely different content. Such terminology is a confusion, and such techniques should be referred to as *photomontages* [47]. Also, terms *panorama* and *mosaic* are often used equally for all image stitching applications and techniques, which can lead to a misunderstanding. In a communication with Prof. Richard Szeliski[11], we concluded that this confusion exists, and that better definitions on what exactly each of the terms represents should be determined. To make a clear distinction and present the choice of using the term *mosaic* for the application in *this dissertation*, we note

[1] http://www.visionbib.com (Mosaic Generation, Image Stitching, Panorama Creation).
[2] Mars vista from Rover, Nasa, http://www.nasaimages.org.
[3] Charles Darwin by Charis Tsevis 2009., http://www.flickr.com/photos/tsevis/3288860652.
[4] Polyp slide, Sessile Serrated Adenoma Polypectomy Specimens: 8 Cases, *Am J of Clin Path* 2006.
[5] Winter Sky Panorama by Alan Dyer, 2010, http://www.flickr.com/photos/iyacalgary/4284808421.
[6] Aerial view of Ljubljana, Google Maps, http://maps.google.com.
[7] http://cvlab.epfl.ch/ brown/autostitch/autostitch.html
[8] http://www.autopano.net/en/
[9] http://www.ptgui.com/
[10] http://panotools.sourceforge.net/
[11] The communication consists of emails between the 19th and the 21st of January 2011.

Figure 4.1 All images above are members of some sort of stitched images. (a) A panorama of Mars vista stitched from photos acquired by the NASA Mars exploration Rover, (b) a photomontage of small images of various life forms from evolution that all together represent a portrait of Charles Darwin, (c) a microscopy mosaic of a Polyp slide, (d) an astronomy panorama of a night sky, (e) an areal view of Ljubljana.

that: both, a panorama and a mosaic are representations of a *real scene*, stitched from *multiple images*. Moreover, they contain a larger representation of the scene than can be captured with a single field of view of the imaging system. The difference is that in a mosaic, all images depict a *flat subject* and are taken each from a *different point of view*. In this context, a panorama could be described as a general (non-flat) scene (e.g.outdoor environment or room) stitched from photos taken from a single location but with the camera looking in different directions. In the presented dissertation, the term mosaic will be used throughout the dissertation as it is the closest to the actual problem presented. Most of the approaches discussed, however, could be used for stitching panoramas as

well.

In the process of stitching a mosaic, the objective is usually to create a visually pleasing result. In this case, visually pleasing refers to a mosaic that looks like it could have been recorded as a single image by an imaging system with a greater field of view and resolution. To achieve this, after the images of the scene had been recorded, several technical problems are usually encountered [48]:

- registering all images in the sequence and creating a mathematical transformation model which morphs images and places them into the mosaic of the scene,
- choosing good seams between parts of the various images so that they can be joined with as few visible artifacts as possible,
- reducing any remaining artifacts through a process that fuses the image regions.

A thorough review of current approaches for solving specific problems will be given in each section where, through our application, these problems are encountered.

4.1.2 Mosaicing in microscopy

Microscopy mosaicing and related techniques fall in the general areas of computational microscopy, image processing, biomedical optics and biomedical informatics. In the last decades mosaics have been gaining popularity not only among photographers, but also among scientists in various areas. This is partially due to the fact that such software enhanced approaches can broaden the utility of existing and available hardware without the need to upgrade. For example, in optical microscopy, a high resolution analysis of a specimen in the size of several centimeters is impossible even if cameras with greater resolutions are employed. The alternative is to acquire multiple images at a greater magnification and then stitch them together so the whole specimen can be observed without the loss in resolution. This method is often termed large scale microscopy. When only a few images are necessary to record the whole sample, they can be stitched together manually with the use of a photo processing tool such as Adobe Photoshop (Adobe Systems Incorporated, California, USA) or Gimp. Dedicated automated stitching software solutions (listed in § 4.1.1) are also applicable to microscopy, however, when hundreds of micrographs are necessary to cover the specimen, multiple problems arise.

Specifics of micrograph recording for mosaicing

Just as in all mosaicing (and image processing in general) applications, the protocol for image acquiring is crucial. At this stage, a proper procedure can greatly reduce post processing steps required during later mosaicing. First, there needs to be some overlap between the images to enable later image registration (§ 4.4). Second, the experimental lighting conditions should be constant, and lastly, there is the choice of focus and depth of field. As the number of images needed for the mosaic increases, manual imaging becomes increasingly difficult. This is where automated image acquiring procedures, commonly termed *virtual microscopy*, such as large slides using a motorized microscope stages that move and focus the slide automatically are employed [49–51].

Specifics of mosaicing from micrographs

When acquiring micrographs, the choice of a viewpoint is usually fixed due to the fixed optics of microscopes. This means that no perspective distortions or scale changes are present in the recorded micrographs and rotation is rarely present, making the geometrical modeling of micrograph registration somewhat less cumbersome than e.g. outdoor panoramas [52]. On the other hand, when multiple micrographs of parts of a certain specimen are acquired, they usually look very much alike. Without any (at least approximate) information on the global position of individual micrographs, their registration will almost inevitably produce incorrect results. This is why mosaicing tools (stitching software) dedicated to microscopy take manual positioning or scanning stage positions of the microscope as an input prior to registration [53]. Some notable comparisons of manual, commercial, open source and dedicated solutions to stitching of micrographs are in [49, 54] and some recent applications [55–57]. An extensive feature by feature comparison of freely available software is in [53].

Another specific of mosaicing in microscopy is that the number of micrographs recorded of a specimen is considerably greater than, for example, the number of photographs in a panorama of a countryside scenery. Consequently, mosaicing of these large datasets is very time and memory intensive, which is one more reason why many dataset-specific optimized mosaic stitching algorithms are still being developed, instead of everybody using a single one-size-fits-all solution.

4.1.3 Specifics of the presented mosaicing approach

Acquisitions of micrographs and mosaicing techniques already presented in this chapter find various and plentiful applications in biology, medicine and other fields. However, most of the *in vivo* and *in vitro* microscopy discussed is focused in observing static specimens while the vesicle population employed in our experiments is a dynamic specimen. Besides the local independent movement of the vesicles, the vesicle population changes in time. The vesicles can increase or decrease in size, change shapes, burst, split, or merge to produce new shapes. As these time dynamics are one of the major interests in our experiments, the micrographs to form a single mosaic should be acquired in a short duration of time, preferably in less than 5 minutes. The whole area we want to capture is approximately 1 cm long and 200 μm wide. In the C_{60} experiment [3], the 15 micrographs captured cover only 15% of the track, whereas with microscopy video sequence, we are able to capture the whole 100% of the track.

Without a change in magnification, the whole area could be covered in the desired time frame by adapting the imaging system hardware with a moving slide to capture the micrographs. With such an automated hardware, recording of the area would be feasible in the desired time. However, this approach would limit the usability of the developed procedure and protocol to a single imaging station. Not only that the protocol and methodology would not be distributable to other laboratories, every change in our own hardware system would result in a need to also upgrade the sliding mechanism. Moreover, the current software solutions for automated micrograph recording are very time consuming. For example, after the operator outlines the shape to be captured, adjusts multiple focusing points for focus interpolation throughout the image, exposure correction and other settings for optimal outcome, the software takes care of the photographing and stitching, all together requiring multiple hours. Such procedures are not suitable for the dynamic nature of our experiment where the data has to be acquired in a short time frame, but still contain all the information required for stitching a mosaic. Employing video microscopy solves both issues and is our preferred choice. Besides not requiring any hardware modifications, this way the methodology (the recording protocol and software) is completely portable. Any operator with a microscope only acquires the video sequences following the here presented protocol, and we are able to stitch the videos into mosaics using the presented algorithms.

4.1.4 Video mosaicing

This section summarizes some problems one encounters when stitching a mosaic from a video sequence and various solutions that can be found in recent publications. With a still camera, users typically only capture up to a dozen images to create a panorama. However, with a video camera, it is easy to generate thousands of images each minute. One such example of time efficient frame registration is in digital image stabilization solutions, useful for videos acquired by cell phones without optical image stabilization [58]. Even more so, because motion stabilized videos can be compressed better. A helpful circumstance in video registration is the progression of frames, where camera motion can be used to inform us on the movement direction and thus direct the most probable geometrical transformations in the frame sequence. This is partially exploited by Steedly et al. [59], as they limit the registration to temporally neighboring frames only. Besides the vast quantity of frames, another problem in video registration is the distortion of moving objects which need to be detected in the video sequence and then blended onto the panorama as only one instance (see Radke [60] for a survey of image change detection methods). Even though normal panoramas also deal with this issue, it is more evident in videos as an object can be moving in and out of tens or hundreds of frames [61]. One common solution is to draw seams around objects using Dijkstra's algorithm [62], segmenting the mosaic into disjoint regions and sampling pixels in each region from a single frame only.

When stitching a video sequence, every pixel of the mosaic is present in multiple frames. Hence, one has to make a choice whether to use some sort of blending of all those pixels or to choose only one of the video frames as the source. Choosing every pixel individually from an independent frame can produce very noisy mosaics, and blending all sampling pixels can result in a very smooth mosaic with a loss in detail. Both approaches are prone to the ghosting effects [48]. In this respect, a choice of a region based approach is preferable although it also comes with downsides. The transitions between regions usually produce an intensity inconsistence demonstrated as an edge. This problem is best approached with gradient domain fusion [48, 63], where boundary conditions are set in adjacent regions and the transition is interpolated using Poisson blending [64].

In microscopy, video mosaicing has not been widely explored. Vercauteren et al. used fibered confocal microscopy to stitch a mosaic of a live mouse colon (cancer research)

[65]. Also, Backer et al. used a fibered fluorescence probe to *in vivo* assess nerve fiber density of a mouse [66], again the video sequence was stitched into a mosaic.

Interesting *relatives* of the usual panoramas and mosaics are the panoramic video textures. These are created by taking a single panning video, and stitching it into a single wide field of view that appears to play continuously and indefinitely [63]. On top of the usual video mosaicing steps, solving this problem includes tackling with dividing the scene into dynamic and static portions and looping them during the times when they were not recorded.

4.2 Video to mosaic algorithm outline

Stitching the video sequences acquired in the lipid vesicle experiment into mosaics is a challenging problem. Even more so, because the applied example of lipid vesicles is a real and dynamic dataset recorded by a human operator. In this respect, for achieving satisfactory result of mosaic stitching, some steps were required, which are very dataset specific. For example, frame noise removal was required because the image system used contained some impurities. Some measures and classification models used (removal of distorted frames, vesicle sharpness measure) are also specific for the lipid vesicles domain, and would need at least minor, if not major modifications in order to be successfully applied to other video microscopy domains.

On the other hand, some steps described are more general and could be applied to multiple video microscopy domains. The combination of global frame registration and local object registration could be applied to any microscopy sequence containing multiple objects, each with its own trajectory. Dividing the memory intense video dataset into multiple manageable buffers, and Poisson blending of sharpest representations of vesicles from multiple frames into a mosaic are general as well. Not to get caught in the details, we try to present the usabilities of each step in the corresponding sections. At this point it is only fair to comment that we do not assert that this is the ultimate or optimal video to microscopy methodology, although it is to our best knowledge the first implementation of image processing steps for the purpose of mosaicing video sequences of giant lipid vesicles. For a better understanding of steps involved in our mosaicing, we present an outline of the algorithm in Fig. 4.2. The input to this algorithm is a video sequence of approximately 5 minutes of a selected track recording (containing a population of lipid

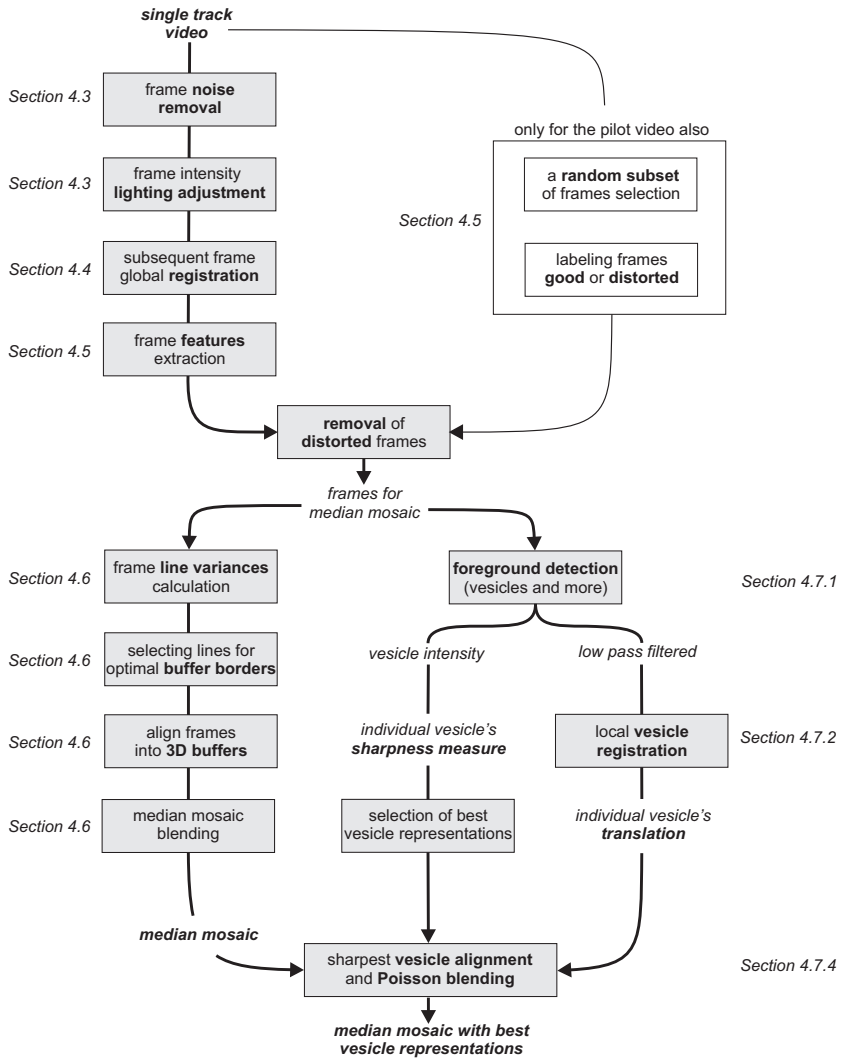

Figure 4.2 An outline of the steps required for transforming a video sequence to a mosaic. Boxes represent processing steps and the text in italics their outputs. Only the first (pilot) video sequence of the experiment is used for training classifiers in the non-shaded steps, while the shaded steps are required for all videos. The text in italics at the sides notes the section of this dissertation describing the step in detail.

vesicles). The output of mosaicing is a single, sharp mosaic, stitched together from the selected frames of the video sequence. Some steps of the mosaicing were necessary only for the first video sequence, which involves the training of classifiers for frame quantity reduction. The models (classifiers, measures) generated in these steps can subsequently be used on all remaining video sequences of the experiment. Here, we refer to this

video sequence of a single track used in training as the pilot video, a term which is used throughout the dissertation. The pilot video can be selected randomly among the videos recorded in the experiment.

4.3 Preprocessing of video sequences

Video sequences, 768 pixels wide and 576 pixels high, were acquired at a rate of 25 frames per second and compressed with DivX video compression. Each video was then split into a sequence of individual frames, 1500 for every minute. The videos were recorded with a color camera, but since the color channels contained no additional information, we converted all frames into grayscale intensity values with equal regard to each of the three color channels (RGB)[12]. All frames were de-interlaced with bicubic interpolation and one of every two de-interlaced frames was discarded since the information contained in both was very similar. All frames had a thin black region on the sides and were thus cropped to a size of 762 x 570 pixels.

4.3.1 Frame noise removal

Due to impurities in the microscope hardware (lenses, glasses, camera), some artifacts appeared in all frames of the recorded video sequence (Fig. 4.3). Such artifacts together with thin layer occlusions are a common problem in photography. They are usually caused by physical layers of media (e.g. unwanted dust particles) between the recorded scene and the imaging system - in our case the camera sensor. For human tasks, such artifacts in images can be disturbing but not critical, as our visual perception system can reconstruct the obfuscated information in most cases. On the other side, artifacts can seriously aggravate automated computer vision tasks and should be removed from the dataset prior to further image processing.

In single-lens reflex (SLR) photography, dust particles often enter camera body because of frequent lens changing. Camera manufacturers solve these issues by incorporating anti-dust coatings to sensors, vibration-cleaning hardware and mapping out the occluding particles by software. When these pre-recording solutions fail, the result of such occlusions is a partially altered brightness or a dark artifact in the image of the

[12] $Intensity = \frac{1}{3} \times (red + green + blue)$

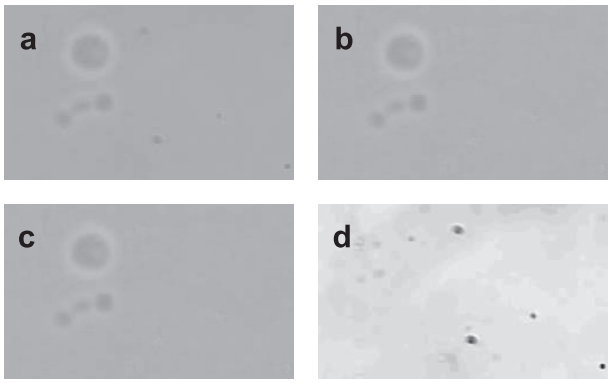

Figure 4.3 Figures a-d show the same part of a video frame. (a) Original image, (b) zero median result after removal of artifacts, (c) after de-interlacing, and (d) additive noise artifacts.

recorded scene. The approaches in removing the artifacts and restoring the image after it has been recorded, are dependent on various factors (number of different scenes recorded with same artifacts, properties of the artifact etc.). From a single image, the area around a partial occlusion can be recovered by modeling the radiance and estimating the background intensity [67]. When an area of a single image is completely occluded, and the intensity gradient in that area is not variable, a guided interpolation can be used to fill the missing area from the border intensities [64].

In case of multiple images with the same artifacts, it is common to model the lens noise from the continuity of occlusions in them [68–70]. As the video sequences of our experiments are continuities of frames, the images containing the artifacts are plentiful. To remove them, we first use the temporal median intensity filter to model the noise I_{noise} on a random subsample of 200 frames of the pilot video sequence. This way, the median value of pixels which were not obstructed by lens noise resulted in the median gray value of the background while the pixels representing lens noise appeared darker (Fig. 4.3d). To remove this additive noise from the video sequence, each frame I_{dirty} is filtered using:

$$\begin{aligned} I_{clean}(i,j) &= I_{dirty}(i,j) - [I_{noise}(i,j) - median(I_{noise})], \\ i &= 1...M, \\ j &= 1...N, \end{aligned} \tag{4.1}$$

where M and N are the height and width of the frame and $median(I)$ is the median

intensity value of the image I. The noise image, obtained from the pilot video sequence, was used to clean the noise from all other video sequences. As the noise image is inherent to the imaging system, it can be reused for all video sequences acquired with the same equipment.

4.3.2 Frame lighting adjustment

The lighting intensity over frames of the video sequences varies. Even though the changes are never more than 5% of gray intensity value, they should be adjusted to avoid later complications in the stitching and segmentation steps. If only mean intensity values of frames are observed, the real lighting conditions cannot be extracted due to lack of knowledge on the foreground objects. An excess presence of vesicles in one frame could alter its mean intensity in comparisson to a frame without vesicles. Instead of mean, median intensity values of the frames were compared and frame intensities were increased or decreased according to how their median intensity compared to the median intensity of whole mosaic.

4.4 Frame registration

An important step in every image mosaicing application is image registration. To register a series of images is to determine the ways in which they overlap. This way one can determine the appropriate mathematical model relating pixel coordinates in one image to pixel coordinates in another. The simplest case of an overlap is when two images can be aligned with only a simple geometric transformation. This is called a translation and consists of moving one image on top of the other so that the overlapping pixels of both images represent the same region of the recorded scene. More commonly, the geometric transformation between the images, required to align them, also includes scaling, rotation, projection and shear. These encumber registration, since the objects in the images cannot be directly compared.

In general, approaches to image registration can be divided into two categories: the direct and the feature based. The direct image registration is pixel based alignment where various error measures are used in order to minimize the pixel-to-pixel dissimilarities. On the other hand, feature based methods work by extracting a sparse set of features in all images and then matching only these instead of matching all pixels (see [71] for a review of feature detection methods). The feature based registration has the advantage of being

more robust against scene movement than the direct registration. An extensive review of image alignment and stitching is in an image alignment tutorial by Szeliski [48], a survey of image registration methods by Zitova et al. [72], and a review on registration of micrographs by Emmenlauer et al. [53].

The frames in the lipid vesicle population videos consist of a mostly uniform background with vesicles in the foreground. A majority of these vesicles, although being of various sizes, resemble each other in their spherical shapes. This detail is crucial for selecting the image registration approach. For instance, a feature based method with vesicle edges as features could find geometrical transformations between more frames in the video sequence than actually overlap in reality. This would lead to false alignment of frames. Hence, we chose to use the direct image registration over the feature based one. Also, the registration was performed on subsequent frames only and avoid false alignment of frames which are distant in the video sequence.

The video acquiring protocol for the experiment instructs the operator to record the video sequence in a single straight vertical track only. Even though such sliding of the object glass during the recording in our experiments is supposed to be 1-dimensional, the cumulative translation between the frames usually also reveals a small translation in the second dimension due to the mechanical imprecision of the object glass slider. However, in the experiments conducted this far, it was always smaller than 2% of the translation in the first dimension. There is no rotation or more complex transformations between frames. Here, translation between two consecutive frames is presented as a vector with two values, pixel translation in vertical and horizontal directions.

To calculate the translation between two frames, we take the peak value of the 2-dimensional normalized cross-correlation coefficient between the edge maps of each two consecutive frames. Moreover, proper filtering of the original images prior to edge estimation is a fundamental operation of image processing. A bilateral filter, which is an edge preserving smoothing technique, effectively a convolution with a non-linear Gaussian filter, with weights based on pixel intensities, is used [73]. This results in blurring of generally flat surfaces such as the background, and consequently removing small glitches and undesired specimens out of the focal plane, without the loss of information on distinctive edges, in this case, the vesicle borders. Frames are then transformed into edge maps with the Sobel edge detector [74], using default settings in Matlab 7.9.0, 2009b. We employ the 2-dimensional normalized cross-correlation on these edge values of two

k	1	2	3	4	5	6	7	8	9	10
Mean	0	0.103	0.243	0.353	0.478	0.635	0.726	0.842	0.951	0.986
Std	0	1.492	1.073	1.8529	2.186	1.9041	2.125	2.613	2.6052	2.6049

Table 4.1 Mean and standard deviation values of translation difference in the vertical dimension between frames in sequence given in pixels. Each frame of a video sequence (5000 frames) was registered against its $k = \{1...K\}$ successive frames where K was 10. Then the differences were calculated between the registered translation of frames i and $i + k$ and the sum of registering i to $i + 1$, $i + 1$ to $i + 2$ ... until $i + k$. The mean differences and the standard deviations are presented above.

frames instead of the intensity values when estimating the translation. The cumulative translations are then used to calculate the size of the mosaic. When the translations from the first to the i^{th} frame are summed, the sum represents the location of the top left corner of the i^{th} frame inside the mosaic.

This direct image registration is an approximation for the general translation of the object glass movement under the microscope and assumes the objects in the frames are static. The objects, in our case the vesicles, remain in the video sequence for as little as 2 seconds to as long as 10, a majority appearing for 5 seconds on average. Even though the motion of the object glass does not influence the vesicle motion (we confirm this by observing that vesicles do not express local motion in the same direction), there are still some noticeable local movements. These contribute to the fact that translation vector for every frame is a rough estimation of the position of object in the pixels of that frame. Fortunately, in our case the rough frame registration is sufficient for this step of mosaic stitching. We test this in a simple experiment where every frame of a video sequence is registered to 10 subsequent frames which follow in the video sequence (Tab. 4.1). These presented misalignments do not effect the stitching of the mosaic at this point. However, the local inconsistencies in alignment of individual vesicles (due to their movements in the dynamic environment) are noticeable. In order to correctly match the same vesicle in two distant but overlapping frames, those alignment issues are addressed with a local rigid registration step in § 4.7.2).

4.5 Selecting the best frames for mosaicing

Every vesicle was present in multiple consecutive frames, and the frame quality – the sharpness of vesicles in the frames – varied throughout the video sequence. When stitching a mosaic from a video sequence acquired by the presented protocol, there are many

frames with an overlap of 99% or more. It is crucial to discard the frames that hold imperfect or skewed information or hold no new information at all. However, no information on the vesicles should be discarded.

4.5.1 Removal of distorted frames

As the speed of object glass sliding was not uniform throughout the video, the moments when the object glass sliding was accelerated resulted in distorted frames. We designed a classifier to separate the sharp and useful frames from the distorted ones, which contained motion artifacts, presented in Fig. 4.4. First, we randomly picked a subset of 10% of all frames from the pilot video sequence and manually labelled them as "good" or "distorted", based on operator's observation. These labelled frames were used as a training set for a Linear Discriminant Analysis (LDA) classifier [75]. Both classes were equally represented in the training set. The LDA was used as the classifier because it provided a sufficiently accurate and generalized classification despite its simplicity. When deciding which features to use for classification, multiple measures previously proposed for autofocusing in computer microscopy [76] were compared. We calculated variance, contrast, entropy, Brenner gradient [77], and multiple image frequency based features for every frame of our video sequence. VizRank [78], a tool that automatically discovers and ranks interesting two-dimensional projections of class-labelled data, was employed to find the most promising features. Three features were selected. The first two were the Brenner gradient (Eq. 4.2) and the contrast feature (Eq. 4.3):

$$Brenner = \sum_{i=1}^{N-2} \sum_{j=1}^{M} [I(i,j) - I(i+2,j)]^2, \tag{4.2}$$

$$Contrast = \frac{\max_{i,j} I(i,j) - \min_{i,j} I(i,j)}{\max_{i,j} I(i,j) + \min_{i,j} I(i,j)}, \tag{4.3}$$

where M and N are the height and width of the frame, and $I(i,j)$ is the intensity value. The third feature is based on the amplitude of the absolute frequency contained in the columns of the frame. For every frame we compute the Absolute Frequency Amplitude Feature (AFAF) which is the mean of the area under the frequency curve (AFA_s) in the frequency bandwidth from s to 1 over the columns of a single frame, where $0 < s < 1$,

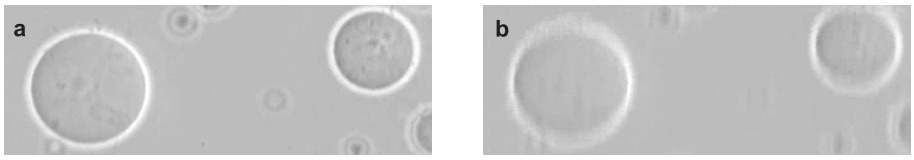

Figure 4.4 (a) The vesicles have a sharp border. Frames containing sharp vesicles were labeled as "good" for the purpose of our classifier. (b) The frames, where the same vesicles are distorted due to a motion artifact which occurred when the movement of object glass under the microscope was accelerated. For the purpose of classification, these frames were labeled as "distorted".

corresponding to lowest and highest frequencies of the column respectively. AFA_s is computed as follows:

$$\mathrm{AFA}_s = \frac{1}{N}\sum_{j=1}^{N}\sum_{f=s}^{1}|S_j(f)| \tag{4.4}$$

where $S_j(f)$ is the amplitude of the Discrete Fourier Transform (DFT) frequency f of the j^{th} column of the frame. The AFA_s is then normalized by AFA_0, the total absolute frequency amplitude under the frequency curve, which gives us the AFAF. In other words, the AFAF is the ratio between the high pass that covers the top 67% of the frequency band, and the total absolute frequency amplitude under the frequency curve of the column:

$$\mathrm{AFAF} = \frac{\mathrm{AFA}_{1/3}}{\mathrm{AFA}_0} \tag{4.5}$$

The optimal s values (0 and 1/3) for AFAF in our classification were selected by random sampling. This normalized measure (AFAF) is used as one of the three features for classification.

Employing these three features, the LDA classifier was used to separate the distorted and the good frames. On a training set of 500 labeled frames, using cross-validation, LDA was on average able to correctly classify 95% of frames. This classifier, trained on 500 frames of the pilot video sequence was then successfully used to classify frames of the remaining video sequences.

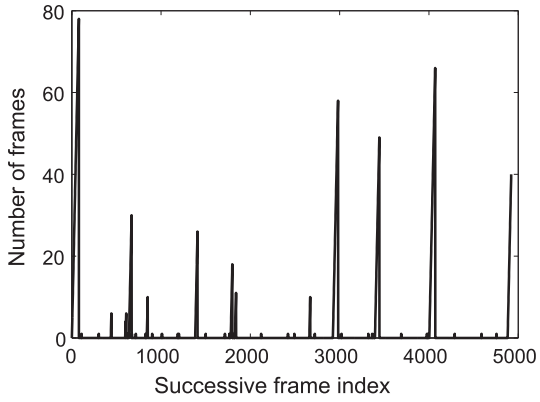

Figure 4.5 The data in the graph is from a video sequence of 5250 frames (3.5 minutes at 25 frames per second). Spikes in the graph present focusing locations where the spike height equals to the number of frames since last camera movement. The higher the spike, the more time (and consequently frames) was required for the operator to acquire a sharp image of the vesicles at that location.

4.5.2 Removal of focusing frames

Just as the sliding of the object glass was accelerated at some places, at some others there was no sliding at all. This is most evident in the parts of the video sequence, where the operator stopped and adjusted the focal plane to find the sharpest representation of the vesicles in view. Due to the focus adjustments, the number of frames representing the same area during the adjustment accumulated by 25 every second. However, because of changing focus, the representation of vesicles in these frames varied from out of focus to in focus. For the mosaic stitching, we decided to omit only the frames with the highest probability of being out of focus. We introduced a new, *focus measure* to compare subsequent frames for sharpness of vesicles (quality of focus).

The training procedure to acquire the focus measure was conducted as follows. Six different frame sequences of the pilot video sequence where the focusing occurred, presented as six highest peaks in graph (Fig. 4.5), were selected as data sets with 200 frames each. Some of the 200 frames represented the manual focus adjustment, and others were frames with same vesicles out of focus but with minimal slide movement. These six datasets (1200 frames altogether) were then used for training and testing of our Focus measure. These frames were manually labeled as the “good” frames (with vesicles in focus) or “focusing” frames (to be discarded). Similarly to our “good” vs. “distorted” classification of frames (Section 3.3.1), multiple features were computed for every frame

and VizRank was again employed to choose the optimal subset of features. The selected subset of features was composed of the Brenner Gradient (Eq. 4.2), the AFAF (Eq. 4.5) and Entropy:

$$Entropy = -\sum_{k=0}^{255} p(k) \cdot \log_2 p(k), \tag{4.6}$$

where $p(k)$ is the probability of $I(i,j) = k$ intensity in frame. LDA was again employed to classify the "good" from the "focusing" frames, but this time the trained classifier was not used for classification. The output of the LDA is a discriminant hyperplane which best separates the two classes. Projecting the feature vector of each micrograph onto the normal vector (vector inner product), which is perpendicular to the discriminant hyperplane, returns a scalar. In classification problems, a threshold has to be set to allow separating the classes. Instead, projections of the micrograph feature vectors is used as a measure to compare frames for focus quality. As it can be seen in Fig. 4.6, a greater focus measure value in a specific focusing situation can be associated with the frame which is generally more in focus. This focus measure is trained on the pilot video sequence and then also used to select the sharpest frames in the remaining video sequences. Wherever focus adjustments are encountered in a video sequence, the focus measure of all focusing frames is computed. Only the frames with the lowest value (the 10% most out of focus) are discarded from the mosaic stitching.

4.6 Buffered stitching

At the resolution of the video sequences in our experiment (768×576 pixels, cropped to 762×570 pixels), the average non-zero vertical translation between consecutive frames was 9 pixels, which is approximately 1.5% of the frame height, and suggests a 98.5% overlap between successive frames. At a duration of 5 minutes, which is the upper limit for our video sequence duration in this experiment, the video consists of roughly 7500 frames. Because our processing methods in Matlab require the image intensity values to be represented in a double format, the whole dataset requires $762 \times 570 \times 7500 \times 8$ B = 24 GB of RAM. In order to make our algorithms more general and applicable to different experiments and therefore potential longer video durations, we decided to break down the mosaic stitching into subsets of frames - *buffers* (Fig. 4.7). The accumulated memory

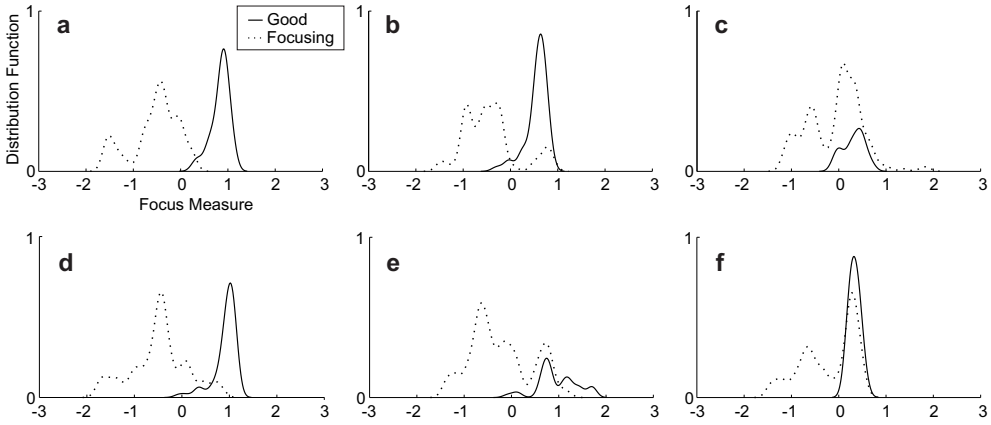

Figure 4.6 Each of the six plots presents two density distributions of the focus measure values. The full line represents the distribution of values when calculated only for the frames labeled as good, and the dotted line represents the frames labeled as focusing. Six plots (a-f) represent six focusing locations of the pilot video sequence (six highest peaks of Fig. 4.5). In all six plots, the greater values of Focus measure correspond to frames in focus and the lower values correspond to frames out of focus.

constraint for each buffer can be limited to the available RAM in the computer used for mosaic stitching. Here, this constraint was set to limit the buffer size to less than 1 GB of RAM. The criteria for selecting buffer borders are mainly:

- no vesicles should be in more than one buffer,
- memory requirement for processing each buffer should be below a predefined constraint.

If the mosaic is observed from the perspective of horizontal lines, the intensity variance in the lines where more vesicles are present, is higher. To satisfy the first constraint, we have to find lines with fewer (preferably no) vesicles and use them for borders. This is done by calculating the average variance of every horizontal line of the mosaic. The lines with the lowest *LineVariance* (Eq. 4.7) are also the lines with few or no vesicles (Fig. 4.8). *LineVariance* for the i^{th} line is calculated as:

$$LineVariance_i = \frac{1}{K \cdot N} \cdot \sum_{k=1}^{K} \sum_{j=1}^{N} [I_k(i,j) - \mu_k(i)]^2, \tag{4.7}$$

where N is the frame width, I is the intensity, i corresponds to the successive line in the mosaic, $\mu_k(i)$ is the mean intensity value of the i^{th} line in frame k that contains this line

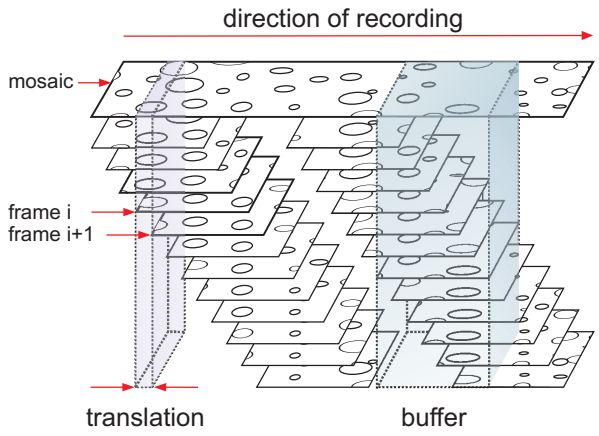

Figure 4.7 Interpretation of frames of the video sequence in our algorithms. Translation, presented in the left shaded cubicle, is the movement between two consecutive frames. The right shaded cubicle represents a single buffer with all corresponding frames of the video sequence. Each buffer contained a full width slice of the mosaic.

in a given buffer, and K is the number of frames that contain the i^{th} line. Separating the frames of the video sequence into manageable buffers was performed as a hierarchical optimization, described below.

The values of *LineVariance*, computed over the mosaic height, was smoothed with a moving average of 20 (selected based on manual inspection) and the local minima were extracted. We used a hierarchical approach to determine which of the local minima of *LineVariance* to use as buffer borders. This was done by sorting the local minima in ascending order and using them to iteratively split bigger buffers of the mosaic into smaller and smaller until every buffer size satisfied the preset memory constraint.

With the frames (source) aligned in the buffers, a blending method to determine the pixel values in the final mosaic (destination) has to be chosen. Some intuitive methods for choosing of destination pixels are the weighted average of the source pixels, mean values, or the temporal median. Temporal median is generally preferable over the weighted average and mean values for its better quality [61]. The major concern with the implementation of the temporal median for a long video sequence is the need for high memory requirement. Fortunately, this issue was solved by using buffers instead of the whole video sequence. To blend all frames of a single buffer into representation of the area, the median intensity value of frames included in a single buffer is calculated (temporal

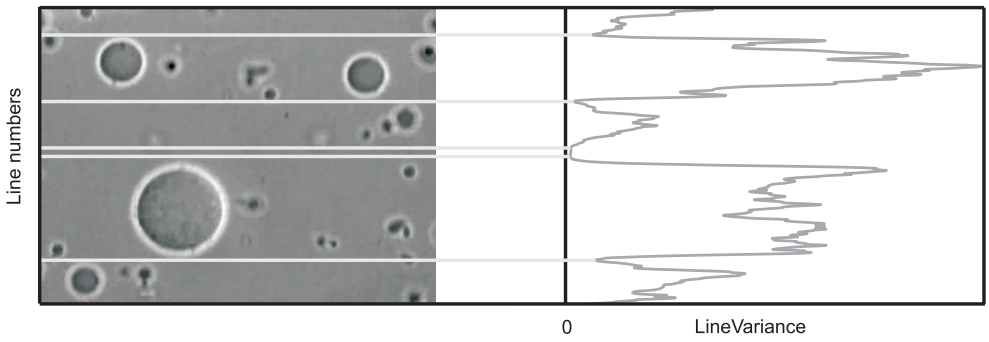

Figure 4.8 Lines without vesicles in the frame on the left correspond to variance minima in the plot of LineVariance (Eq. 4.7) on the right. Potential buffer borders are found in this way, and are marked by horizontal lines leading from the plot on the right to the frame on the left.

median) one at a time. These median images of the buffers (containing destination pixels) are then combined into the mosaic representing the whole area of the recorded video sequence (Fig. 4.7). The transitions between buffer borders are smooth and unnoticeable, because two consecutive buffers always contain (different) parts of the same frames.

However, as we have previously discussed, even though the frames have been aligned using direct registration (normalized cross-correlation), this alignment does not fit all vesicles. As the specimen is dynamic, a vesicle in two overlapping frames could have a different translation than the general translation of frames containing it (computed in § 4.4). Since the median mosaic is generated using only the frame translation alignment, this results in artifacts as shown in Fig. 4.9. The approach used to solve this issue is presented in the following chapter.

4.7 Improving the quality of the mosaic

The mosaic, resulting from steps presented in previous sections, is a temporal median blend of a subset of frames of the original video sequence. In order to extract good representations of objects (mostly vesicles), frames containing motion artifacts or those mostly out of focus were removed prior to blending. At this point, if the recorded vesicles had been static, and there had been no adjustments to the focal plane, no other steps would be necessary. However, this is not true. Even though the vesicles are mostly in the same focal plane, some focusing is still required throughout the recording. In previous sections, frames that were most out of focus were identified by using our Focus measure

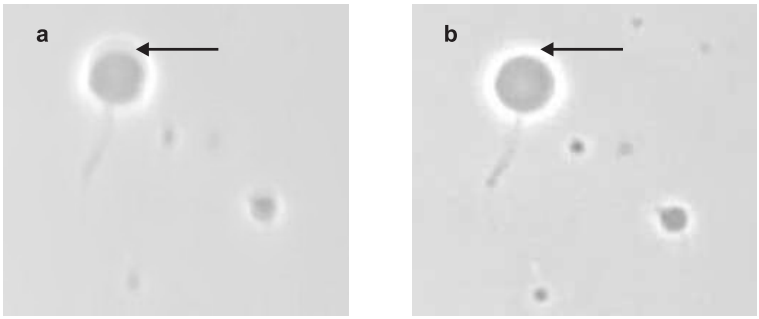

Figure 4.9 Due to local movements of the vesicles in the frames, an artifact appears when using only frame translation information for blending the frames into a mosaic with a temporal median filter. (a) destination pixels of an area in a median blended mosaic, (b) the sharpest frame in the video sequence, representing the same area.

and removed from the subset for temporal median blending. This reduced the size of the dataset for median filtering and enabled somewhat more correct vesicle representation, however, choosing the sharpest representation of every vesicle for the final mosaic would still improve the mosaic and facilitate automated or manual vesicle segmentation.

In order to find the best vesicle representations, these need to be compared between frames containing them. If there had been no movements of individual vesicles, this would be fairly trivial. The direct pixel-to-pixel frame registration (§ 4.4) would also provide the locations of all vesicles in them. Unfortunately, this is not true, the vesicles do express movements and thus need to be locally registered and aligned. At this point, yet another problem is quite obvious. For the local registration of vesicles, the locations of vesicles have to be at least roughly identified. Therefore, some kind of foreground detection is required to separate the foreground objects (mostly vesicles) from the background and allow their local registration. If solved appropriately, this would result in identifying the following properties for every vesicle in our mosaic:

- a mask and a bounding box around it,
- the frame containing vesicle's sharpest representation,
- local misalignment of the vesicle in every frame.

The final step required is to blend the selected vesicle representations onto the initial median mosaic. In this respect, the biggest challenge is to seamlessly insert the vesicle into the mosaic.

4.7.1 Rough foreground detection

In order to assess whether vesicles in the video sequence express any local motion, they first need to be somehow detected and segmented. Due to the low quality of the median mosaic being segmented, it would be an exaggeration to call the steps in this section "vesicle segmentation", so we will stick to the term "foreground detection". However, the intention, of course, is to miss no vesicles at this point. Over-segmentation with false positives is welcome just as long as as few vesicles as possible are missed. The output of this segmentation are the masks and bounding boxes at locations of all objects that "resemble" vesicles.

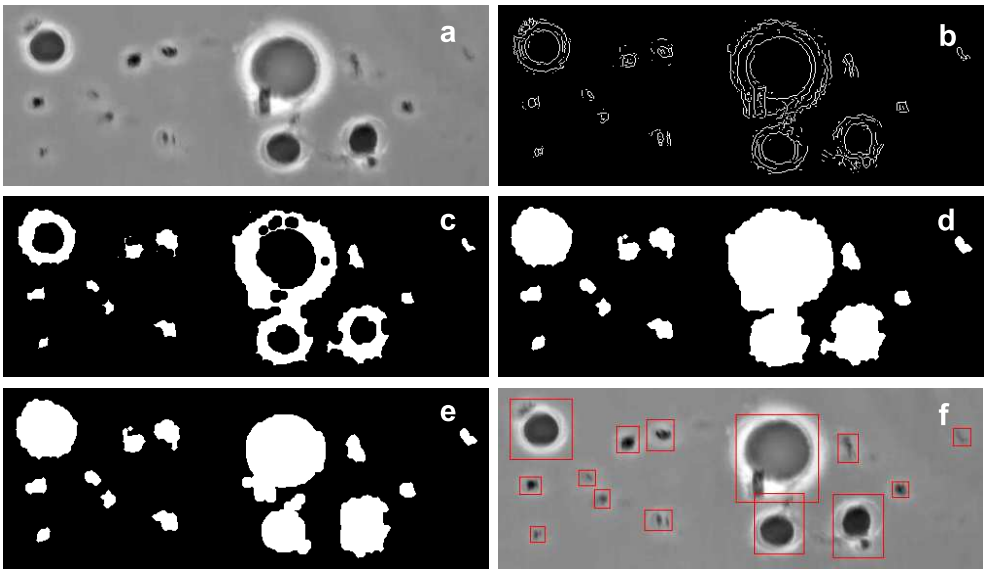

Figure 4.10 Rough foreground detection of the median mosaic, examples of the individual steps. (a) The median mosaic, (b) Sobel edge detection, (c) morphological dilation, followed by an erosion, (d) hole filling, (e) splitting bigger areas into smaller, (f) bounding boxes around every detected object of connected components.

Outputs of steps in our foreground detection are presented with examples in Fig. 4.10. Here, we explain each step in greater detail. All operations are executed upon one buffer at a time. First a Sobel edge detector is employed (Fig. 4.10b) and the extracted edges are used in a morphological close operation (Fig. 4.10c). The Sobel method finds image edges using the Sobel approximation of the derivative. It returns edges at those points where the gradient of the image is maximum. The edge detection preciseness can be set with a threshold, where a large value results in loosely connected or unconnected vesicle

borders. On the contrary, a small threshold returns a very detailed edge estimation which includes not only vesicle edges but also all other fluctuations in the image intensity. In the case of the lipid vesicles, we prefer loose edges and rather employ a morphological closing operation to connect them. The morphological close is a dilation followed by an erosion. When executed on loose edges, it connects them to form connected components, mostly depicting single vesicles and in some cases groups of them. Next, all connected components that have fewer than 150 pixels are removed. The threshold 150 pixels was determined because that equals to a radius of the object of less than 2 μm, which is smaller than the giant unilamellar vesicle being detected. This way all unconnected small objects are removed. Next step is to gather bounding boxes around all remaining objects. This is done by finding all connected components, labeling them, and then calculating bounding boxes that contain them. Most boxes contain single vesicles, but in some cases, more vesicles are attached and cannot be put into separate boxes. All boxes that are longer or wider than 150 pixels (vesicles with radii of more than 18 μm are not common) are then submitted to the same steps as the whole mosaic (Fig. 4.10e). All steps are the same, just the Sobel edge detection threshold is smaller, allowing to separate the vesicles, if there is more than one in the box. The results of each step are depicted in Fig. 4.10.

4.7.2 Local vesicle registration

The goal of the foreground detection steps was to provide bounding boxes containing objects in the foreground. Although not optimal, the precision of the segmentation allows us to detect all vesicles and also some objects that are not vesicles (dust particles, conjugated lipids etc.). As the steps in this section are meant only to improve the mosaic quality, the precision of this foreground detection is sufficient.

With the objects (mostly vesicles) detected, the goal of the next step, local foreground registration, is to align each individual vesicle throughout the third (temporal) dimension in all frames where it is present. By visually inspecting individual vesicles we concluded that the movements consist mainly of translations and rotations. For alignment purposes, only translation is important, as vesicle from only one of the frames will be chosen for the final mosaic, and its rotation is not interesting for our analysis. Just as with global registration of frames (§ 4.4), registering vesicles in *subsequent frames* was first tested. It turned out that the vesicle motion was not apparent enough to be detected this way.

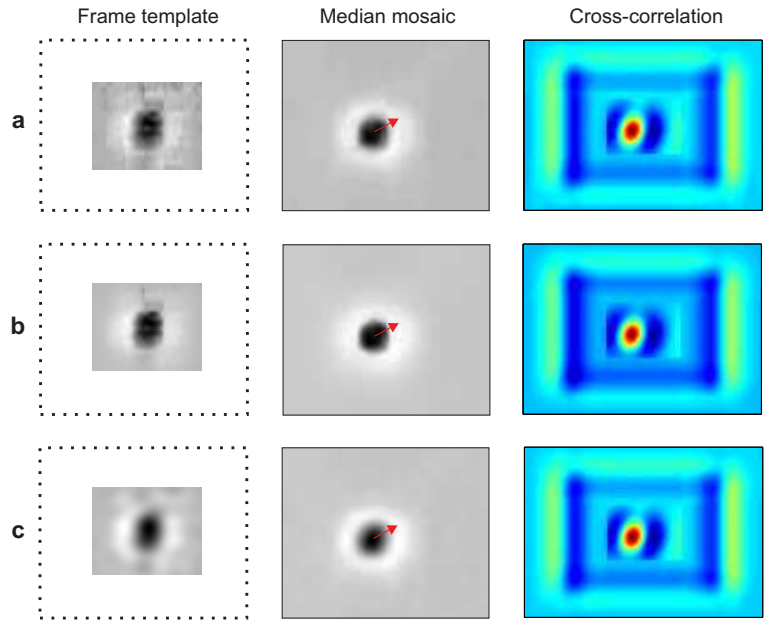

Figure 4.11 Local registration of differently filtered vesicles. Horizontally (a) gray intensity of the vesicle in the mosaic, (b) bilateral filtered gray intensity, (c) low pass filtered gray intensity. The three columns are a template taken from one of the source frames (left), the median mosaic (center) values of the normalized cross-correlation of the template over median mosaic. The arrows in the middle column denote the translation of the template image in relation to the mosaic.

Instead, we decided to register vesicles in each frame to the median mosaic instead. Once again normalized cross-correlation was employed [79]. As we soon discovered, this algorithm only gives meaningful results if the *template* image being registered is smaller than the target image. Therefore, a template region with the vesicle in every frame was registered to a region in the median mosaic 9 times the size of the template. We tested registering differently filtered images: gray intensity, low pass filtered gray intensity and bilateral filtered [73] gray intensity (Fig. 4.11).

This way, we were able to detect local translations of single vesicles in respect to the median mosaic. The differences in translations acquired by registering differently filtered images were minimal (a plot depicting the translation throughout the frames of a single vesicle is given in Fig. 4.12). We decided to use the registration given by low pass filtered images for the following steps requiring local vesicle registration.

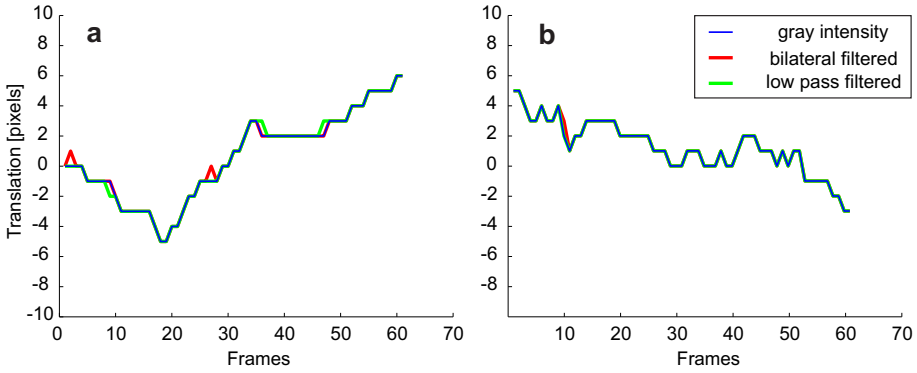

Figure 4.12 Local movements in pixels of a single vesicle through all frames that contain it. (a) Vertical shifts. (b) Horizontal shifts. The difference between registration of differently filtered images is rarely present and always within 1 pixel of the translation on gray intensity image.

4.7.3 Finding the sharpest vesicle representation

Having acquired the masks of objects in the foreground and registered them in every frame, the next step is to decide which frame contains their sharpest representation and should be chosen for the final mosaic. With visual observation this step is trivial, as a human can recognize when a vesicle is most in focus with only a little practice. A computer, on the other side, needs to inspect every frame and compare the pixels or regions in different frames in order to choose the *best* for the final mosaic. A similar problem was also discussed in the section on selecting best frames (§ 4.5).

Two quite distinct approaches were tested, one based on taking individual pixels from frames, and the other on taking regions instead. Either way, most steps are the same in both cases. The regions or pixels need to be assigned a value so they can be compared to each other for sharpness. Then the best pixels/regions are selected and blended onto the mosaic. A similar problem is encountered also in a wide area of applications. Just to name a few: segmentation of objects in images with low depth of field [80–83], automated extraction of alpha-matte for video sequences [84], combining multiple images acquired focused at different depths into one sharp image [85] or a 3-dimensional structure model of the recorded object [86] also called *shape from focus* [87]. In this context, various approaches for estimating the depth, focus, or sharpness of a pixel/region are proposed. Frequently used are techniques that rely on local variance estimates [81, 84]. Another approach is to iteratively blur an image and subtract it

from the original. This way, the sharpest regions will be the last to disappear from the difference image and can thus be segmented in the original [88]. Focus regions can also be estimated using spatial derivatives. A simple unsupervised approach is presented by Tsai and Wang [80] where image edges are first evaluated using a Sobel edge detector, linked together by morphological operations and then higher moments are estimated at all edges to determine whether it belongs to an object in focus. For comparing sharpness on a pixel level, Boissenin et al. [86] propose a pixel based sharpness measure:

$$\begin{aligned}\text{Buff}_s(i,j,z) := \quad & (\text{Buff}(i+1,j,z) - \text{Buff}(i-1,j,z))^2 + \\ & (\text{Buff}(i,j+1,z) - \text{Buff}(i,j-1,z))^2,\end{aligned} \tag{4.8}$$

where $\text{Buff} : \mathbb{N}^3 \mapsto \mathbb{R}$ is a 3-dimensional buffer containing the aligned frames, i and j denote pixel coordinates in the Buff, and z is the frame number in the Buff. After calculating sharpness of every pixel in the buffer, the source frame for every pixel is found by maximizing:

$$I_{sharp}(i,j) := \arg\max_z(\text{Buff}_s(i,j,z)). \tag{4.9}$$

The pixel sharpness measure was tested on a set of images Fig. 4.13. It is used to find sharp regions in twelve images of the same keyboard with varying shallow depth of field. These sharpest regions are then fused into a single sharp image, similar to the image taken with a large depth of field. Even though the resulting keyboard image is sharp throughout the depth, there is a spatial discrepancy between the original images due to the lens magnification effect [89, 90]. These result in edge misalignments, visible when the upper two images are compared or when the fused image is observed. This discrepancy can be evaluated and aligned by applying a block based matching measure [88].

Applied to the vesicle mosaic, the pixel-based approach did not yield visually satisfying results (see Fig. 4.16). Instead, we used the region based measure, where multiple features are computed for every vesicle bounding box in every frame. These measures are the Brenner gradient (Eq. 4.2), Variance, Entropy (Eq. 4.6), Contrast (Eq. 4.3), and the AFAF (Eq. 4.5). The vesicle representation at the maximum and minimum values of each measure were compared and interestingly, four out of the five measures yield results of similar quality. The maximum of measures: Brenner, Variance, Contrast, and the min-

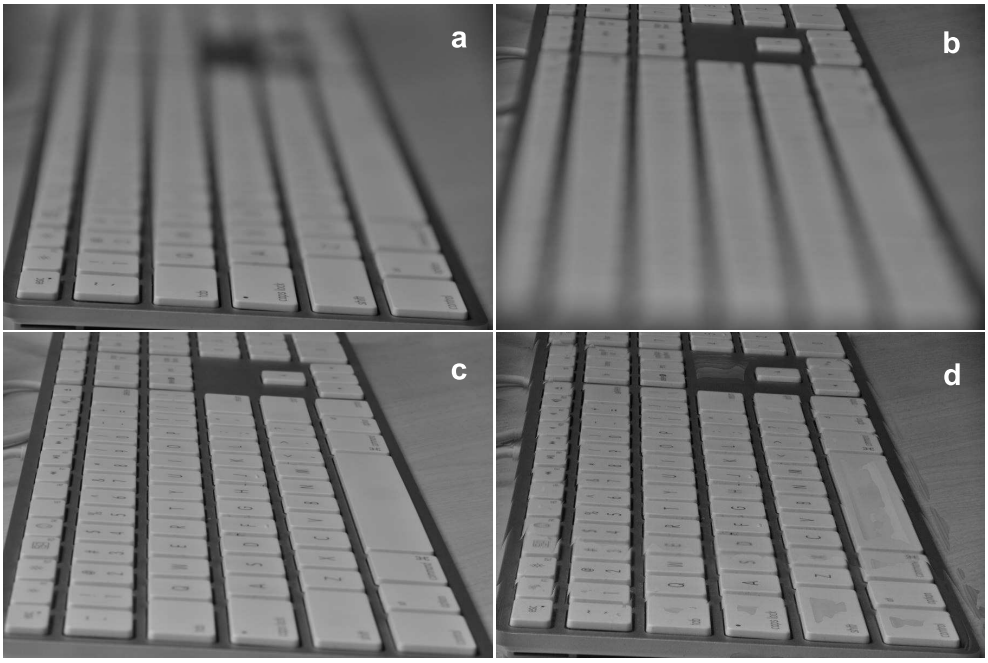

Figure 4.13 A series of 12 photos were taken (a and b are two of them) representing a keyboard with a different part in focus. Photos were taken from a fixed point with a Nikon D90 DSLR camera and 18-200 mm Nikkor lens. The aperture was set to $f = 5.6$. The sharpness measure was calculated for every pixel of every photo, and a reconstruction of the sharpest areas was created (d). The same keyboard was also photographed with a larger depth of field at aperture $f = 22$ and is presented in (c).

imum of the AFAF measure returned equally sharp vesicle representations. This makes all of these features qualify as good vesicle sharpness assessment measures. Only the Entropy measure returned indistinct vesicles at both extremities. For one vesicle, plots with feature values at all frames and the vesicle representations at extremities are given in Fig. 4.14. We also compare the Brenner measure of vesicles in two buffers Fig. 4.15. Each line of a figure corresponds to the occurrences of one vesicle in the frames (horizontal axis). The color is its Brenner measure value (the hotter the color, the higher is the vesicle sharpness). It can be noted that in most cases, the best representation of multiple vesicles is in the same frame or at least in a narrow neighborhood of frames.

Choosing every pixel individually from an independent frame can produce a very noisy mosaic, and blending all sampling pixels can result in a very smooth mosaic with a loss of details. Both approaches are prone to the ghosting effects [48]. In this respect, a choice of a region based approach is preferable as all pixels belonging to a vesicle are

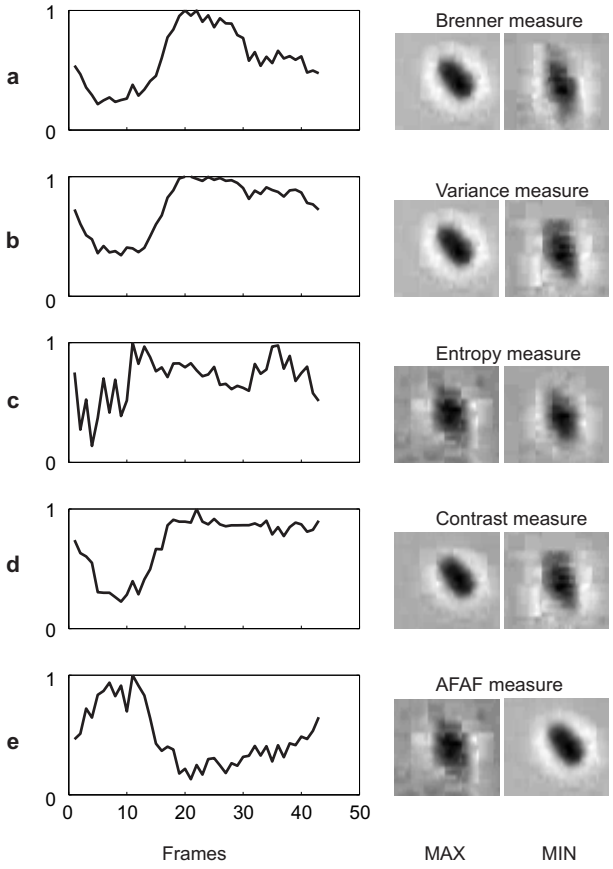

Figure 4.14 Five different region based sharpness measures computed for a single vesicle followed over 43 frames containing it. The left column are plots of the measures' values at every frame. On the right the vesicle regions from two frames are presented, one at maximal value of the corresponding measure and the other at minimal value. In four cases (Brenner, Variance, Contrast and AFAF measures) one of the extremities gives a sharp representation of the vesicle, and the other a very vague one. In the case of Entropy measure, vesicles in both images are indistinct.

taken from the same frame and thus spatially consistent. On the other side, this also comes with a downside. As the pixels are from the same frame, when directly copied on top of the median vesicles, the area inside the bounding box does not look uniform with the rest of the mosaic. The transitions between regions usually produce an intensity inconsistence demonstrated as an edge. This can be observed in figure Fig. 4.16, where four different approaches to blending a mosaic are presented. The median mosaic, created with temporal median blending of all frames, the sharp mosaic, where every pixel is taken from the frame chosen by Eq. 4.9 and the mosaic, where for every vesicle, the sharpest

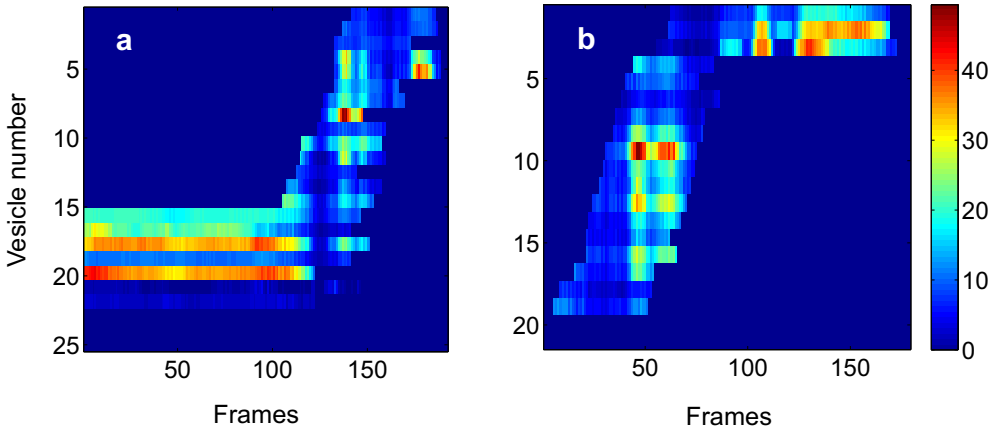

Figure 4.15 How the Brenner measure of different vesicles changes through frames. The figures (a) and (b) represent the vesicles (each line of the vertical axis is one vesicle) Brenner measure (colorbar on the right) in each frame (horizontal axis) where it occurs. The dark blue color (value 0) is in the frames where the vesicle is not present.

representation is chosen by the Brenner measure Eq. 4.2. The problem of blending a part of one image into another can be successfully approached with gradient domain fusion [48, 63] and is described in the following chapter.

4.7.4 Vesicle gradient domain fusion

After the sharpest vesicle representation is found, it needs to be seamlessly blended onto the stitched median mosaic. This is best performed by employing seamless image blending using Poisson equation solving [64]. Such approaches are called gradient-domain processing since they use the gradient data instead of intensity values directly in order to achieve the seamless blend. For example, this technique found applications in image blending, tone mapping, non-photo realistic rendering etc.

The simplest method would be to just copy the intensity values of the source image (the sharpest vesicle) directly onto the target image (mosaic). Unfortunately, this usually creates a very noticeable seam, even if the background intensities are well matched. The goal of more sophisticated approaches is to get rid of these seams without doing too much damage to the source region being copied. We can form the problem as finding values of the target pixels that maximally preserve the gradient of the source image without changing any of the pixels bordering the region in the target image. The insight is that people often care more about gradient of an image than the overall intensity. Thus, using

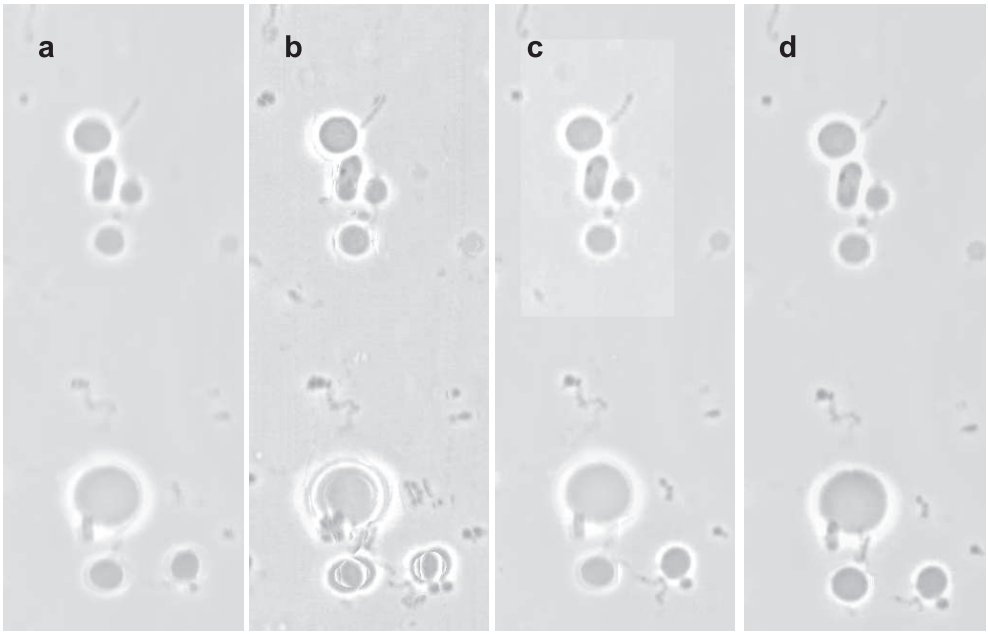

Figure 4.16 Results of three approaches to mosaic blending. (a) The median mosaic, created with temporal median blending of all frames, (b) the sharp mosaic, where every pixel is taken from the frame chosen by Eq. 4.9, (c) the sharpest vesicle representation is chosen by the Brenner measure and the bounding box is copied directly into the median mosaic. (d) The sharpest bounding box is selected as in (c) but blended in the mosaic by Poisson blending.

the target image intensities just outside the transfer region, we try interpolating with the source image gradient from inside the copying region. Perez et al. [64] call this guided interpolation where boundary conditions are set in adjacent regions and the transition is interpolated with Poisson blending [64]. The discrete interpretation of this interpolation boils down to the following algorithm. For each pixel under the mask, its value satisfies the equation for all $p \in \Omega$:

$$|N_p|\, f_p - \sum_{q \in N_p \cap \Omega} f_q = \sum_{q \in N_p \cap \partial\Omega} f_q^* + \sum_{q \in N_p} v_{pq}, \tag{4.10}$$

for all neighbors $\langle p, q \rangle$ in a 4-connected neighborhood, $v_{pq} = g_p - g_q$, where the notation is as follows:

$$\begin{aligned}
f^* &= \text{source image,} \\
g &= \text{target image,} \\
p &= \text{pixel,} \\
\Omega &= \text{pixels under the mask,} \\
\partial\Omega &= \text{pixels which have at least one neighbor under the mask,} \\
N_p &= \text{neighborhood of pixel } p, \\
|N_p| &= \text{number of neighbors of pixel } p, \\
f_p &= \text{new value of pixel } p, \\
f_p^* &= \text{value of pixel } p \text{ in the source image,} \\
v_{pq} &= \text{gradient of the pixel intensity to a neighbor in the source image.}
\end{aligned}$$

From the equation above, we can write an equation for the new value of each of the pixels under the mask. Each equation contains data on the values of all the neighboring pixels in the target image and the gradient from the source image. Only a subset of the values of neighboring pixels are known (those from the border of the mask), and the values of the pixels under the mask depend on each other for their final value. To solve these equations, they have to be computed simultaneously, which can be done by solving the linear system formed as an equation $Ax = b$. The relations between the pixels are presented in lines of the matrix A. The vector x contains all pixels in the final image and the vector b is the guiding gradient plus the sum of all non-masked neighbor pixels in the target image. Solving the equation for x gives the final image where the vesicles blend smoothly into the mosaic (Fig. 4.16d).

When all bounding boxes containing the vesicles are blended into the median mosaic, the mosaic stitching is concluded. A part of a stitched mosaic is presented in Fig. 4.17 where an area is marked that represents the size of a single frame. The resulting mosaic is the input for the vesicle segmentation algorithm, which is the topic of the next chapter.

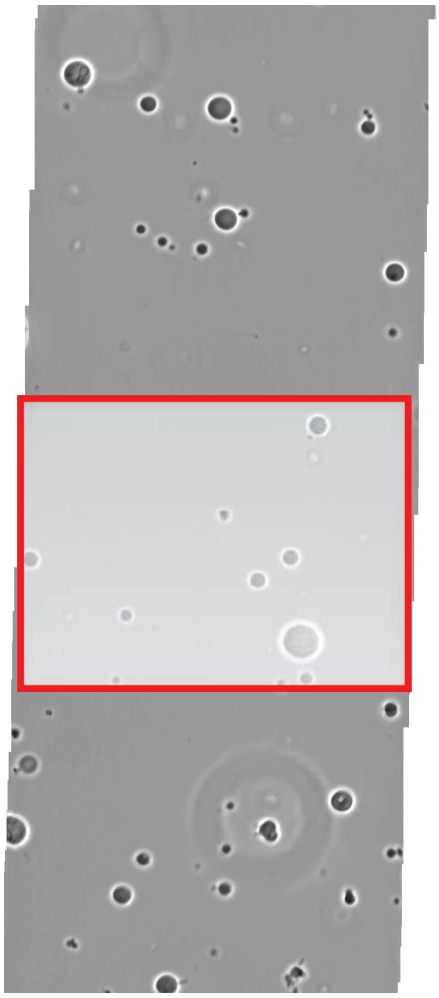

Figure 4.17 Part of a mosaic stitched from a microscopy video sequence of a single track. The whole track is approximately 33 times the height of the presented sample. The rectangle in the centre represents a single field of view that can be observed at 400x magnification and is also the size of a single frame.

5 Lipid vesicle population segmentation

5.1 Properties of lipid vesicle images

The video sequences of lipid vesicle populations stitched into mosaics were recorded with the use of phase contrast optical microscopy. This is the most common microscopy technique employed in research on lipid vesicles, mostly because they are well visible due to their size and properties [19–25]. The most important property for their segmentation is that the vesicle interior appears darker from the surrounding medium in the micrographs, which makes it distinguishable from the background. The intact membrane is impermeable to sugar molecules, and the composition inside the vesicles (primarily saccharose) differs from the saccharose/glucose composition outside. This difference in the content density results in a different refractive index (the tendency of the materials to bend light). In phase-contrast microscopy, a white halo occurs around the vesicle, separating the darker inside from the brighter background. The halo effect is exploited not only with lipid vesicles but for cell segmentation in general [91, 92].

Observed at 400x magnification with a phase contrast light microscope, a giant unilamellar lipid vesicle can be recognized as a dark spherical region, surrounded by a bright

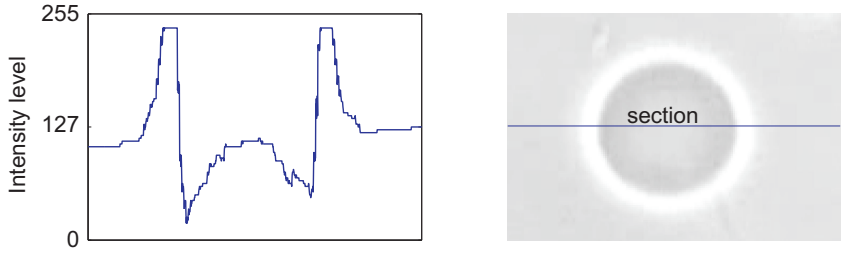

Figure 5.1 A giant lipid vesicle extracted from a micrograph (right) and an intensity grayscale value plot (left) of a cross section of the same vesicle, marked with the horizontal line in the image of the vesicle. On the vertical axis, 0 is the black intensity, and 255 is the white.

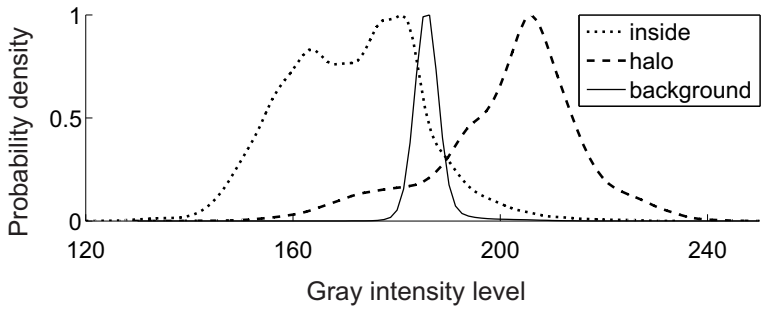

Figure 5.2 The probability density functions of grayscale intensities for all three regions - vesicle, halo, and the background.

halo (Figure 5.1). When grayscale intensities in the different regions of the vesicle and its surroundings are compared, the following differences are observed. The darkest regions of the micrographs are the vesicle insides, and the brightest regions are the vesicle halos (Figure 5.2). Both intensity distributions are wider than the intensity distribution of the micrograph background. However, in order to use straightforward approaches (e.g. thresholding) to segment the vesicles, the intensity distributions of the areas should not overlap. In this case, it is not so, and more advanced segmentation approaches are necessary.

In published research, several methods for lipid vesicle segmentation have been proposed. A standard approach is to exploit the high grayscale intensity regions of the halo to extract its contour by using an edge detector [24]. Manually selected points within the vesicles were also used as origins of a polar coordinate system from which a series of radial rays pointing towards the lipid membrane are generated. The profiles of image intensities, projected along the rays, contain distinctive patterns that result from the

halo effect [27, 29, 93]. These can be extracted by using e.g. intensity derivatives. Both approaches are adequate for segmenting single vesicles from micrographs, but fail when multiple vesicles are present. For such cases, we previously proposed a two tier detection system. In the first tier, thresholding and morphological operations are applied to acquire regions where the vesicles are present. In the second tier, a fine vesicle border detection is applied using the determinant of the Hessian of intensity values at every pixel [2]. The second derivative test states that the eigenvalues of the Hessian are negative around local maximum. Both eigenvalues will be negative and their product is positive inside a region that is defined by the inflection curve of the intensity function. On the inflection curve, one of the eigenvalues will change the sign making the product negative. This can be detected by calculating the determinant of the Hessian which shares the sign with the product of eigenvalues of the Hessian. Although this method works well in some cases, it fails where intensity of the vesicle inside varies. In such situations, the algorithm splits a single vesicle into two, each with a more homogeneous intensity. Additionally, we tested some other approaches that had previously been used for cell segmentation in optical microscopy or for segmenting objects with shapes similar to lipid vesicles. Apart from simple (region growing, template matching) that did not yield satisfactory results, we also tried some methods that depend on shapes to find and segment the objects. A generalized Hough transform, for example, is commonly used to detect shapes which can be parametrically described as lines, circles, or ellipses, the latter being especially useful for segmenting cell-like shapes [94]. One such, an adapted Hough transform algorithm [95] was tested on micrographs. This way, a majority of spherical vesicles are detected correctly, since the potential heterogeneity of the vesicle inside intensity does not affect the segmentation. However, some other issues arise. The Hough transform is based on parametrization of the shapes being sought. The image space (its gradient or edge values) is transformed into the parameter space, where the parameters describing a certain shape, orientation, location, are accumulated if such a shape appears in the image space. The peaks in the parameter space hold information on the parameters describing the shape in the image space. If lines, circles or ellipses are describable with two to five parameters (the fifth being the ellipse rotation angle), the non-spherical vesicles are not. The multitude of shapes and potential contours of these vesicles in micrographs require many more parameters (for a parametrization[1] of potential vesicle contours see [33]). As

[1] Description and parametrization of vesicle shapes in lipid vesicle research is most often presented in

the complexity of shape parametrization for the Hough transform increases, so does the computational requirements. This increases the dimensionality of the problem and causes the usability of such vesicle segmentation to become useless due to its time inefficiency. Since the vesicles comprise of so many different shapes, we rather focused on another property they all (spherical and non-spherical) have in common. The most direct way to describe how the vesicles differ from the micrograph background to a non-expert would be to distinguish the gray intensity distributions of the vesicle inside and the halo. These properties of neighborhood information and intensity distribution are also the basis for a model, that is often applied to image segmentation: the Markov random field model.

5.2 Markov random field segmentation

The Markov random field model (MRF) is a frequently applied model in image interpretation processes [96], since classification of a particular pixel is also based on the classification of its neighboring pixels rather than on the pixel intensity alone. For example, to segment the image into two classes, foreground and background, an MRF model for spatial interaction between pixels will cause the pixels with neighbors classified as foreground to be classified as foreground with greater probability. This exploitation of a priori models of spatial interaction between image pixels can compensate for deficiencies in observed information, and is also applicable in the case of vesicle segmentation from micrographs.

5.2.1 Introduction

In general, image segmentation can be described as assignment of class labels to individual pixels of the image, the goal being to divide the image into distinct segments [96–99]. Pixels of each segment share some kind of similarity. This similarity could be proximity of pixels, intensity levels, however, it should be quantified and incorporated into a model that assigns each pixel to a segment.

The MRF segmentation model used in this dissertation can be defined as follows [98]. First, N pixels of the image being segmented are $\mathcal{P} = \{p_1, p_2, ..., p_N\}$ and the gray intensities of image pixels are an observation $\mathcal{F} = \{f_1, f_2, ..., f_N\}$. Given T distinct class labels $\Psi = \{1, 2, ..., T\}$, a valid segmentation of the image is a set of class labels $\phi = \{\phi_1, \phi_2, ..., \phi_N\}$, where each image pixel is assigned one class label. Using the

a Phase diagram.

Bayesian approach [100], we assume a set of observed (Y) and a set of hidden (X) random variables, in our case $\mathcal{F} \in Y$ and $\phi \in X$.

Now we can formulate finding a segmentation of the image as Bayesian labeling [96] so that the probability distribution $P(\mathcal{F}|\phi)$ is the imaging model and $P(\phi)$ is a prior probability distribution. The Bayes theorem gives the posterior distribution:

$$P(\phi|\mathcal{F}) \propto P(\mathcal{F}|\phi)P(\phi). \tag{5.1}$$

We assume that the observation $\mathcal{F}$ is a noisy version of the underlying segmentation, which we want to identify. The aim is to find a segmentation ϕ^*, maximizing the posterior probability $P(\phi|\mathcal{F})$, therefore the maximum a posteriori (MAP) estimate:

$$\phi^* = \arg\max_{\phi \in \Phi} P(\mathcal{F}|\phi)P(\phi)\,, \tag{5.2}$$

where Φ is the set of all possible segmentations of the image. The segmentation ϕ is modeled as a Markov random field (MRF).

5.2.2 Prior and imaging model

Finding the optimal segmentation ϕ^* first requires defining the prior ($P(\mathcal{F}|\phi)$) and the imaging model ($P(\phi)$). According to the Hammersley-Clifford theorem [100], $P(\phi)$ follows the Gibbs distribution:

$$P(\phi) = \frac{1}{Z}\exp(-U(\phi))\,, \tag{5.3}$$

where $Z = \sum_{\phi \in \Phi} \exp(-U(\phi))$ is the normalizing constant. $U(\phi)$ is called an energy function, which is defined as:

$$U(\phi) = \sum_{C \in \mathcal{C}} V_C(\phi_C)\,. \tag{5.4}$$

Here, V_C is the clique potential of clique $C \in \mathcal{C}$ with the label configuration ϕ_C. A clique is a pair of pixels in a spatial neighborhood. Our MRF is defined over an 8-connected two dimensional neighborhood, the 2^{nd}-order cliques being defined as shown in Fig. 5.3. The V_C clique potential is calculated over all cliques in the image, $\mathcal{C}$ being the set of all 2^{nd}-order cliques, which correspond to pairs of neighboring pixels. The nature of the

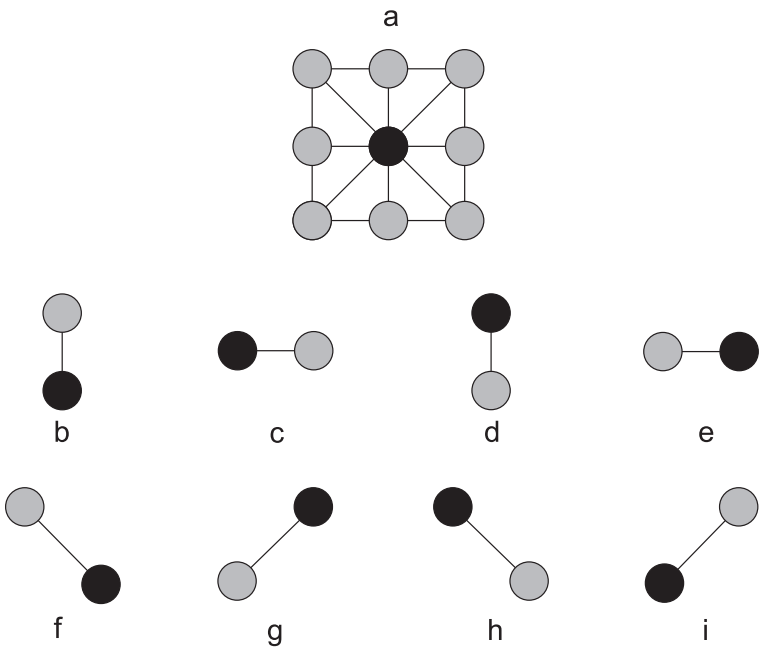

Figure 5.3 (a) The 8-connected neighborhood system of our MRF. (b-i) are the 2^{nd} order cliques of the above defined neighborhood.

segmentation problem is that two neighboring pixels are more likely to belong to the same segment. In MRF, this is expressed by the potential, which favors same classes for neighboring pixels $\{p_i, p_j\} \in C$:

$$V_C = \theta(\phi_{p_i}, \phi_{p_j}) = \begin{cases} +1 & \text{if } \phi_{p_i} \neq \phi_{p_j}, \\ -1 & \text{if } \phi_{p_i} = \phi_{p_j}. \end{cases} \tag{5.5}$$

The more homogeneous the segmentation, the higher its probability. Using Eq. 5.3, Eq. 5.4, and Eq. 5.5, we get the complete prior:

$$P(\phi) = \frac{1}{Z} \exp\left(- \sum_{\{p_i, p_j\} \in \mathcal{C}} \theta(\phi_{p_i}, \phi_{p_j}) \right). \tag{5.6}$$

Each pixel has a certain probability of belonging to a class $\psi \in \Psi$ due to the pixel's intensity value in the observation $\mathcal{F}$. The probability distributions of intensities for each class are extracted from multiple manually segmented images of vesicles, where three classes are defined: vesicle, halo, and background (Fig. 5.2). These distributions

are used to calculate the imaging model $P(\mathcal{F}|\phi)$. We assume that our features (gray intensities) f for a given class $\psi \in \Psi$ are normally distributed around the mean value μ_ψ:

$$N(\mu_\psi, \sigma_\psi) = \frac{1}{\sqrt{2\pi\sigma_\psi^2}} \exp\left(-\frac{1}{2}\left(\frac{f-\mu_\psi}{\sigma_\psi}\right)^2\right). \tag{5.7}$$

Therefore, for each class ψ, the μ_ψ and σ_ψ are extracted. The features are assumed to be independent [98], so the probability of the imaging model is the product:

$$\begin{aligned} P(\mathcal{F}|\phi) &= \prod_{p\in\mathcal{P}} P(f_p|\phi_p) \\ &= \prod_{p\in\mathcal{P}} \frac{1}{\sqrt{2\pi\sigma_{\phi_p}^2}} \exp\left(-\frac{1}{2}\left(\frac{f_p-\mu_{\phi_p}}{\sigma_{\phi_p}}\right)^2\right). \end{aligned} \tag{5.8}$$

Similarly to the doubleton potential (Eq. 5.5) the singleton potential can also be defined. The singleton potential of each pixel p corresponds to the likeliness of its intensity to belong to a certain class. This can be specified by the logarhithm of Eq. 5.7 which leads to the following expression:

$$V_p(\phi_p, f_p) = \ln\sqrt{2\pi\sigma_{\phi_p}^2} + \frac{1}{2}\left(\frac{f_p-\mu_{\phi_p}}{\sigma_{\phi_p}}\right)^2. \tag{5.9}$$

5.2.3 Posterior probability

To calculate the posterior probability $P(\phi|\mathcal{F})$, we have to take into account two components. The singleton and doubleton potentials. The first define the pixels' class labels based on the probability distributions of intensity of each class label (imaging model, $P(\mathcal{F}|\phi)$). The latter estimate the contribution of the clique potentials (the prior $P(\phi)$). Combining the singleton and doubleton potentials gives the following energy function:

$$U(\phi, \mathcal{F}) = \sum_{p\in\mathcal{P}} V_p(\phi_p, f_p) + \beta \sum_{\{p_i,p_j\}\in\mathcal{C}} \theta(\phi_{p_i}, \phi_{p_j}), \tag{5.10}$$

where β is a weight regulating the relevance of the prior, $\beta > 0$. As β increases, the resulting regions become more homogeneous because the same neighboring classes are rewarded. Combining Eq. 5.1 and Eq. 5.3 gives a connection between the energy function and the posterior probability:

$$\begin{aligned} \exp(-U(\phi, \mathcal{F})) &\propto P(\mathcal{F}|\phi)P(\phi) \\ U(\phi, \mathcal{F}) &\propto -(\ln(P(\mathcal{F}|\phi)) + \ln(P(\phi)). \end{aligned} \tag{5.11}$$

Plugging in $P(\mathcal{F}|\phi)$ (Eq. 5.8), $P(\phi)$ (Eq. 5.6), and dropping the normalizing constant Z leads to the complete energy function $U(\phi, \mathcal{F})$:

$$U(\phi, \mathcal{F}) = \sum_{p \in \mathcal{P}} \left(\ln \sqrt{2\pi\sigma_{\phi_p}^2} + \frac{1}{2} \left(\frac{f_p - \mu_{\phi_p}}{\sigma_{\phi_p}} \right)^2 \right) + \beta \sum_{\{p_i, p_j\} \in \mathcal{C}} \theta(\phi_{p_i}, \phi_{p_j}) \,. \tag{5.12}$$

This way, the maximum a posteriori estimation (Eq. 5.2) is equivalent to the following energy minimization:

$$\phi^* = \arg\min_{\phi \in \Phi} U(\phi, \mathcal{F}) \,. \tag{5.13}$$

The segmentation problem thus becomes the optimization of the function $U(\phi, \mathcal{F})$. Since it is difficult to maximize the joint probability of an MRF, Besag [101] proposed a deterministic algorithm called iterated conditional modes (ICM) which maximizes local conditional probabilities sequentially. The ICM algorithm uses the "greedy" strategy in the iterative local maximization.

5.3 Markov random field adjustment for vesicle segmentation

To segment the vesicles, we divide the micrograph pixels into three regions: the vesicle, the halo, and the background, thus $T = 3$. One can observe all three segmented regions in Figure 5.4c. Figure 5.4a shows a part of the micrograph where multiple vesicles are present. As shown in Figure 5.4b, the MRF segmentation model presented in previous section does not succeed in segmenting the vesicle. The halo and background in the region are segmented correctly, however the vesicle inside is classified as background in some cases.

Here we present a correction mechanism for the image segmentation model, allowing a correct segmentation of the vesicles. This is accomplished by adding an additional potential function (PF) to the function $U(\phi, \mathcal{F})$. The PF is in the following form:

$$PF(\phi, \mathcal{F}) = -\gamma \delta(\phi_p, 2) \delta(\phi_p^-, 1) \rho \left(\sum_{\{p,r\} \in \mathcal{C}} \phi_r - \Delta \right) , \tag{5.14}$$

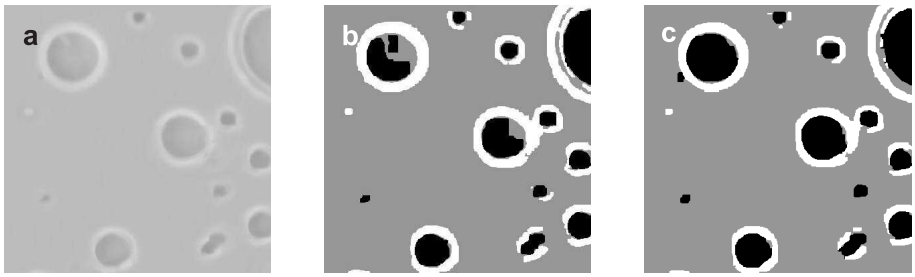

Figure 5.4 (a) Original image, (b) segmented image without correction (MRF), and (c) segmented image with correction (MRF2).

where

$$\delta(a,b) = \begin{cases} 1 & \text{if } a = b \\ 0 & \text{otherwise} \end{cases} \tag{5.15}$$

and

$$\rho(a) = \begin{cases} a & \text{if } a \geq 0 \\ 0 & \text{otherwise} \end{cases} \tag{5.16}$$

The term ϕ_p^- is the value of ϕ_p in previous iteration. Δ is a predefined threshold. The complete function to optimize is now $U_2 = U + PF$.

The explanation of the function PF is the following. One would like the background pixels (label 1) which are surrounded by the pixels classified as vesicle (label 2) and the halo pixels (label 3) to be more likely to turn into pixels of the vesicle (label 2). This is the situation where the classification error of the original MRF is the highest (Figure 5.4b) as the vesicle pixels are falsely classified as the background pixels. Let the label 1 mark the background, 2 vesicle, and 3 halo (Table 5.1).

Table 5.1 Labels for background, vesicle, and halo.

label	element	color in segmented images
1	background	gray
2	vesicle	black
3	halo	white

The function $\delta(\phi_p^-, 1)$ reflects the fact that the pixel p was previously marked as background (label 1), and $\delta(\phi_p, 2)$ reflects the fact that the pixel p is now a candidate for

the vesicle pixel (label 2). When neighboring pixels of a background pixel have labels 2 and 3, the sum of the label values is high, and when it reaches the predefined threshold Δ, the background pixel turns to a vesicle pixel. The interior of the vesicle is filled in this way completely. The parameter γ is the weighting parameter controlling the importance of the term. The MRF algorithm with this correction mechanism is denoted as MRF2 in our experiments.

Directly applying the MRF segmentation to the whole mosaics proved unsuccessful as each iteration would require hours of processing. Instead, we once again employed the rough foreground detection step previously presented in § 4.7.1. At that point, this rough foreground detection was required in order to locally register vesicles and apply sharpness estimation to find the sharpest vesicle representations in the frames that contained it. Here, the foreground detection was used to acquire bounding boxes containing objects in individual buffers. This foreground detection relies on the edge detection (and consequently the gradient of the image), which causes all objects that step out of the background to be detected as foreground. These areas of interest are passed to the MRF2 algorithm as bounding boxes. This way, the computationally intensive MRF algorithm is applied only to individual bounding boxes at a time, which significantly reduces the time required for each iteration.

The MRF requires mean values and variance of grayscale intensity for each of the classes, in this case the halo, the vesicle, and the background. We extract those from a manually segmented micrograph with multiple vesicles. Because the buffers in various mosaics could express somewhat different lighting conditions, we apply zero mean normalization to the grayscale intensity distribution for the segmented micrograph and each buffer entering the segmentation. Besides accuracy of the MRF segmentation, this step also improves accuracy of the foreground detection output.

All manual segmentation is performed by a custom developed plug-in for the open source image processing software ImageJ [44]. The Matlab used was Matlab 2009b, ImageJ plug-in "Shape Segmenter" was developed in Java with the use of the environment Eclipse. A screenshot is presented in Fig. 5.5.

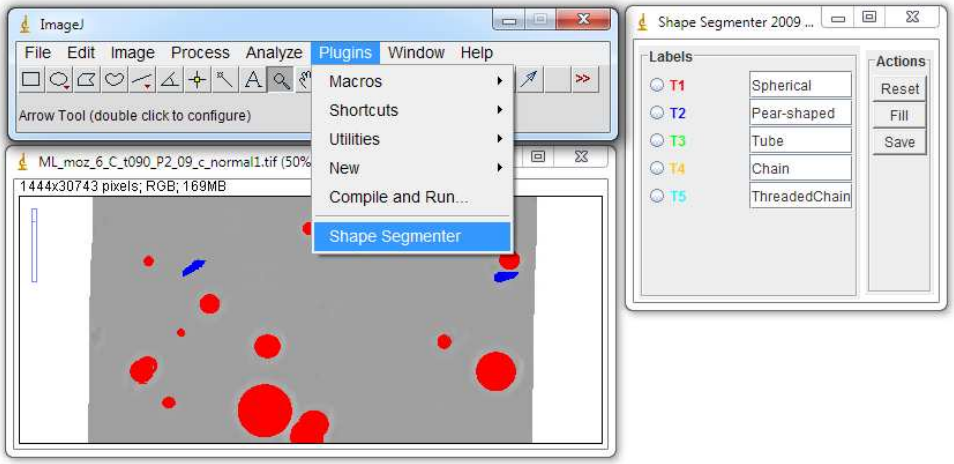

Figure 5.5 Screenshot of the ShapeSegmenter plug-in, developed for manual segmentation of vesicles.

6 Results and discussion

6.1 Organization of results

Due to the horizontal extent of the topics in this thesis, the results and discussion material is combined in the sections according to subject matter. We discuss the results gained with the presented methodology when applied to two different nanoparticle—vesicles experiments and one with synthesized images containing vesicles. The connections between different steps of our methodology and experiments are presented in Tab. 6.1.

Experiment	Data type	Nano	Mosaicing	Manual seg.	MRF2 seg.
Synthesized images	images	NO	NO	✓	✓
C_{60} experiment	micrographs	✓	NO	✓	NO
$CoFe_2O_4$ experiment	videos	✓	✓	✓	✓

Table 6.1 The results chapter contains three sections where the proposed methodology is evaluated. The table connects a certain experiment with the steps of our methodology that are tested on that data. The abbreviations used are "seg." - segmentation, "nano" – including nanoparticles.

6.2 Mosaic validation

There is no ground truth for direct comparison and validation of the presented mosaic stitching method. The only way to check the resulting mosaic is to compare the vesicles in it to the vesicles in the original video sequence. Most vesicles were found in both, the video and the corresponding mosaic. Vesicles detected only in the video are very small and never appear sharp in the video.

When comparing the median mosaic to the sharp mosaic, the sharpest vesicle representations from the video frames are captured in the latter with few exceptions. In some vesicle populations, vesicles that are connected to each other occur. One such example is in Fig. 6.1. If vesicles in such groups are not focused on properly during the video recording, multiple difficulties arise during the mosaicing and segmentation steps. First of all, the vesicles without a proper sharp representation will appear sharp in neither of the mosaics (the first median and the improved mosaic). Secondly, as the vesicles are overlapping and not separated, they are difficult to segment in the foreground detection steps. The result is usually a big bounding box containing the whole group, preventing to find a sharp representation (even if there is one) for its individual vesicles. Since the MRF2 algorithm does not depend on shape information for the segmentation, the overlapping vesicles do not render it useless. However, the regions with such groups

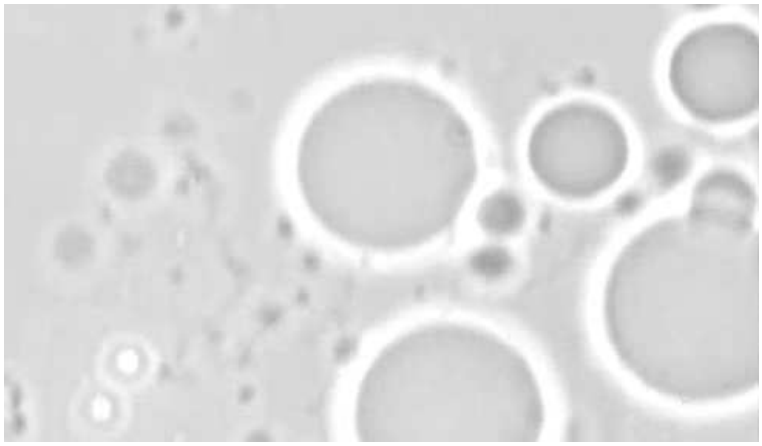

Figure 6.1 An example of a frame with indistinct vesicles. If vesicles in such groups are not focused on properly during the video recording, difficulties arise during the mosaicing and segmentation steps. The vesicle populations prepared with the presented protocol very rarely contain such groups of vesicles. It is much more convenient to prepare the vesicle populations with more effort, so complications in computerized steps can be avoided.

still require more time for manual corrections after the automated segmentation. Fortunately, the vesicle populations prepared with the presented experiment protocol very rarely contain such groups of vesicles. It is much more convenient to prepare the vesicle populations with more effort, so complications in computerized steps can be avoided.

In the final mosaics, boundaries between the vesicles blended onto the median mosaic using gradient fusion are not detectable. The results are even more pleasing because all mosaics are monochrome and color discrepancies, which can occur with Poisson blending, are avoided. To further validate the vesicle population in mosaics, the length of every mosaic in pixels is equal to the actual length of the recorded region in the corresponding specimen.

6.3 Vesicle segmentation from synthesized images

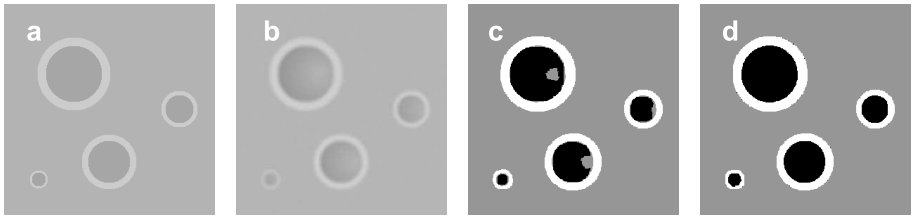

Figure 6.2 An example of a synthesized image with vesicles. (a) The template for synthetic vesicle preparation, (b) synthetic vesicle model, (c) synthetic vesicles segmented with basic MRF (at $\sigma = 5$, noise = 0.02), and (d) synthetic vesicles segmented with our MRF2

The proposed MRF2 segmentation is first tested on synthesized images with vesicles. These are produced with Matlab and resemble the actual vesicles of sizes 5-20 μm when recorded at 400x magnification with optical microscopy (Fig. 6.2). For generating these images, both MRF segmentation models require mean values and standard deviations of all regions' gray intensity levels. These are gathered from the vesicle images (Fig. 6.2b) with the use of the template image as a mask (Fig. 6.2a) to extract points from a single region. This way, the mean and standard deviations are the same as that of the ground truth. The synthesized image segmentation is performed to test both, the original MRF and our improved MRF2, algorithms on images of different qualities (blurred and noisy). In order to create variable image characteristics, the synthetic image is distorted by first applying a smoothing filter and then adding noise. Smoothing is performed with the

Gaussian filter of 7×7 pixels, and noise addition is simulated by adding a random matrix with uniformly distributed values to the image. To obtain results with different image characteristics, the standard deviations for the Gaussian filter are set to $\sigma = 1, 3, 5, 7, 9$, and the noise matrix is multiplied by 0.005, 0.01, 0.02, 0.03, and 0.05. The results of the synthetic image segmentation with all standard deviations and noise levels are presented in Fig. 6.3b and 6.3c. As the images are synthesized from a template image, the ground truth label boundaries are known and can be used to assess segmentation accuracy of both segmentations.

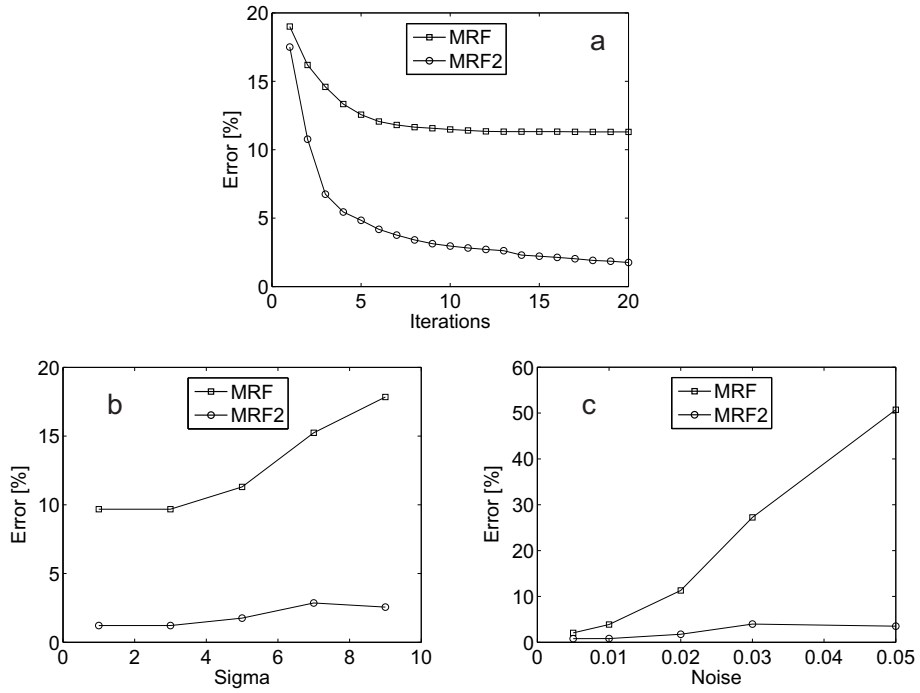

Figure 6.3 Comparison of MRF and MRF2 segmentation on synthesized images. (a) Segmentation error of both segmentation models dependent on iterations, (b) segmentation error due to varying smoothing parameter σ, and (c) segmentation error due to varying noise level.

The misclassification rate (segmentation error) is the percentage of pixels that were not classified into the correct class. It is recorded during each iteration of the Iterated conditional modes (ICM) algorithm. The segmentation error in the case of MRF2 is much lower than with the original MRF (2% vs. 12%) (Fig. 6.3a). Fig. 6.3b shows the dependence of the segmentation error on the smoothing parameter σ. The error increases with σ in both cases, but the MRF2 method at largest smoothing level ($\sigma = 9$)

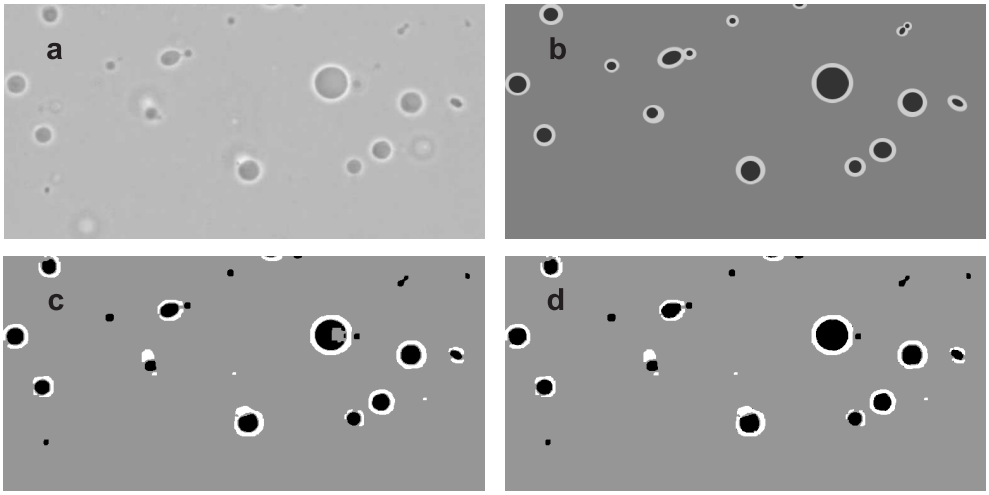

Figure 6.4 (a) Original image of the vesicles, (b) manually segmented image with three classes - background, halo, and vesicle, (c) original image segmented with basic MRF, and (d) original image segmented with our MRF2.

outperforms the MRF method even at the smallest smoothing level ($\sigma = 1$). Fig. 6.3c shows how the noise level influences the segmentation accuracy. Even though the MRF accuracy is reduced to a 50% classification error, the proposed MRF2 is not susceptible to increased noise and achieves only 5% error rate in images with the most noise. Results obtained with the MRF2 segmentation in Fig. 5.4c show that all vesicles are segmented successfully, whereas the segmentation obtained with the original MRF (Fig. 5.4b) is unsuccessful in filling the vesicle insides. The heuristics for MRF2 are set as $\gamma = 2$ and $\Delta = 6$. These values are optimal for this and all subsequent examples. The parameter β of the energy function U is set to 2 after testing for an appropriate value.

6.4 Vesicle segmentation from micrographs

To verify the accuracy of the algorithm on images of real vesicles, we manually segmented two micrographs with 15 vesicles (Figure 6.4) and 10 vesicles (Figure 6.5), and compared the segmentation accuracy of the MRF and MRF2 algorithms. In both cases, the MRF2 provides superior accuracy (1% error compared to 4% error, Figure 6.6). The mean values and variances of intensity levels for each of the three regions were obtained from multiple manually labeled micrographs (one of them is presented in Figure 5.2).

The main difference that can be observed in both examples is that the MRF2 com-

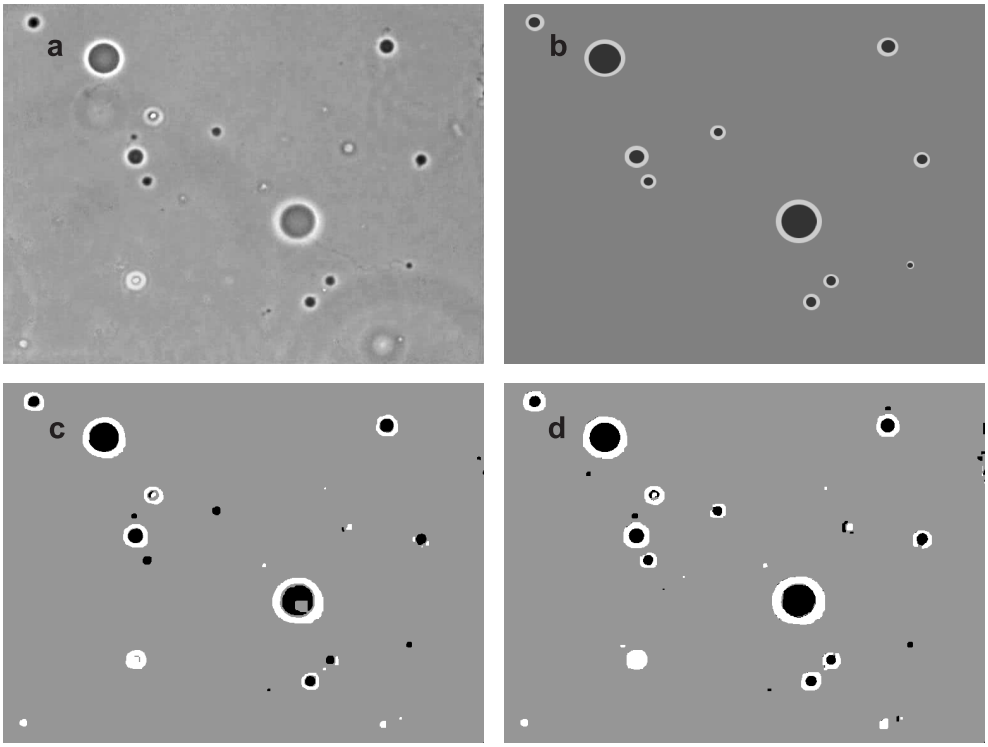

Figure 6.5 (a) Original image of the vesicles, (b) manually segmented image with three classes - background, halo, and vesicle, (c) original image segmented with basic MRF, and (d) original image segmented with our MRF2.

pletely filled the vesicle insides while the MRF algorithm filled them only partially. The results in Figure 6.6a and 6.6b show the error rate of each algorithm after each iteration of the ICM algorithm. The MRF2 image segmentation model reached the final accuracy after 7 iterations in both cases while the error rate of the MRF stopped decreasing after 15.

6.5 Experiment with cobalt-ferrite nanoparticles (video)

The only experiment where video sequences were recorded is the $CoFe_2O_4$ nanoparticle experiment. In this experiment (results published in the Journal of Biomedical Optics [4]), microscopy video sequences of vesicles incubated in three different suspensions were recorded and each video sequence of an investigated area was stitched into a mosaic. The vesicles were then manually segmented from the mosaics and their sizes and shapes evaluated. In short, the experiment was used to assess the effect of $CoFe_2O_4$ nanopa-

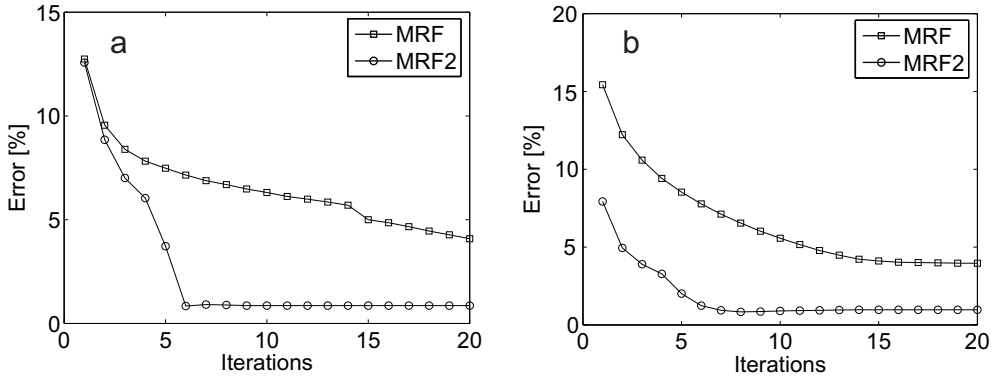

Figure 6.6 Segmentation error of both, MRF and MRF2 algorithms on (a) Figure 6.4 and (b) Figure 6.5.

rticles on the population of vesicles. Three vesicle populations were examined. The first was exposed to neutral $CoFe_2O_4$ nanoparticles (CF), the second to negatively charged citrate-coated $CoFe_2O_4$ nanoparticles (CF-CA) and the third population was left unexposed and used as a control (C). The duration of exposure in all three cases was 90 minutes, and the three populations were recorded immediately after exposure and again after 90 minutes, altogether 6 videos.

6.5.1 Vesicle segmentation in mosaics

In this section, we focus on two aspects of the $CoFe_2O_4$ experiment. First, the proposed MRF2 automated segmentation is compared to the manual segmentation [4] (its accuracy and operator's time requirement), and second, the results obtained from the analysis of the 6 segmented mosaics are presented.

We use the mosaics from the described experiment to test the proposed MRF2 and compare it to the manual segmentation, focusing on the time required and the segmentation accuracy. All together, 6 mosaics are investigated, each containing between 800 and 2200 vesicles. The time required for completely manual segmentation varies from 5 to 10 hours per mosaic, averaging at 8 hours (Figure 6.7b). It took an operator approximately 50 hours of concentrated work to segment the vesicles in these few mosaics. For the results to become more relevant, the experiment would have to be repeated at least a couple more times, demanding weeks of an operator's manual segmentation. This was the original motivator for automating the vesicle segmentation.

The proposed MRF2 algorithm requires almost no human involvement. The algorithm

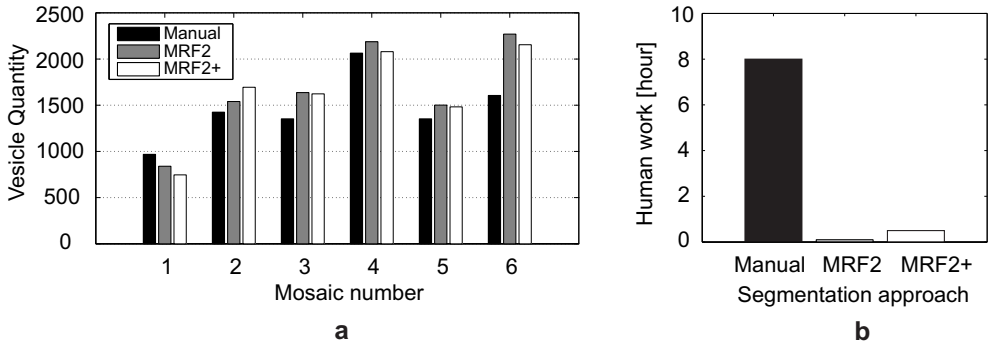

Figure 6.7 Vesicle quantity in mosaics segmented manually and automatedly. (a) Vesicle quantities in each of the six mosaics according to the manually labeled, automatedly segmented (MRF2) or automatedly segmented with minor corrections by the operator (MRF2+). (b) Average number of hours of the operator's time required for each of the three approaches.

is set to over-segment the mosaic preferring false positives in detected vesicles over false negatives. False positives are the objects which are detected, but are not vesicles. False negatives are vesicles that are missed by the segmentation. After the automated MRF2 segmentation, the acquired segmented mosaics are checked by the operator (we refer to these segmentations as MRF2+) to:

- delete the false positive vesicle labels,
- add vesicle labels for vesicles missed by the automated segmentation,
- identify non-spherical vesicles and label them with distinct colors (Figure 6.8).

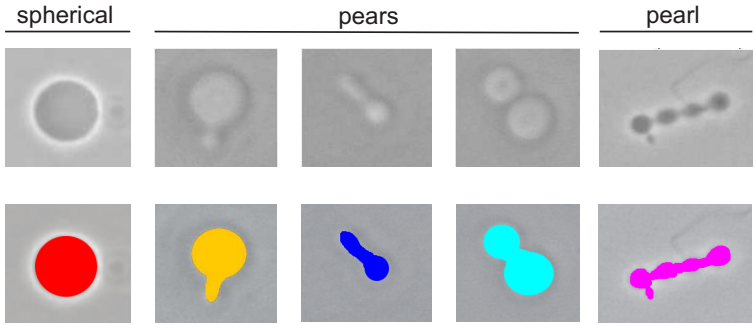

Figure 6.8 A legend with typical representatives of spherical vesicles, different pears, and a pearl.

Consequently, one can rely on the results obtained by combining the MRF2 auto-

mated segmentation and only minimal human involvement described above (MRF2+). Identifying and labeling the non-spherical vesicles (approximately 15% of the population) with distinct colors, allows analyzing the frequencies of their occurrences in the populations. In the case of the $CoFe_2O_4$ experiment, the two observed nonspherical types of vesicles are the pears and the pearls Fig. 6.8.

The results obtained with both approaches are presented in Figure 6.7a, where quantities of vesicles detected in each of the 6 mosaics by manual segmentation are compared to the detected quantities by solely MRF2 algorithm or the MRF2 algorithm with the operator's corrections (MRF2+). As expected, the MRF2 over-segmented the mosaics in 5 out of 6 cases, but the operator's time requirement for corrections was below 1 hour per mosaic on average. All together, the time required for analyzing data after such experiment is decreased more than eightfold compared to the solely manual segmentation. All mosaics were checked by a second operator afterwards and the MRF2+ was confirmed to be the best approximation of the ground truth.

6.5.2 Vesicle size and shape transformations

The accuracy of the MRF2+ segmentation also enables the analysis of spherical vesicle diameter sizes. We are able to detect the following differences between CF, CF-CA and C populations. The mean diameter of the spherical vesicles in the control population (C) decreases from 6.5 μm to 6 μm after 90 minute incubation, while the mean diameters in the CF and CF-CA populations increase to 8.1 μm and 8.5 μm, respectively (Fig. 6.9). Moreover, non-spherical vesicles are up to three times more likely to appear in CF and CF-CA exposed populations than in the C population (Fig. 6.9b). The differing occurrence of pearls is especially noticeable (Fig. 6.9c). Nonspherical vesicles represent from 5-15% of all vesicles in the exposed populations.

Another detected difference is in the distribution of the diameter sizes of the vesicles in the populations. We can observe minimal changes of cumulative distribution function (CDF) in the C population before and after 90 minutes of incubation, whereas results from the CF and CF-CA populations suggest significantly more vesicles with larger diameter (Fig. 6.10). The total quantity of segmented vesicles in all experimental populations (both times of exposure, 0 and 90, combined) together is 9781 (according to MRF2+).

Our data on size and shape transformations of giant lipid vesicles incubated in a suspension of nanoparticles confirm findings described by other authors [16, 38]. Incu-

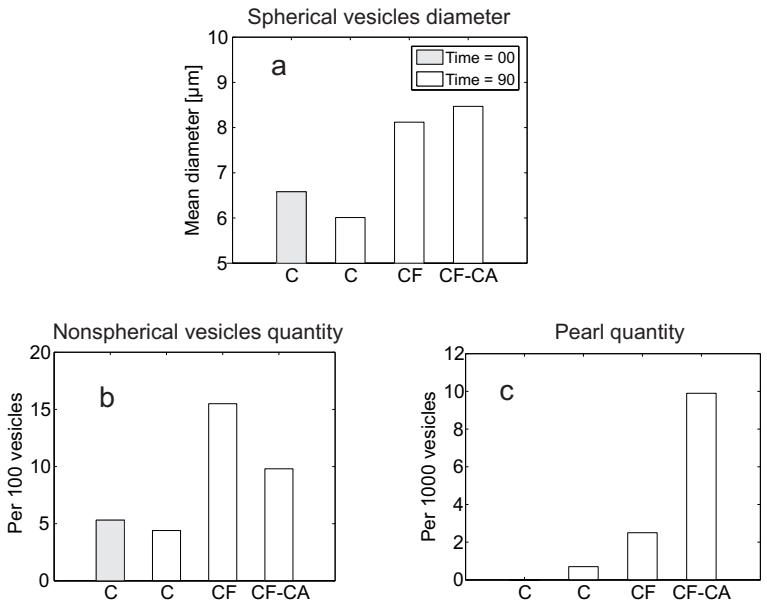

Figure 6.9 (a) Mean diameter size of spherical vesicles for each experimental population, (b) number of nonspherical vesicles per 100 vesicles and (c) number of pearls per 1000 vesicles. The experimental populations are: C - control, CF - neutral Cobalt-ferrite nanoparticles and CF-CA - negatively charged citrate-coated Cobalt-ferrite nanoparticles. Vesicles in the C population are observed at time 0, and vesicles in all three populations are observed after 90 minutes of incubation.

bation in a suspension of neutral $CoFe_2O_4$ (CF) or negatively charged citrate-coated $CoFe_2O_4$ nanoparticles (CF-CA) results in an increased quantity of nonspherical vesicles (Fig. 6.9b-c), the increase being most notable in occurrences of pearls [16]. Yu et al. [16] also reported formation of pearls as a result of interaction between lipid vesicles and negatively charged nanoparticles. They explain that cationic nanoparticles adsorb onto vesicles causing a mismatch of surface area between the outer and inner leaflets of the bilayer, resulting in formation of pearls.

6.6 Experiment with fullerene nanoparticles (micrographs)

In the first stage of research on interactions between nanoparticles and lipid vesicles, we conducted an experiment with vesicles and fullerene nanoparticles C_{60} (results published in the International Journal of Biomedical Nanoscience and Nanotechnology [3]).

The experiment was conducted three times (in order to gather information on variability of results), similarly to the protocol described in § 3, with only minor differences

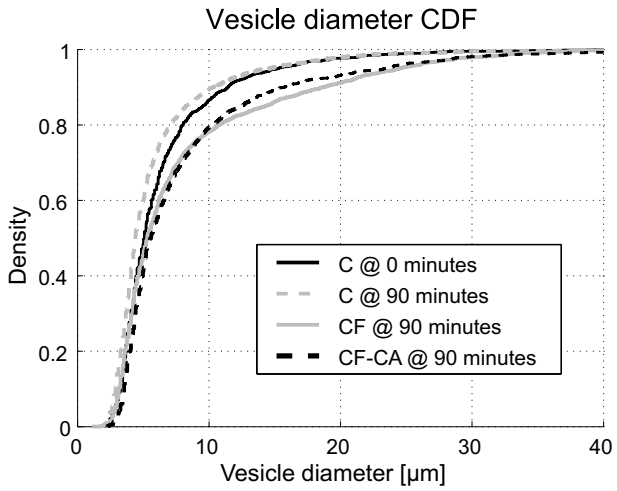

Figure 6.10 Each curve presents a cumulative distribution function (CDF) of the diameters of spherical lipid vesicles. The X axis gives sizes of the lipid vesicles in micrometers and F(X) is percentage of all vesicles with diameter smaller than X. We can observe minimal changes of CDF in the C group before and after 90 minutes of incubation. However, the distributions in the sizes of CF and CF-CA lipid vesicles suggest notably more vesicles with larger diameter. The vesicles with diameters above 40 μm are not shown because they represent less than 0.5% of the vesicle population.

(also presented in a scheme in Fig. 6.11):

- besides the control and nanoparticle exposed populations, a reference population was exposed to $ZnCl_2$ and served as a positive control,
- instead of recording only a single location at each object glass, two locations were recorded, which are referred to as P1 and P2. The location P1 was close to the place where the C_{60}, $ZnCl_2$, or glucose were added. The distance between P1 and P2 was approximately 4 mm. This was done in order to capture a concentration gradient.
- instead of recording a video sequence, 15 micrographs were acquired at each track, uniformly distributed. In comparison with the video, this is approximately 15% of the track.

First sets of images were obtained immediately after suspensions of vesicles had been applied and covered by cover glasses. These images are referred to as being taken at time 1. The next sets of images were taken after 5 μl of either control (glucose solution),

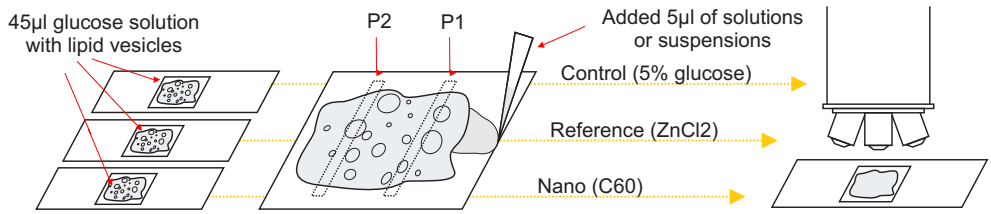

Figure 6.11 Sequence of steps in the experiment with fullerenes is presented from left to right. First, equal volumes of glucose solution with lipid vesicles are added to three object glasses. Second, either nanoparticles, a reference chemical or a glucose solution only are added to either of the samples. Two places: P1 and P2 are defined as observing places on the object glass. Finally, multiple images of these places (in all three samples) were acquired after different duration of exposures by a camera, attached to the microscope (figure not to the scale).

nanoparticles (C_{60}) in a glucose solution or a reference chemical ($ZnCl_2$) in glucose solution had been added to vesicles. For the convenience of the analysis, these sets are referred to as being taken after 10 minutes of incubation. Third and the last sets of images were taken after 100 minutes of incubation. As at the time of this experiment, no automated vesicle segmentation methods for the vesicle populations had been developed, 7670 vesicles in 810 images were manually segmented using the Shape Segmenter plug-in. The segmented vesicles were then analyzed with Matlab, and vesicle size distributions of vesicle populations, vesicle quantities and the percentage of binding vesicle occurrences in vesicle populations were compared.

6.6.1 Quantities of all vesicles

Fig. 6.12 shows quantities of vesicles incubated in C_{60} (N-ano) or $ZnCl_2$ (R-eference) compared to quantities of unexposed ones (C-ontrol). Quantities of vesicles at place P1 were affected by both added substances. The vesicles at place P2 were affected only by $ZnCl_2$ while the vesicles in C and N populations remained unaffected.

Quantity of vesicles at place P1 was reduced due to C_{60} or $ZnCl_2$ exposure already in the first 10 minutes after addition. Here the quantity of vesicles was significantly lower than before addition of substances. After prolonged incubation (100 minutes) the response did not increase and the quantity of vesicles remained the same throughout the duration of experiment. Quantity of vesicles at place P2 was significantly reduced only when incubated with $ZnCl_2$. The effect was not noticeable before 100 minutes of incubation. The effect of C_{60} was minimal. The amount of vesicles at all places (P1 and

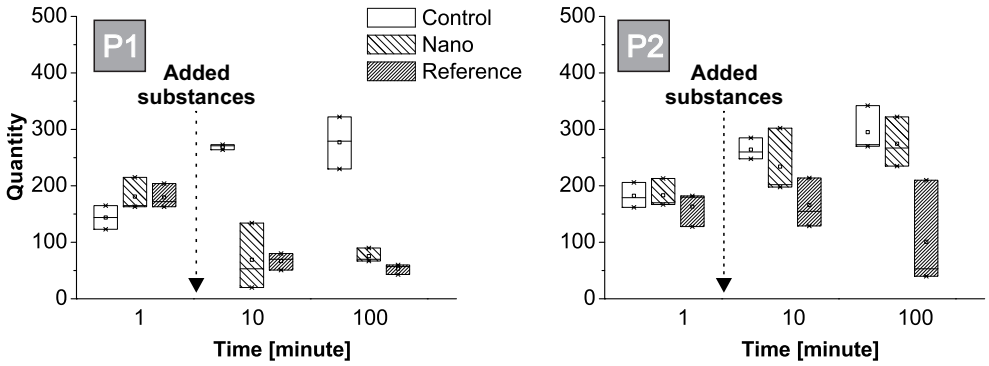

Figure 6.12 Quantities of vesicles at both places on the object glass: P1 (left), and P2 (right). Each box plot represents quantity of vesicles (unexposed (C) or exposed (N, R)) after a specific duration of incubation. It is composed of quantities detected at three repetitions of the experiment. The lower line represents the lowest quantity, the central line the second lowest and the upper line the highest quantity detected. The small square in the center of the box plot is the mean value of quantities of all three experiments. At P1, the quantity of vesicles in population decreased whether it was exposed to nanoparticles or the reference chemical, whereas quantity of vesicles in the unexposed population did not decrease. At P2, the vesicles were affected by the reference chemical only, and the effect happened after 100 minutes of incubation.

P2) before the start of incubation was in the range of 150-200 per observed area. After 100 minutes of exposure, there were five times less vesicles in the exposed populations compared to the unexposed one. The quantity of all segmented vesicles (two places, three experiments with three populations at three different times of incubation) was 7670. In the first 10 minutes and throughout the duration of experiment, quantities of vesicles in all unaffected samples increased. We explain this with the gravitational effect, due to negative buoyancy of the vesicles it takes a few minutes for them to collect in the focal plane, at the bottom of the observation chamber.

The effect at P1 is more or less instant with both added substances, the quantity of vesicles drops significantly in the first minutes compared to the unexposed population (Fig. 6.12). The effect at P2 is notable only with $ZnCl_2$. The C_{60} affected only close to the location of addition, while the $ZnCl_2$ affected the P2 too. We explain this quantity related effect by bursting induced by the added C_{60} or $ZnCl_2$. At P1, which was most affected, approximately 4 out of 5 incubated vesicles burst.

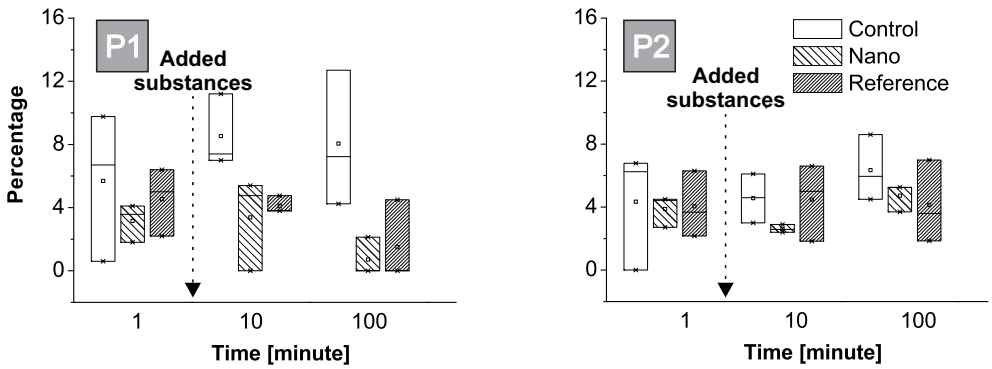

Figure 6.13 Portions of pears in the vesicle populations at each of the three places on the object glass: P1, and P2. Each box plot represents percentage of pears (unexposed (C) or exposed (N, R)) in the vesicle population after a specific duration of incubation. The box plot is composed of quantities detected in three repetitions of the experiment. The lower line represents the lowest percentage, the central line the second lowest and the upper line, the highest percentage detected. The small square in the center of the box plot is the mean value of quantities of all three experiments. Charts respectively present places P1 (left) and P2 (right).

6.6.2 Portion of pears in vesicle populations

Fig. 6.13 shows portions of pears in the vesicle populations. That is the percentage of all vesicles that were classified as pears in the whole vesicle population. Each box plot represents three experiments (lower, middle and upper line) and the small square is the mean value of the percentages in all three experiments. At P1, the portion of pears in the unexposed populations (where only additional glucose solution was added) increases to an average of 8% during the first ten minutes of the incubation. The portion in the unexposed populations remains below 4%. The effect is not notable at P2, where the average (of three experiments) pears portions of unexposed populations is similar to that of the exposed ones after all durations of incubation.

6.6.3 Vesicle size cumulative distribution functions

Fig. 6.14 presents vesicle size cumulative distribution functions of vesicles at different places and after different durations of incubation. The interpretations of the curves are presented in the legend below (Fig. 6.14).

At place P1 there were no differences in size distributions of vesicles before the addition of substances. However, after 10 minutes of incubation a significant difference was observed where the vesicles were incubated with $ZnCl_2$. Here, the majority of remaining

vesicles had a diameter significantly smaller when compared to control or C_{60} exposed vesicles or those before the incubation. After 10 minutes of exposure of control and C_{60} incubated vesicles no differences in size distributions were observed. After 100 minutes of exposure, the effect of $ZnCl_2$ is even more pronounced than after the first 10 minutes. Still, the size distributions in other two groups were not altered. At place P2, no differences in size distributions before the start of incubation or after 10 minutes after incubation were observed. After 100 minutes of incubation, again, vesicles exposed to $ZnCl_2$, were affected. Here the average diameter of vesicles was smaller than average diameter of unexposed or those vesicles exposed to nanoparticles.

6.6.4 Discussion

The results obtained show that tested concentrations of both C_{60} and $ZnCl_2$ have the potential to affect the lipid vesicles. Interactions in our experiments led to a collapse of vesicles, which resulted in changed quantities of vesicles and, in the case of $ZnCl_2$, in a significant change in size distribution of vesicles. Shape transformations were not observed to be significantly altered by neither of tested substances. Vesicles' size distribution of a population of vesicles is related to duration of exposure and concentration of tested substance. Very pronounced differences were detected already after 10 min of exposure to C_{60} or $ZnCl_2$. Data on size distributions of vesicles needs to be interpreted together with data on the quantity of vesicles in order to not underestimate the effect of C_{60} or $ZnCl_2$.

Similar data on the potential of C_{60} to interact with biological membranes were reported also by other authors. The damage of C_{60} colloidal suspension to cell membranes was observed both with chemical assays, and confirmed physically by visualizing membrane permeability with high molecular weight dyes [102]. The results presented by Tang Yinjie et al. [103] favor the hypothesis that fullerenes cause more membrane stress than perturbation to energy metabolism. It is also explained that shape transformations of vesicles are governed by curvature and bending elasticity [35, 104, 105]. The lipid vesicles could be deflected by osmotic pressure [22], rising the temperature [106, 107] or electric fields, or by different surfactants [108]. At present stage we cannot explain the mode of action of nanoparticles or $ZnCl_2$ on vesicles.

$ZnCl_2$ was used in our study as a reference chemical in positive control to provoke the shape transformations of vesicles. In a negative control, vesicles were treated only

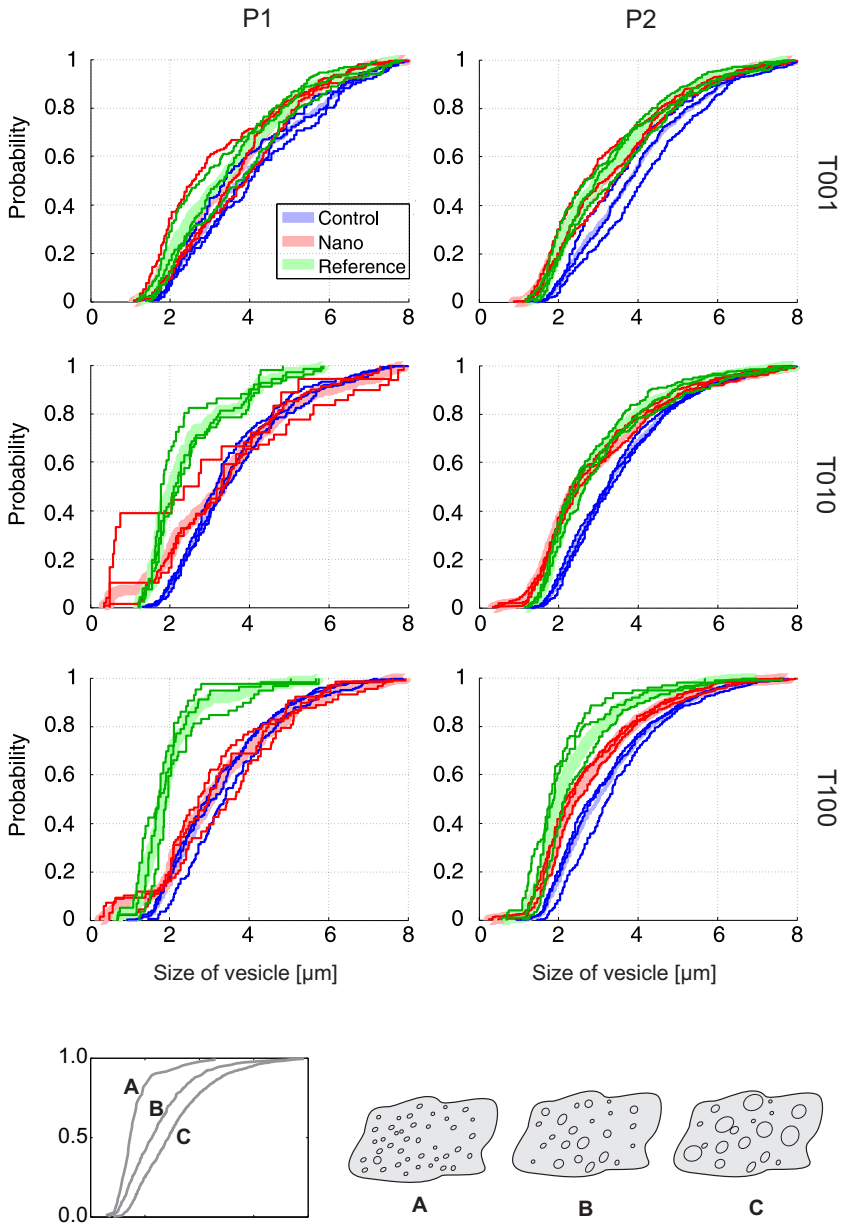

Figure 6.14 Vesicle diameter size cumulative distribution functions of vesicles at different places and after different durations of incubation. Each curve presents a cumulative distribution function (CDF) of the diameters of lipid vesicles. The X axis gives sizes of the lipid vesicles in micrometers and F(X) is percentage of all vesicles with diameter smaller than X. The two columns represent P1 (left) and P2 (right), and each line is a specific time of recording micrographs in minutes. The wide line is the average of the three experiments (each of the three thin lines of the same color).

with glucose solution. Reference chemical appeared to be adequately selected since statistically significant differences between behavior of control vesicles and those treated with a reference chemical were recorded. Besides, the effects of C_{60} on lipid vesicles were different from that on the reference chemical. This is a proof that the effects are not provoked by experimental conditions (rising temperature, osmotic pressure etc.) but are due to a specific mode of action of the tested substance.

7 Conclusion

In this dissertation, we have developed a methodology for assessing the shape and size changes in populations of giant unilamellar lipid vesicles. Instead of observing isolated vesicles, this methodology allows extraction of data on size and shape of thousands of vesicles incubated in different media. The methodology begins with a protocol on how to prepare a vesicle experiment and record tracks of vesicle populations exposed to different nanoparticles. Although we propose and test this methodology for the use in studies on bio-nano interactions, it can be used to assess the effects of any additive or change (electrical or magnetic field, temperature etc.) to the vesicle population. Next, we present image processing methods for stitching mosaics from the video sequences. The resulting mosaic is composed of a smooth mosaic (assembled by temporal median filtering all but the most distorted video frames) with the sharpest representations of vesicles which were blended onto it by gradient fusion. The next stage is a Markov Random Field image segmentation model, which is adapted for segmenting the vesicles. As this segmentation is tuned to prefer the false positives, the resulting segmentation has to be checked by the operator. This human involvement is only minor, on average

about eight times less time consuming than completely manual vesicle segmentation. Finally, a statistical analysis is conducted from the extracted vesicle masks, which can be used to assess whether the observed vesicle populations differ. Using this methodology, differences in the morphological properties of lipid vesicles incubated in a suspension with or without nanoparticles are demonstrated through two experiments. Through a population experiment, repeated three times, we show that C_{60} nanoparticles induce bursting of vesicles. This way, the repeatability of the methodology is confirmed and also its ability to capture quantity and size data on vesicles. The experiment, where video sequences are recorded and stitched into mosaics is with the $CoFe_2O_4$ nanoparticles. Through applying the algorithms to this dataset we verify the mosaic stitching and vesicle segmentation. In addition, differences in shape transformations of populations of lipid vesicles incubated with cobalt-ferrite nanoparticles were detected.

7.1 Future work

The presented methodology is an important milestone in our bio-nano research and holds much promise in its future applications. The prototype software described here is prepared to process data from new experiments. Some directions that should be considered for future steps, to improve the methodology, and its application in lipid vesicle studies, are presented in this section.

- The most time consuming step is the direct registration of frames in the video sequence. Currently, each two subsequent frames are registered with normalized cross-correlation, which is performed by sliding one (template) frame over the whole surface of the second frame and computing cross-correlation at every pixel. However, the consequence of continuity of frames in the video sequence is the continuity in the subsequent translations between them. With the use of the history of translations, every new translation could be predicted (e.g. Kalman filter) and the peak value of normalized cross-correlation could be identified only among the pixels in the proximity of the predicted translation.

- Instead of employing the foreground detection to identify the objects (majority of which are vesicles), a Watershed transform [109] could be employed to divide the mosaic into segments. These segments would play the role of bounding boxes with one important advantage. The watershed boundaries are not rectangular

and can adapt to true boundaries between objects, which is not possible with bounding boxes. However, such approach also comes with weaknesses. As the areas segmented by Watershed transform are not rectangular, algorithms for their processing (such as registration and region based sharpness measures), which are implemented for rectangular regions, have to be adapted.

- Extend the methodology from 1-dimensional to arbitrary 2-dimensional mosaics.
- The implementation could be ported to C++ for its performance and portability.
- Currently wide spread open source microscopy mosaicing software packages should be investigated in detail to evaluate the potential applicability of our algorithm to their solutions.
- The most important step is to conduct a valid and extensive null experiment without additives and by recording video sequences to test: repeatability of population size (among the recording places of the same population), repeatability of vesicle size distributions in populations, and repeatability of non-spherical vesicle portions in populations.
- Test different time frames of recording to allow us following an even more detailed time dependent response.
- Finally, routinely use the methodology for its purpose.

In the future, studies on lipid vesicles could provide basic understanding of nanoparticle-membrane interactions and more, the information on biological reactivity of nanoparticles could be used as an additional, biological characteristic of nanoparticles beside their physicochemical properties. The method presented here holds many promises for future investigation of the potential of different nanoparticles to interact with lipid membranes. We presented here an approach for studying nanoparticle–membrane interactions under controlled conditions. The application of image processing methods in investigating shape transformations of vesicles illustrates the potential of computational imaging in understanding of the dynamics of nanoparticle-vesicle interactions.

We conclude that the methodology presented holds much promise for future studies on responses of lipid vesicle populations to various substances. Among these, nanoparticles are perhaps the most challenging and interesting.

BIBLIOGRAPHY

[1] J. Zupanc, J. Valant, A. Dobnikar, V. Kralj-Iglic, A. Iglic, and D. Drobne, "Interactions of nanoparticles with lipid vesicles: A population based computer aided image analysis approach," in *Proc. Annual Int. Conf. of the IEEE Engineering in Medicine and Biology Society EMBC*, 2009, pp. 1400–1403.

[2] J. Zupanc, E. Bas, and D. Erdogmus, "Analysis of lipid vesicle populations from microscopy video sequences," in *Proc. Annual Int. Conf. of the IEEE Engineering in Medicine and Biology Society EMBC*, 2010, pp. 5050–5053.

[3] J. Zupanc, J. Valant, D. Drobne, V. Kralj-Iglic, and A. Iglic, "A new approach to analyse effects of nanoparticles on lipid vesicles," *International Journal of Biomedical Nanoscience and Nanotechnology*, vol. 1, no. 1, pp. 34–51, 2010.

[4] J. Zupanc, A. Dobnikar, D. Drobne, J. Valant, D. Erdogmus, and E. Bas, "Biological reactivity of nanoparticles: mosaics from optical microscopy videos of giant lipid vesicles," *Journal of Biomedical Optics*, vol. 16, no. 2, pp. 26 003–10, 2011.

[5] J. Zupanc, B. Ster, and D. Drobne, "Markov random field model for segmenting large populations of lipid vesicles from micrographs," *Journal of Liposome Research*, 2011.

[6] J. Zupanc and D. Drobne, "Populacije orjaških lipidnih veziklov kot model za študij bio-nano interakcij," *Informatica Medica Slovenica*, vol. 16, no. 1, pp. 1–12, 2011.

[7] C. Toumey, "Reading Feynman into nanotechnology: a text for a new science," *Techne*, vol. 12, pp. 133–168, 2008.

[8] D. Drobne, "Nanotoxicology for safe and sustainable nanotechnology," *Arhiv za higijenu rada i toksikologiju*, vol. 58, no. 4, pp. 471–478, 2007.

[9] K. Schmidt, "The great nanotech gamble," *The New Scientist*, vol. 195, no. 2612, pp. 38–41, 2007.

[10] K. L. Dreher, "Health and Environmental Impact of Nanotechnology: Toxicological Assessment of Manufactured Nanoparticles," *Toxicological Sciences*, vol. 77, no. 1, pp. 3–5, 2004.

[11] F. Giacobbe, L. Monica, and D. Geraci, "Nanotechnologies: Risk assessment model," *Journal of Physics: Conference Series*, vol. 170, p. 012035, 2009.

[12] P. Hoet, B. Legiest, J. Geys, and B. Nemery, "Do nanomedicines require novel safety assessments to ensure their safety for long-term human use?" *Drug safety: an international journal of medical toxicology and drug experience*, vol. 32, no. 8, pp. 625–636, 2009.

[13] J. Valant, D. Drobne, K. Sepcić, A. Jemec, K. Kogej, and R. Kostanjsek, "Hazardous potential of manufactured nanoparticles identified by in vivo assay," *Journal of hazardous materials*, vol. 171, no. 1-3, pp. 160–165, 2009.

[14] H. Jin, D. a. Heller, R. Sharma, and M. S. Strano, "Size-dependent cellular uptake and expulsion of single-walled carbon nanotubes: single particle tracking and a generic uptake model for nanoparticles," *ACS nano*, vol. 3, no. 1, pp. 149–158, 2009.

[15] B. J. Marquis, S. A. Love, K. L. Braun, and C. L. Haynes, "Analytical methods to assess nanoparticle toxicity," *The Analyst*, vol. 134, no. 3, pp. 425–439, 2009.

[16] Y. Yu and S. Granick, "Pearling of lipid vesicles induced by nanoparticles," *Journal of the American Chemical Society*, vol. 131, no. 40, pp. 14 158–9, 2009.

[17] J. Fendler, "Atomic and molecular clusters in membrane mimetic chemistry," *Chemical Reviews*, vol. 87, no. 5, pp. 877–899, 1987.

[18] C. Peetla, A. Stine, and V. Labhasetwar, "Biophysical interactions with model lipid membranes: applications in drug discovery and drug delivery," *Molecular pharmaceutics*, vol. 6, no. 5, pp. 1264–1276, 2009.

[19] R. Dimova, S. Aranda, N. Bezlyepkina, V. Nikolov, K. Riske, and R. Lipowsky, "A practical guide to giant vesicles. Probing the membrane nanoregime via optical microscopy," *Journal of Physics: Condensed Matter*, vol. 18, no. 28, pp. 1151–1176, 2006.

[20] J. Käs and E. Sackmann, "Shape transitions and shape stability of giant phospholipid vesicles in pure water induced by area-to-volume changes," *Biophysical Journal*, vol. 60, no. 4, pp. 825–844, 1991.

[21] R. Lipowsky, "The conformation of membranes," *Nature*, vol. 349, no. 6309, pp. 475–481, 1991.

[22] L. Mathivet, S. Cribier, and P. Devaux, "Shape change and physical properties of giant phospholipid vesicles prepared in the presence of an AC electric field," *Biophysical Journal*, vol. 70, no. 3, pp. 1112–1121, 1996.

[23] S. Svetina and B. Zeks, "Shape behavior of lipid vesicles as the basis of some cellular processes," *The Anatomical record*, vol. 268, no. 3, pp. 215–225, 2002.

[24] P. Peterlin, G. Jaklič, and T. Pisanski, "Determining membrane permeability of giant phospholipid vesicles from a series of videomicroscopy images," *Measurement Science and Technology*, vol. 20, no. 5, p. 055801, 2009.

[25] L. R. Arriaga, R. Rodríguez-García, I. López-Montero, B. Farago, T. Hellweg, and F. Monroy, "Dissipative curvature fluctuations in bilayer vesicles: Coexistence of pure-bending and hybrid curvature-compression modes," *The European physical journal. E, Soft matter*, vol. 31, no. 1, pp. 105–113, 2010.

[26] Pavlic, Janez, "Interactions of charged and superparamagnetic nanoparticles with lipid model membranes," Ph.D. dissertation, University of Ljubljana, Faculty of Electrical Engineering, 2010.

[27] H. G. Döbereiner, J. Käs, D. Noppl, I. Sprenger, and E. Sackmann, "Budding and fission of vesicles," *Biophysical journal*, vol. 65, no. 4, pp. 1396–1403, 1993.

[28] S. Hong, P. R. Leroueil, E. K. Janus, J. L. Peters, M. M. Kober, M. T. Islam, B. G. Orr, J. R. Baker, and M. M. Banaszak Holl, "Interaction of polycationic polymers with supported lipid bilayers and cells: Nanoscale hole formation and enhanced membrane permeability," *Bioconjugate Chemistry*, vol. 17, no. 3, pp. 728–734, 2006.

[29] J. Pécréaux, H. G. Döbereiner, J. Prost, J. F. Joanny, and P. Bassereau, "Refined contour analysis of giant unilamellar vesicles," *The European physical journal. E, Soft matter*, vol. 13, no. 3, pp. 277–290, 2004.

[30] T. Gruhn, T. Franke, R. Dimova, and R. Lipowsky, "Novel method for measuring the adhesion energy of vesicles," *Langmuir: the ACS journal of surfaces and colloids*, vol. 23, no. 10, pp. 5423–5429, 2007.

[31] C. T. Leirer, B. Wunderlich, A. Wixforth, and M. F. Schneider, "Thermodynamic relaxation drives expulsion in giant unilamellar vesicles," *Physical biology*, vol. 6, no. 1, p. 016011, 2009.

[32] H. G. Dobereiner, "The Budding Transition of Phospholipid Vesicles: A Quantitative Study via Phase Contrast Microscopy," Ph.D. dissertation, 1995.

[33] H. G. Döbereiner, E. Evans, M. Kraus, U. Seifert, and M. Wortis, "Mapping vesicle shapes into the phase diagram: A comparison of experiment and theory," *Physical Review E*, vol. 55, no. 4, pp. 4458–4474, 1997.

[34] J. Barauskas, C. Cervin, M. Jankunec, M. Spandyreva, K. Ribokaite, F. Tiberg, and M. Johnsson, "Interactions of lipid-based liquid crystalline nanoparticles with model and cell membranes," *International journal of pharmaceutics*, vol. 391, no. 1-2, pp. 284–291, 2010.

[35] A. Imparato, J. C. Shillcock, and R. Lipowsky, "Shape fluctuations and elastic properties of two-component bilayer membranes," *Europhysics Letters (EPL)*, vol. 69, no. 4, pp. 650–656, 2005.

[36] J. Liu and A. J. Hopfinger, "Identification of possible sources of nanotoxicity from carbon nanotubes inserted into membrane bilayers using membrane interaction quantitative structure–activity relationship analysis," *Chemical research in toxicology*, vol. 21, no. 2, pp. 459–466, 2008.

[37] D. Drobne and V. Kralj-Iglic, "Chapter 5: Lipid membranes as tools in nanotoxicity studies," ser. Advances in Planar Lipid Bilayers and Liposomes, A. L. Leitmannova and A. Iglic, Eds. Academic Press, 2009, vol. 10, pp. 121–134.

[38] B. Wang, L. Zhang, S. C. Bae, and S. Granick, "Nanoparticle-induced surface reconstruction of phospholipid membranes," *Proceedings of the National Academy of Sciences of the United States of America*, vol. 105, no. 47, pp. 18 171–5, 2008.

[39] R. Lipowsky and H. G. Döbereiner, "Vesicles in contact with nanoparticles and colloids," *Europhysics Letters*, vol. 43, no. 2, pp. 219–225, 1998.

[40] N. Rodriguez, J. Heuvingh, F. Pincet, and S. Cribier, "Indirect evidence of submicroscopic pores in giant unilamellar vesicles," *Biochimica et biophysica acta*, vol. 1724, no. 3, pp. 281–287, 2005.

[41] P. Leroueil, S. Hong, A. Mecke, J. Baker Jr, B. Orr, and M. Banaszak Holl, "Nanoparticle interaction with biological membranes: does nanotechnology present a Janus face?" *Accounts of chemical research*, vol. 40, no. 5, pp. 335–342, 2007.

[42] M. Angelova, S. Soléau, P. Méléard, F. Faucon, and P. Bothorel, "Preparation of giant vesicles by external AC electric fields. Kinetics and applications," in *Trends in Colloid and Interface Science VI*, ser. Progress in Colloid & Polymer Science, C. Helm, M. Lösche, and H. Möhwald, Eds. Darmstadt: Steinkopff, 1992, vol. 89, ch. 29, pp. 127–131.

[43] V. Kralj-Iglic, "Myelin-like protrusions of giant phospholipid vesicles prepared by electroformation," *Colloids and Surfaces A: Physicochemical and Engineering Aspects*, vol. 181, no. 1-3, pp. 315–318, 2001.

[44] M. D. Abramoff, P. J. Magelhaes, and S. J. Ram, "Image processing with imagej," *Biophotonics International*, vol. 11, no. 7, pp. 36–42, 2004.

[45] A. Agarwala, M. Dontcheva, M. Agrawala, S. Drucker, A. Colburn, B. Curless, D. Salesin, and M. Cohen, "Interactive digital photomontage," *ACM Transactions on Graphics*, vol. 23, no. 3, p. 294, 2004.

[46] M. Brown and D. G. Lowe, "Automatic Panoramic Image Stitching using Invariant Features," *Int. J. Comput. Vision*, vol. 74, no. 1, pp. 59–73, 2007.

[47] R. Silvers, *Photomosaics*, M. Hawley, Ed. New York, NY, USA: Henry Holt and Co., Inc., 1997.

[48] R. Szeliski, "Image alignment and stitching: A tutorial," *Foundations and Trends in Computer Graphics and Vision*, vol. 2, no. 1, pp. 1–104, 2006.

[49] S. K. Chow, H. Hakozaki, D. L. Price, N. a. B. MacLean, T. J. Deerinck, J. C. Bouwer, M. E. Martone, S. T. Peltier, and M. H. Ellisman, "Automated microscopy system for mosaic acquisition and processing," *Journal of Microscopy*, vol. 222, no. Pt 2, pp. 76–84, 2006.

[50] E. Flaberg, P. Sabelström, C. Strandh, and L. Szekely, "Extended Field Laser Confocal Microscopy (EFLCM): combining automated Gigapixel image capture with in silico virtual microscopy," *BMC medical imaging*, vol. 8, pp. 1–13, 2008.

[51] Y. Arzhaeva, P. Vallotton, and C. Sun, "Mosaicing of microscope images in the presence of large areas with insufficient information content," in *SPIE Symposium on Medical Imaging*, vol. 7623, 2010, pp. 762 338–8.

[52] C. Sun, R. Beare, V. Hilsenstein, and P. Jackway, "Mosaicing of microscope images with global geometric and radiometric corrections," *Journal of Microscopy*, vol. 224, no. Pt 2, pp. 158–165, 2006.

[53] M. Emmenlauer, O. Ronneberger, A. Ponti, P. Schwarb, A. Griffa, A. Filippi, R. Nitschke, W. Driever, and H. Burkhardt, "XuvTools: free, fast and reliable stitching of large 3D datasets," *Journal of Microscopy*, vol. 233, no. 1, pp. 42–60, 2009.

[54] B. Ma, T. Zimmermann, M. Rohde, S. Winkelbach, F. He, W. Lindenmaier, and K. Dittmar, "Use of autostitch for automatic stitching of microscope images," *Micron*, vol. 38, no. 5, pp. 492–499, 2007.

[55] J. Kopf, M. Uyttendaele, O. Deussen, and M. F. Cohen, "Capturing and viewing gigapixel images," *ACM Transactions on Graphics*, vol. 26, no. 3, p. 93, 2007.

[56] D. S. Gareau, Y. Li, B. Huang, Z. Eastman, K. S. Nehal, and M. Rajadhyaksha, "Confocal mosaicing microscopy in Mohs skin excisions: feasibility of rapid surgical pathology," *Journal of Biomedical Optics*, vol. 13, no. 5, p. 054001, 2008.

[57] D. S. Gareau, Y. G. Patel, Y. Li, I. Aranda, A. C. Halpern, K. S. Nehal, and M. Rajadhyaksha, "Confocal mosaicing microscopy in Mohs skin excisions: a demonstration of rapid surgical pathology," *Journal of Microscopy*, vol. 233, no. 1, pp. 149–159, 2009.

[58] S. Battiato, A. Bruna, and G. Puglisi, "A Robust Block Based Image/Video Registration Approach for Mobile Imaging Devices," *IEEE Transactions on Multimedia*, vol. 12, no. 7, pp. 622–635, 2010.

[59] D. Steedly, C. Pal, and R. Szeliski, "Efficiently registering video into panoramic mosaics," in *10th IEEE International Conference on Computer Vision*, vol. 2. IEEE, 2005, pp. 1300–1307.

[60] R. J. Radke, S. Andra, O. Al-Kofahi, and B. Roysam, "Image change detection algorithms: a systematic survey," *Image Processing, IEEE Transactions on*, vol. 14, no. 3, pp. 294–307, 2005.

[61] C. Hsu, "Mosaics of video sequences with moving objects," *Signal Processing: Image Communication*, vol. 19, no. 1, pp. 81–98, 2004.

[62] J. Davis, "Mosaics of scenes with moving objects," in *IEEE Computer Society Conference on Computer Vision and Pattern Recognition Proceedings*. IEEE Comput. Soc, 1998, pp. 354–360.

[63] A. Agarwala, K. C. Zheng, C. Pal, M. Agrawala, M. Cohen, B. Curless, D. Salesin, and R. Szeliski, "Panoramic video textures," in *ACM SIGGRAPH 2005 Papers on - SIGGRAPH '05*, vol. 1, no. 212. New York, New York, USA: ACM Press, 2005, pp. 821–824.

[64] P. Pérez, M. Gangnet, and A. Blake, "Poisson image editing," in *ACM SIGGRAPH 2003 Papers on - SIGGRAPH '03*, vol. 22. New York, New York, USA: ACM Press, 2003, p. 313.

[65] T. Vercauteren, A. Perchant, X. Pennec, and N. Ayache, "Mosaicing of confocal microscopic in vivo soft tissue video sequences," in *Lecture Notes in Computer Science, Proceedings of Medical Image Computing and Computer Assisted Intervention*, vol. 8, 2005, pp. 753–760.

[66] S. D. Backer, F. Cornelissen, and J. Lemeire, "Mosaicing of Fibered Fluorescence Microscopy Video," in *Proceedings of the 10th International Conference on Advanced Concepts for Intelligent Vision Systems*. Springer, 2008, pp. 915–923.

[67] S. McCloskey, M. Langer, and K. Siddiqi, "Removing Partial Occlusion from Blurred Thin Occluders," in *Pattern Recognition, International Conference on*. Los Alamitos, CA, USA: IEEE Computer Society, 2010, pp. 4400–4403.

[68] R. Willson, M. Maimone, A. Johnson, and L. Scherr, "An optical model for image artifacts produced by dust particles on lenses," in *8th International Symposium on Artificial Intelligence, Robotics, and Automation in Space (i-SAIRAS)*, vol. 1, no. 1, 2005, pp. 5–8.

[69] C. Zhou and S. Lin, "Removal of Image Artifacts Due to Sensor Dust," in *2007 IEEE Conference on Computer Vision and Pattern Recognition*. IEEE, 2007, pp. 1–8.

[70] J. Gu, R. Ramamoorthi, P. Belhumeur, and S. Nayar, "Removing image artifacts due to dirty camera lenses and thin occluders," *ACM Transactions on Graphics*, vol. 28, no. 5, p. 1, 2009.

[71] C. Schmid, R. Mohr, and C. Bauckhage, "Evaluation of interest point detectors," *International Journal of computer vision*, vol. 37, no. 2, pp. 151–172, 2000.

[72] B. Zitova, "Image registration methods: a survey," *Image and Vision Computing*, vol. 21, no. 11, pp. 977–1000, 2003.

[73] C. Tomasi and R. Manduchi, "Bilateral filtering for gray and color images," 1998, pp. 839–846.

[74] R. C. Gonzalez and R. E. Woods, *Digital Image Processing*, 2nd ed. Boston, MA, USA: Addison-Wesley Longman Publishing Co., Inc., 2001.

[75] G. J. Mclachlan, *Discriminant Analysis and Statistical Pattern Recognition (Wiley Series in Probability and Statistics)*. Wiley-Interscience, 2004.

[76] S. Duthaler and B. Nelson, "Autofocusing Algorithm Selection in Computer Microscopy," in *2005 IEEE/RSJ International Conference on Intelligent Robots and Systems*. IEEE, 2005, pp. 70–76.

[77] S. Yazdanfar, K. B. Kenny, K. Tasimi, A. D. Corwin, E. L. Dixon, and R. J. Filkins, "Simple and robust image-based autofocusing for digital microscopy," *Optics express*, vol. 16, no. 12, pp. 8670–7, 2008.

[78] G. Leban, I. Bratko, U. Petrovic, T. Curk, and B. Zupan, "VizRank: finding informative data projections in functional genomics by machine learning," *Bioinformatics (Oxford, England)*, vol. 21, no. 3, pp. 413–4, 2005.

[79] J. P. Lewis, "Fast normalized cross-correlation," in *Vision Interface*. Canadian Image Processing and Pattern Recognition Society, 1995, pp. 120–123.

[80] D. Tsai, "Segmenting focused objects in complex visual images," *Pattern Recognition Letters*, vol. 19, no. 10, pp. 929–940, 1998.

[81] J. Wang, R. Gray, and G. Wiederhold, "Unsupervised multiresolution segmentation for images with low depth of field," *IEEE Transactions on Pattern Analysis and Machine Intelligence*, vol. 23, no. 1, pp. 85–90, 2001.

[82] C. Kim, J. Park, J. Lee, and J. N. Hwang, "Fast Extraction of Objects of Interest from Images with Low Depth of Field," *ETRI Journal*, vol. 29, no. 3, pp. 353–362, 2007.

[83] Z. Liu, W. Li, L. Shen, Z. Han, and Z. Zhang, "Automatic segmentation of focused objects from images with low depth of field," *Pattern Recognition Letters*, vol. 31, no. 7, pp. 572–581, 2010.

[84] E. Reinhard and E. A. Khan, "Depth-of-field-based alpha-matte extraction," *Proceedings of the 2nd symposium on Appied perception in graphics and visualization - APGV '05*, p. 95, 2005.

[85] R. Bilcu, S. Alenius, and M. Vehvilainen, "A novel method for multi-focus image fusion," in *Image Processing (ICIP), 2009 16th IEEE International Conference on*. IEEE, 2010, pp. 1525–1528.

[86] M. Boissenin, J. Wedekind, a. Selvan, B. Amavasai, F. Caparrelli, and J. Travis, "Computer vision methods for optical microscopes," *Image and Vision Computing*, vol. 25, no. 7, pp. 1107–1116, 2007.

[87] S. Nayar and Y. Nakagawa, "Shape from focus: An effective approach for rough surfaces," in *IEEE International Conference on Robotics and Automation*. IEEE, 1990, pp. 218–225.

[88] K. Kodama, "Generation of arbitrarily focused images by using multiple differently focused images," *Journal of Electronic Imaging*, vol. 7, no. 1, pp. 138–144, 1997.

[89] A. Castorina, A. Capra, S. Curti, E. Ardizzone, and V. Lo Verde, "Improved multi-resolution image fusion," in *2005 Digest of Technical Papers. International Conference on Consumer Electronics, 2005. ICCE.* IEEE, 2005, pp. 131–132.

[90] H. M. Merklinger, *The INs and OUTs of FOCUS*, 2002.

[91] I. Ersoy, F. Bunyak, M. Mackey, and K. Palaniappan, "Cell segmentation using Hessian-based detection and contour evolution with directional derivatives," in *15th IEEE International Conference on Image Processing (ICIP 2008)*. IEEE, 2008, pp. 1804–1807.

[92] M. Oberlaender, V. J. Dercksen, R. Egger, M. Gensel, B. Sakmann, and H. C. Hege, "Automated three-dimensional detection and counting of neuron somata," *Journal of Neuroscience Methods*, vol. 180, no. 1, pp. 147–160, 2009.

[93] P. Usenik, T. Vrtovec, F. Pernus, and B. Likar, "Automated Tracking of Vesicles in Phase Contrast Microscopy Images," in *20th International Conference on Pattern Recognition*. IEEE, 2010, pp. 2520–2523.

[94] A. Garrido and N. Pérez de la Blanca, "Applying deformable templates for cell image segmentation," *Pattern Recognition*, vol. 33, no. 5, pp. 821–832, 2000.

[95] T. Peng, A. Balijepalli, S. K. Gupta, and T. LeBrun, "Algorithms for On-Line Monitoring of Micro Spheres in an Optical Tweezers-Based Assembly Cell," *Journal of Computing and Information Science in Engineering*, vol. 7, no. 4, p. 330, 2007.

[96] S. Z. Li, *Markov random field modeling in image analysis*. Secaucus, NJ, USA: Springer-Verlag New York, Inc., 2001.

[97] K. Held, E. R. Kops, B. J. Krause, W. M. Wells, R. Kikinis, and H.-W. M. Gärtner, "Markov random field segmentation of brain mr images," *IEEE Trans. Med. Imaging*, vol. 16, no. 6, pp. 878–886, 1997.

[98] Z. Kato and T. Pong, "A Markov random field image segmentation model for color textured images," *Image and Vision Computing*, vol. 24, no. 10, pp. 1103–1114, 2006.

[99] R. S. Alomari, S. Kompalli, and V. Chaudhary, "Segmentation of the Liver from Abdominal CT Using Markov Random Field Model and GVF Snakes," in *2008 International Conference on Complex, Intelligent and Software Intensive Systems*. IEEE, 2008, pp. 293–298.

[100] S. Geman and D. Geman, *Stochastic relaxation, Gibbs distributions, and the Bayesian restoration of images*. San Francisco, CA, USA: Morgan Kaufmann Publishers Inc., 1990, pp. 452–472.

[101] J. Besag, "On the statistical analysis of dirty pictures," *Journal of the Royal Statistical Society*, vol. B-48, pp. 259–302, 1986.

[102] C. M. Sayes, A. M. Gobin, K. D. Ausman, J. Mendez, J. L. West, and V. L. Colvin, "Nano-C60 cytotoxicity is due to lipid peroxidation," *Biomaterials*, vol. 26, no. 36, pp. 7587–7595, 2005.

[103] Y. J. Tang, J. M. Ashcroft, D. Chen, G. Min, C.-H. Kim, B. Murkhejee, C. Larabell, J. D. Keasling, and F. F. Chen, "Charge-Associated Effects of Fullerene Derivatives on Microbial Structural Integrity and Central Metabolism," *Nano Letters*, vol. 7, no. 3, pp. 754–760, 2007.

[104] R. Lipowsky, "The morphology of lipid membranes," *Current Opinion in Structural Biology*, vol. 5, no. 4, pp. 531–540, 1995.

[105] G. T. Linke, R. Lipowsky, and T. Gruhn, "Free fluid vesicles are not exactly spherical," *Physical Review E*, vol. 71, no. 5, p. 051602, 2005.

[106] M. Kraus, U. Seifert, and R. Lipowsky, "Gravity-induced shape transformations of vesicles," *Europhysics Letters*, vol. 32, no. 5, p. 431, 1995.

[107] V. V. Ginzburg and S. Balijepalli, "Modeling the thermodynamics of the interaction of nanoparticles with cell membranes," *Nano Letters*, vol. 7, no. 12, pp. 3716–3722, 2007.

[108] B. Babnik, D. Miklavcic, M. Kanduser, H. Hägerstrand, V. Kralj-Iglic, and A. Iglic, "Shape transformation and burst of giant popc unilamellar liposomes modulated by non-ionic detergent c12e8," *Chemistry and Physics of Lipids*, vol. 125, no. 2, pp. 123–138, 2003.

[109] F. Meyer, "Topographic distance and watershed lines," *Signal Processing*, vol. 38, no. 1, pp. 113–125, 1994.

A Povzetek disertacije

A.1 Uvod

V disertaciji predstavljamo metodologijo za *in vitro* študij bio-nano interakcij zasnovano na poskusu z nanodelci in orjaškimi lipidnimi vezikli. Pričakovani cilj metodologije je, da s pomočjo pristopov računalniške obdelave slik ugotovimo, ali se dve populaciji veziklov razlikujeta po številu veziklov in velikostni porazdelitvi njihovih premerov. Takšna primerjava je posebej zanimiva, če sta bili populaciji izpostavljeni različnim dodatkom, katerih učinek nas zanima. Poleg poskusa, kjer zajamemo slikovne ali video mikrografske posnetke populacije veziklov, metodologija obsega še računalniške pristope za lepljenje posnetkov v mozaike, segmentacijo oblik veziklov iz njih in statistično obdelavo pridobljenih podatkov. Kljub temu da je v prvih poglavjih predstavljeno bio-nano ozadje ter motivacija, se jedro disertacije nanaša na protokol poskusa, avtomatizacijo računalniškega procesiranja, ki vodi od obdelave surovih videoposnetkov do statistične analize posnetih veziklov.

Pričujočo metodologijo lahko v grobem razdelimo na pet korakov (Slika 1.1). Najprej naredimo poskus z lipidnimi vezikli. Protokol za izvrševanje poskusa je prilagojen snemanju populacij veziklov, v primerjavi s snemanjem posameznih veziklov, kot je bilo v navadi pri dozdajšnjih raziskavah. Kot naslednji korak predstavljamo pretvorbo video mikroskopskega posnetka populacije veziklov v mozaik, veliko zlepljeno sliko, na kateri je vidna vsa posneta površina istočasno. Predstavitev populacije veziklov v mozaiku omogoča tako ročno kot tudi avtomatsko segmentacijo veziklov. Za ročno segmentacijo smo razvili vtičnik "Shape Segmenter" za programsko orodje "ImageJ", s katerim lahko operater obrisuje vezikle, kar pa se je izkazalo za časovno zelo zahtevno opravilo. Da bi pohitrili segmentacijo, smo prilagodili model Markovovega naključnega polja za segmentacijo slik. Rezultat avtomatske segmentacije (z minimalnimi ročnimi popravki) so mozaiki, na katerih so različne oblike veziklov pobarvane z označbami različnih barv. Te označbe v naslednjem koraku preberemo in izračunamo velikosti oblik, ki jih predstavljajo, ter ovrednotimo pogostost pojavljanja in velikostno porazdelitve premerov veziklov v opazovani populaciji. Na podlagi primerjave izračunanih podatkov o veziklih v več populacijah lahko ugotovimo, ali pogoji, ki jim je populacija izpostavljena, vplivajo na oblikovne spremembe oziroma povzročajo pokanje veziklov. Metodologijo v disertaciji preizkusimo v treh eksperimentih. Najprej s sintetiziranimi slikami veziklov, kjer primerjamo osnovno različico modela Markovovega naključnega polja z našo izpopolnjeno različico. Sledita dva poskusa z vezikli in nanodelci, posneta po predlaganem protokolu. V enem lipidne vezikle izpostavimo negativno nabitim in nevtralnim kobalt-feritnim nanodelcem $CoFe_2O_4$, v drugem pa fulerenom – nano C_{60}.

Predstavljena in verificirana metodologija je začetek nove veje raziskav interakcij med lipidnimi vezikli in nanodelci, kjer se pozornost premakne s posameznih veziklov na njihove populacije. Morebitna širša uporabnost metodologije se bo izkazala v novih eksperimentih, pri katerih pričakujemo nova odkritja o interakcijah med nanodelci in lipidnimi vezikli.

A.2 Eksperiment z nanodelci in lipidnimi vezikli

Nanotehnologija je panoga, ki razvija, karakterizira in proizvaja materiale v velikosti 1–100 nanometrov. Materiali, proizvedeni v tem velikostnem razredu, spremenijo lastnosti v primerjavi z večjimi materiali iste kemijske sestave, kar jih naredi zanimive za

širok spekter uporabe v zdravstvu, industriji ličil, elektrotehniki, proizvodnji energije itd. Veliko navdušenje pri iskanju novih aplikacij v znanosti in industriji pa spremljata tudi previdnost in strah. Lastnosti, ki so pri nanodelcih zanimive, hkrati predstavljajo tudi možno nevarnost za okolje in človeka. Ker vpliv nanodelcev na okolje še ni široko raziskan, se pojavlja vprašanje, kako zagotoviti sistematično preverjanje morebitne škodljivosti na novo proizvedenih nanodelcev in dolgoročno zagotoviti njihovo varno uporabo. Zaradi hitrega razvoja nanotehnologije je ključnega pomena, da razvijemo, izdelamo in v praksi uveljavimo tudi metodologijo za vrednotenje varnosti nanodelcev [10]. Nedavne raziskave kažejo, da pri interakcijah z živimi bitji nanodelci najprej vstopijo v stik s celičnimi membranami in povzročijo verigo celičnih sprememb [13]. Preprost model, ki se pogosto uporablja za natančno proučevanje interakcij med celičnimi membranami in različnimi topnimi kemikalijami, so lipidni vezikli.

Lipidni vezikli, iz istega materiala kot biološke celične membrane narejeni mehurčki, so v raziskavah in aplikacijah pogosto uporabljeni kot poenostavljeni modeli celic [19, 21]. Na širokem področju raziskav obnašanja celičnih membran v različnih pogojih postajajo zelo priljubljen nadomestek pravih celic, saj jih lahko zaradi velikosti neposredno opazujemo pod svetlobnim mikroskopom. V večini poskusov, kjer preverjamo interakcije kemikalij z vezikli, operater izbere en sam vezikel, ga osami v vidnem polju mikroskopa in zajema slike skozi daljše časovno obdobje [24, 29]. Zaradi specifičnosti nanodelcev in njihovega nepredvidljivega obnašanja v stiku z vezikli [16] je za njihovo proučevanje zelo zanimiv naslednji pristop, na katerem temelji tudi naše delo. Namesto spremljanja enega samega vezikla v eksperimentu, zajamemo sliko populacije veziklov v določenih časovnih obdobjih izpostavljenosti in iz posnetka ob vsakem časovnem obdobju naredimo statistično analizo porazdelitev velikosti, oblik, pojavljanja netipičnih veziklov in njihovih morfoloških značilnosti [1–4]. Ker je pristop k raziskovanju interakcij populacij veziklov z nanodelci nov, v tej disertaciji predstavljamo po našem vedenju prvo specifično rešitev. Predstavljena metodologija vključuje protokol za izvedbo eksperimenta in zajem mikrografij ter računalniške pristope za analizo populacij veziklov.

Izvedli smo dva eksperimenta s populacijami lipidnih veziklov in različnimi nanodelci. V enem smo raziskovali interakcije veziklov s C_{60} fulereni, v drugem pa s kobalt-feritnimi $CoFe_2O_4$ nanodelci. Razlike med poskusoma so navedene v tabeli Tab. 3.1. V tem poglavju predstavljamo protokol, ki je enak za oba eksperimenta.

Orjaški unilamelarni fosfolipidni vezikli so pripravljeni iz 1-palmitoil-2-oleoil-sn-glicero-

3-fosfatidilholin (POPC) in holesterola, zmešanega v razmerju 4:1 na sobni temperaturi s prilagojeno metodo elektroformacije [42], kot je opisana v [43]. 24 ur po začetku priprave veziklov začnemo izvajanje eksperimenta, ki je sestavljen iz naslednjih korakov. Za vsako populacijo (v kontrolno ne bomo dodajali aditivov, v nano bomo dodajali nanodelce in v referenčno izbran detergent) pripravimo po eno objektno stekelce, na katerega namestimo 45 μl veliko kapljico suspenzije z vezikli. Na vzorec poveznemo manjše objektno stekelce, ob straneh pa prostor z vzorcem zapremo s silikonsko pasto, da preprečimo izhlapevanje. V shemi Slika 6.11 je prikazan potek poskusa s C_{60}, kjer vsem populacijam dodamo različne aditive. Na vsakem stekelcu določimo mesto (P1), kjer poteka snemanje. V primeru, da je mest več (P1 in P2), sta mesti določeni nekaj milimetrov narazen, kar omogoči spremljanje vpliva koncentracijskega gradienta aditiva na vezikle. Pod 400-kratno povečavo fazno kontrastnega mikroskopa nato posnamemo eno-dimenzionalno sled, v kateri je zajet vzorec populacije veziklov. Snemanje lahko ponovimo večkrat (za oba poskusa so obdobja snemanja v tabeli Tab. 3.1), tako da zajamemo spremembe v populacijah skozi čas. Posnete mikrografije ali videi so osnova, ki jo pozneje računalniško obdelamo, da izločimo podatke o zajetih populacijah veziklov.

A.3 Pretvorba video mikroskopskih posnetkov v mozaike

Proučevanje vzorca, ki je večji od vidnega polja na izbrani povečavi pod mikroskopom, je izvedljivo z lepljenjem posameznih mikrografij v mozaik. Pristop so fotografi uporabljali že v 19. stoletju, v 20. pa so ga prevzeli tudi znanstveniki, tako da je danes razširjen na mnogih področjih. V mikroskopiji lahko mozaik večjega opazovanega vzorca naredimo tako, da vzorec premikamo pod mikroskopom in zajemamo delno prekrivajoče se mikrografije. Te nato zlepimo v mozaik, tako da uporabimo plačljiva programska orodja [50], ali pa razvijemo algoritem, namenjen za lepljenje mikrografij, ki so tipične za naš vzorec [49, 54–56] (dober pregledni članek je [53]). Poleg slik lahko za lepljenje mozaikov uporabimo tudi video mikroskopske posnetke [65, 66], kjer je pristop podoben lepljenju posameznih slik. Naš protokol snemanja populacij veziklov vključuje zajem videoposnetkov. Dinamična narava veziklov namreč zahteva zajem karseda velikega vzorca v čimkrajšem času, kar lažje dosežemo z videoposnetki kot s posameznimi mikrografijami. Pri lepljenju videoposnetka populacije lipidnih veziklov v mozaik se pojavijo naslednji problemi, ki jih rešujemo v disertaciji:

- odstranjevanje digitalne nečistoče z videoposnetkov, ki je nastala zaradi prašnih delcev v optičnem in snemalnem delu mikroskopa,
- odstranjevanje neostrih in popačenih slik videoposnetka iz izbora za lepljenje mozaika,
- razrez videoposnetka za hitrejše procesiranje zaradi visoke računske zahtevnosti,
- odkrivanje objektov v mozaiku, ki izstopajo iz ozadja,
- iskanje najostrejših slik vsakega vezikla v videoposnetku,
- lepljenje najostrejših slik veziklov v mozaik.

Postopek je sestavljen iz korakov predstavljenih na shemi (Slika 4.2). Vhodni podatek v postopek je eno-dimenzionalni videoposnetek sledi s populacijo lipidnih veziklov. Izhodni podatek je velika slika, mozaik, ki predstavlja celotno posneto področje. Vsak vezikel v mozaiku je predstavljen z najostrejšo sliko, ki ga v mozaiku predstavlja. Za odstranitev digitalne nečistoče z videoposnetkov najprej izdelamo sliko nečistoče – iz naključnega izbora 300 slik izračunamo za vsako točko slike nečistoče mediano vseh istoležnih točk v izboru slik. Točke skupaj sestavljajo sliko nečistoče, ki jo odštejemo od vsake slike videoposnetka (Enačba 4.2). Rezultat so slike videoposnetka z vezikli in brez digitalne nečistoče. Da bi dobili položaj posamezne slike videoposnetka v mozaiku, potrebujemo registracijo. Med vsakima zaporednima slikama izračunamo normirano križno korelacijo, iz katere lahko razberemo, kolikšen je premik med njima. Ta premik v naši aplikaciji je globalni premik. Iz vsote zaporednih premikov lahko za vsako sliko določimo položaj znotraj mozaika.

Povprečni videoposnetek posamezne sledi je dolg 5 minut, kar ob 25 slikah na sekundo pomeni 7500 slik. Dimenzije mozaika tako presegajo 40.000 x 2.000 točk, zato je procesiranje tako velikih slik časovno zelo zahtevno. Pospešitev izvedemo tako, da vse korake lepljenja mozaikov (in pozneje tudi detekcijo veziklov) izvajamo na posameznih delih mozaika. Mozaik razrežemo na dele vodoravno, za vrstice razreza pa izberemo tiste z najmanjšo varianco v svetlobni jakosti. Vrstice, kjer je svetlobna jakost najbolj homogena, so namreč vrstice, kjer vezikli ne nastopajo. Z razrezi v teh vrsticah zagotovimo, da ni noben vezikel ni v delu mozaika le polovično, kar bi izničilo verodostojnost končnega mozaika. Da bi dobili mozaik, je potrebno vse slike videoposnetka združiti v celoto. Vsaka točka mozaika se namreč pojavlja tudi v več sto slikah, v katerih ima lahko tudi

različne vrednosti. Pri našem mozaiku za vsako točko njeno svetlobno jakost izračunamo kot mediano vseh istoležnih točk v slikah videoposnetka. Tako dobimo prvi, "medianski" mozaik, ki pa ni popoln. Slike veziklov so neostre, kar onemogoča natančno segmentacijo njihovih oblik. Naslednji koraki so namenjeni izostritvi veziklov v mozaiku.

Za vsak del mozaika naredimo detekcijo objektov (večina objektov so vezikli, nekaj pa je tudi delcev zlepljenih fosfolipidov ali drugih tujkov v vzorcu). Glavni koraki te detekcije temeljijo na izračunu gradientov svetlobne jakosti za vsako točko, povezovanju točk z najočitnejšimi gradienti v robove (detekcija robov Sobel), in na povezovanju robov, ki so si dovolj blizu, v objekte z uporabo morfoloških operatorjev. Na ta način zaznamo vse objekte v mozaiku, ki s svojo svetlobno heterogenostjo odstopajo od homogenega ozadja. Nad vsakim objektom v naslednjem koraku izvedemo lokalno detekcijo premikov. Tokrat vsako sliko poravnamo z mozaikom in z normalizirano križno korelacijo izračunamo premik vsakega posameznega objekta med mozaikom in posamezno sliko. Tako lahko z uporabo globalnega premika slike (premikanje objektnega slike pod objektivom) in lokalnega premika objekta (vezikli so v fluidu), slednjega v vsaki sliki poravnamo. Rezultat opisanega postopka je poravnanost istoležnih objektov v vseh slikah videoposnetka z njihovim položajem v medianskem mozaiku. Med poravnanimi slikami veziklov je potrebno izbrati najostrejšo. Primerjali smo več mer izostrenosti mikroskopskih slik [76] in izbrali mero gradient Brenner za določanje ostrine objekta v sliki. Izbrano sliko objekta je potrebno zliti v medianski mozaik. Če jo preprosto prilepimo nanj, nastanejo svetlobna neujemanja na robovih, zato potrebujemo naprednejši pristop. Za zlivanje najostrejših slik objektov na mozaik uporabimo zlivanje v gradientni domeni. Iz svetlobnih jakosti na robovih objekta v ciljnem medianskem mozaiku in gradienta objekta iz najostrejše slike, izračunamo nove vrednosti točk objekta v mozaiku. Takšna gradientna interpolacija omogoča najostrejše slike objektov v medianskem mozaiku brez vidnih robov, kjer nastopa lepljenje.

A.4 Segmentacija populacij veziklov iz mozaikov

Problema segmentacije lipidnih veziklov iz mikroskopskih slik so se v literaturi lotili mnogi, največkrat s pomočjo svetlečega obroča, ki nastane okoli veziklov na slikah posnetih s faznokontrastnim mikroskopom [24, 27, 29, 32, 93]. Svetlobna jakost preseka slike vezikla ima na vsaki strani obliko sigmoide, saj je notranjost veziklov temnejša od okolice

(kemijska sestava okolice se razlikuje od tiste v notranjosti vezikla). Omenjeno lastnost avtorji uporabijo tako, da njihov algoritem obriše vezikel iz začetne ročne inicializacije njegovega roba. Peterlin idr. [24] so za segmentacijo vezikla iz slik videoposnetka uporabili prilagodljiv prag svetlobne jakosti v sliki skupaj z detektorjem robov Sobel. Takšni pristopi k segmentaciji veziklov so se izkazali za uspešne, vendar je na tem mestu potrebno dodati, da so se avtorji ukvarjali s segmentacijo enega samega vezikla in pogostokrat z ročno inicializacijo njegovega obroča. Kadar pa segmentacija ni omejena le na izolirane vezikle, pristopi, ki so vezani na njihovo sferično obliko, odpovedo. Za segmentacijo populacije smo se osredotočili na lastnost, ki je skupna vsem veziklom, ne glede na njihovo obliko. Porazdelitvi svetlobne jakosti dveh področij vezikla (obroča in notranjosti) sta si v vseh primerih zelo podobni. Obroč vezikla je svetlejši od ozadja, njegova notranjost pa temnejša. Za segmentacijo populacije veziklov smo izbrali model Markovovega naključnega polja (MRF) [98], ki poleg porazdelitev svetlobnih jakosti posameznih segmentov slike upošteva še sosednost točk v slikah.

Sliko (posamezna mikrografija ali mozaik) želimo razdeliti na tri segmente, katerih porazdelitvene funkcije svetlobnih jakosti se razlikujejo: vezikel, obroč in ozadje. Ideja modela Markovovega naključnega polja je naslednja. Svetlobna jakost vsake točke slike z določeno verjetnostjo pripada enemu izmed segmentov. Naloga je poiskati največjo vezano verjetnost vseh točk z upoštevanjem znane verjetnostnih porazdelitev svetlobnih jakosti posameznih segmentov, svetlobnih jakosti posameznih točk in povezav med sosednimi točkami. Ker se je osnovni MRF model izkazal za nezadostno natančnega, smo potencialni funkciji PF [98] dodali še en člen, ki upošteva specifično strukturo mikrografij veziklov (Enačba 5.14). Točka ozadja, ki je ima za sosede več točk notranjosti ali obroča, z večjo verjetnostjo postane notranjost vezikla. Segmentacija vseh točk mozaika je zaradi računske zahtevnosti algoritma neizvedljiva. Za pospešitev in izboljšanje natančnosti tudi v korak natančne segmentacije veziklov vpeljemo v detekcijo objektov. MRF segmentacijo tako izvedemo le na okolici posameznih objektov in ne na celotnem mozaiku istočasno. Celoten postopek je načrtovan tako, da segmentiramo vse objekte – tako vezikle, kot tudi ostale objekte. Tako segmentacija ne obsega le veziklov, ampak tudi nekatere tujke, ki so prisotni v vzorcu. Po računalniški segmentaciji operater pregleda in popravi segmentacijo mozaikov, po večini tako da izbriše vse označbe, ki niso vezikli. S takšno ročno korekcijo, ki zahteva približno osemkrat manj časa kot celotna ročna segmentacija, zagotovimo ustrezno natančnost segmentacije in verodostojnost pridobljenih

podatkov.

A.5 Rezultati in diskusija

Iz mozaikov s segmentiranimi notranjostmi veziklov izločimo vse segmentirane točke in izračunamo njihovo površino. Iz primerjave velikostnih porazdelitev veziklov in njihovega števila v posameznih mozaikih lahko ugotovimo, kako je dodani aditiv vplival na vezikle v populaciji skozi čas. V disertaciji smo analizirali eksperimenta z dvema različnima vrstama nanodelcev: $CoFe_2O_4$ in C_{60}.

Iz videoposnetkov, zajetih po opisanem protokolu, smo z uporabo predstavljene avtomatizacije pridobili natančne podatke o veziklih in njihovih velikostih. V poskusu s kobalt feritnimi nanodelci se je povprečen premer veziklov v neizpostavljeni kontrolni populaciji po 90 minutah inkubacije zmanjšal s 6.5 μm na 6 μm. V populacijah, izpostavljenih nevtralnim in negativno nabitim kobalt feritnim nanodelcem, so se vezikli v povprečju povečali na 8.1 μm oziroma 8.5 μm. Prav tako smo ugotovili povečano pojavljanje nesferičnih veziklov (5–15 odstotkov vseh) v populacijah z dodanimi (tako negativno nabitimi kot tudi nevtralnimi) kobalt feritnimi nanodelci.

V eksperimentu z nanodelci C_{60} smo ročno označili 7670 veziklov v 810 slikah. Ugotovili smo, da je učinek C_{60} takojšen in da tako kot referenčna kemikalija $ZnCl_2$ pospeši pokanje veziklov. Učinek je bil takoj opazen blizu mesta dodajanja, kjer je popokalo 80 odstotkov veziklov. Na drugem mestu snemanja, nekaj milimetrov oddaljenem od lokacije dodajanja, je bil učinek C_{60} manjši od tistega pri $ZnCl_2$, spremembe so bile opazne šele po 100 minutah inkubacije. Iz porazdelitev velikosti premerov veziklov v vseh populacijah je razvidno, da sta tako C_{60} kot tudi $ZnCl_2$ najbolj vplivala na pokanje večjih veziklov, manjši vezikli pa so bili manj prizadeti. Pridobljeni rezultati kažejo, da imata testirani koncentraciji tako C_{60} kot tudi $ZnCl_2$ vpliv na lipidne vezikle. V večini primerov povzročita pokanje veziklov večjih dimenzij. Morfološke spremembe so se pokazale le v primeru dodajanja nanodelcev $CoFe_2O_4$, kjer smo ugotovili povečano pojavljanje nesferičnih veziklov, najbolj opazno verižic. Do podobnih rezultatov z nanodelci C_{60} so se dokopali tudi drugi raziskovalci, ki v svojih eksperimentih s spremljanjem propustnosti membrane za C_{60} z uporabo raznih barvil, poročajo o podobnih distrupcijah membran [102].

Z rezultati eksperimentov smo pokazali uporabnost metodologije za analiziranje pop-

ulacij lipidnih veziklov, predstavljene v tej disertaciji. V času, ki smo ga imeli na voljo za snemanje, smo lahko z videoposnetki zajeli 100 odstotkov posamezne sledi. Tak vzorec je dovolj velik, da smo dobili vpogled v dogajanje po interakciji lipidnih veziklov z nanodelci. Lepljenje videoposnetkov v mozaike in avtomatska segmentacija veziklov, skupaj z malim časovnim vložkom operaterja, zagotavljata visoko stopnjo zaupanja v rezultate. Celotno eksperimentalno delo, ki je pred avtomatizacijo vključevalo zelo obsežno ročno delo, smo pospešili tudi do osemkrat. V večini primerov pa lahko operater zdaj že v enem dnevu dobi rezultate. Zanje je bil prej potreben en teden ročnega dela.

A.6 Prispevki k znanosti

V disertaciji so predstavljeni naslednji prispevki k znanosti:

1. Predlagam novo metodologijo za preiskavo vplivov različnih nanodelcev na orjaške unilamelarne lipidne vezikle. Glavni prispevek je protokol zajema slik ali videoposnetkov, predvsem uporaba populacije namesto osamljenih veziklov, kar je sicer zdajšnja široka praksa.

2. V disertaciji pokažem, da lahko metodologijo uspešno uporabimo v eksperimentih, kjer nas zanimajo interakcije med nanodelci in lipidnimi vezikli.

3. V jedru metodologije so predstavljeni koraki, kako iz slik videoposnetkov populacije lipidnih veziklov zlepimo kakovosten mozaik posnetega področja. Najpomembnejši je hierarhičen pristop k registraciji slik, pri kateri najprej poravnamo celotne slike, potem pa v nastalem mozaiku registriramo tudi posamezne vezikle, ki se med slikami premikajo neodvisno od premikanja vzorca v videoposnetku.

4. Za segmentacijo veziklov iz mozaikov, predlagam dopolnjen model Markovega naključnega polja. Takšen pristop omogoča hkratno detekcijo in ustrezno segmentacijo populacije veziklov in analizo njihovih velikosti ter oblik.

Dele disertacije smo objavili v šestih mednarodnih znanstvenih publikacijah: dva konferenčna prispevka na biomedicinskih konferencah združenja IEEE v letih 2009 in 2010 [1, 2], članek v novi reviji o biomedicinskih nanoznanostih [3], reviji s področja biomedicinske optike [4], v reviji s področja raziskav lipidnih veziklov [5] in v slovenski medicinski reviji [6].

B Publications

1. J. Zupanc, J. Valant, A. Dobnikar, V. Kralj-Iglic, A. Iglic, and D. Drobne, "Interactions of nanoparticles with lipid vesicles: A population based computer aided image analysis approach," in *Proc. Annual Int. Conf. of the IEEE Engineering in Medicine and Biology Society EMBC*, 2009, pp. 1400–1403.

2. J. Zupanc, E. Bas, and D. Erdogmus, "Analysis of lipid vesicle populations from microscopy video sequences," in *Proc. Annual Int. Conf. of the IEEE Engineering in Medicine and Biology Society EMBC*, 2010, pp. 5050–5053.

3. J. Zupanc, J. Valant, D. Drobne, V. Kralj-Iglic, and A. Iglic, "A new approach to analyse effects of nanoparticles on lipid vesicles," *International Journal of Biomedical Nanoscience and Nanotechnology*, vol. 1, no. 1, pp. 34–51, 2010.

4. J. Zupanc, A. Dobnikar, D. Drobne, J. Valant, D. Erdogmus, and E. Bas, "Biological reactivity of nanoparticles: mosaics from optical microscopy videos of giant lipid vesicles," *Journal of Biomedical Optics*, vol. 16, no. 2, pp. 26003–10, 2011.

5. J. Zupanc, B. Ster, and D. Drobne, "Markov random field model for segmenting large populations of lipid vesicles from micrographs," *Journal of Liposome Research*, July 2011.

6. J. Zupanc, and D. Drobne, "Populacije orjaških lipidnih veziklov kot model za študij bio-nano interakcij," *Informatica Medica Slovenica*, vol. 16, no. 1, pp. 1-12, 2011.